

# **Exploration of Nanoscale Electromechanical Couplings**

by

**Nathaniel Charles Miller**

B.S. in Chemistry, University of Pittsburgh, 2011

P.S.M. in Industrial and Applied Chemistry, Indiana University of Pennsylvania, 2014

Submitted to the Graduate Faculty of  
the Kenneth P. Dietrich School of Arts and Sciences in partial fulfillment  
of the requirements for the degree of  
Doctor of Philosophy

University of Pittsburgh

2020

UNIVERSITY OF PITTSBURGH  
DIETRICH SCHOOL OF ARTS AND SCIENCES

This dissertation was presented

by

**Nathaniel Charles Miller**

It was defended on

April 2, 2020

and approved by

Seth Horne, Associate Professor, Chemistry Department

David H. Waldeck, Professor, Chemistry Department

Jeremy Levy, Associate Professor, Physics Department

Dissertation Advisor: Geoffrey Hutchison, Ph.D., Associate Professor, Chemistry Department

Copyright © by Nathaniel Charles Miller

2020

## Exploration of Nanoscale Electromechanical Couplings

Nathaniel Charles Miller, Ph.D.

University of Pittsburgh, 2020

This dissertation explores the electromechanical properties of organic piezoelectric materials and the measurement systems used to determine their unique properties. The project focus was to gain experimental insight into previously predicted piezoelectric molecules and develop new methods to accurately determine the electromechanical properties of their self-assembled monolayers.

Using atomic force microscopy, the nanoscale properties of organic self-assembled monolayers were studied to compare previous computational predictions with experiment. Piezo force microscopy (PFM), was used to quantify the magnitude of sample deformation by an applied electric field across monolayers of a set of macromolecules (peptides and peptoids) to determine their effective piezo coefficient ( $d_{\text{eff}}$ ). This resulted in small but differentiable responses been the peptides and peptoids. Through the study of these macromolecular monolayers, conventional PFM methods were found to be lacking sensitivity for these soft-flexible SAMs.

These insights lead to the development of a new method leveraging the physics of dual AC resonance tracking PFM (DART-PFM) to simultaneously increase the sensitivity of the measurement system and reduce the sources of error. A new DC-sweep DART-PFM methodology allowed for the accurate determination of piezo response in soft macromolecular monolayers, plus several small molecule and crystalline reference materials. The method adds an additional DC field sweep to the classical AC field sweep DART-PFM to determine the *in-situ* point where the electrostatic component of the tip response is minimized. This new method should provide

accurate determination of the vast library of “soft” piezoactive materials, as well as those with negative piezo coefficients, in which the material compresses under an applied field instead of expanding.

The newly developed DC-sweep DART-PFM method was implemented to study piezoactive “buckybowl” organic ferroelectric materials, in which the net polarization of the film can be flipped with a coercive field. The  $d_{\text{eff}}$  of a corannulene derivative was determined and hysteresis loops were observed via scanning Kelvin probe force microscopy, suggesting ferroelectric behavior near room temperature.

## Table of Contents

Preface.....	xxii
<b>1.0 Introduction.....</b>	<b>1</b>
<b>1.1 General Background .....</b>	<b>1</b>
<b>1.1.1 Basics of Electromechanical Coupling .....</b>	<b>1</b>
<b>1.1.1.1 Piezoelectricity .....</b>	<b>2</b>
<b>1.1.1.2 Classical Piezoelectric Materials .....</b>	<b>3</b>
<b>1.1.1.3 Piezoelectricity in Ceramic and Crystalline Materials.....</b>	<b>4</b>
<b>1.1.1.4 Piezoelectricity in Organic Materials.....</b>	<b>5</b>
<b>1.1.1.5 Ferroelectricity.....</b>	<b>5</b>
<b>1.1.1.6 Alternative Forms of Electromechanical Coupling .....</b>	<b>6</b>
<b>1.2 Self-Assembled Monolayers.....</b>	<b>9</b>
<b>1.3 Methodology Overview .....</b>	<b>11</b>
<b>1.3.1 Scanning Probe Microscopy.....</b>	<b>11</b>
<b>1.3.1.1 Topography .....</b>	<b>11</b>
<b>1.3.1.2 Scanning Kelvin Probe Microscopy .....</b>	<b>12</b>
<b>1.3.1.3 Piezo Force Microscopy .....</b>	<b>12</b>
<b>1.3.2 X-Ray Photoelectron Spectroscopy .....</b>	<b>13</b>
<b>1.3.2.1 XPS for Packing Density Determination in Self Assembled Monolayers</b> <b>.....</b>	<b>14</b>
<b>2.0 Influence of Molecular Structure on a Self-Assembled Monolayer’s Piezoresponse</b> <b>.....</b>	<b>15</b>

<b>2.1 Contributions .....</b>	<b>15</b>
<b>2.2 Introduction to Tailored Organic Molecular based Piezoelectric Materials .....</b>	<b>16</b>
<b>2.3 Methods .....</b>	<b>17</b>
<b>2.3.1 General Information .....</b>	<b>17</b>
<b>2.3.2 Peptide Synthesis.....</b>	<b>17</b>
<b>2.3.3 Peptoid Synthesis.....</b>	<b>18</b>
<b>2.3.4 Circular Dichroism .....</b>	<b>19</b>
<b>2.3.5 Self-Assembled Monolayer Formation.....</b>	<b>20</b>
<b>2.3.6 X-Ray Photoelectron Spectroscopy (XPS) .....</b>	<b>20</b>
<b>2.3.7 Atomic Force Microscopy (AFM) and Piezo Force Microscopy (PFM) .....</b>	<b>21</b>
<b>2.3.8 Calculation of Dipole Moment for Model Helicies.....</b>	<b>22</b>
<b>2.4 Results and Discussion .....</b>	<b>22</b>
<b>2.5 Conclusions .....</b>	<b>30</b>
<b>3.0 Optimization of Nanoscale Electromechanical Coupling Evaluation Methods .....</b>	<b>32</b>
<b>3.1 Contributions .....</b>	<b>32</b>
<b>3.2 Introduction .....</b>	<b>32</b>
<b>3.3 Methods .....</b>	<b>35</b>
<b>3.3.1 Monolayer Formation.....</b>	<b>35</b>
<b>3.3.2 Equipment.....</b>	<b>36</b>
<b>3.3.3 Dual AC Resonance Tracking Piezo Force Microscopy (DART-PFM).....</b>	<b>37</b>
<b>3.3.4 Scanning Kelvin Probe Force Microscopy (sKPFM) .....</b>	<b>37</b>
<b>3.3.5 Amplitude Modulated Force Microscopy (AMFM).....</b>	<b>38</b>
<b>3.4 Results and Discussion .....</b>	<b>38</b>

3.5 Conclusions .....	55
<b>4.0 Exploration of Organic-Molecular Based Ferroelectric Materials .....</b>	<b>57</b>
4.1 Contributions .....	57
4.2 Introduction .....	57
4.3 Methods .....	59
4.3.1 Sample Preparation .....	59
4.3.2 Dual AC Resonance Tracking Piezo Force Microscopy (DART-PFM).....	59
4.3.3 Scanning Kelvin Probe Force Microscopy (sKPFM).....	60
4.4 Results and Discussion .....	61
4.5 Conclusions .....	71
<b>5.0 Lab Scale Manipulation of Single and Multilayer Organic Self Assembled Structures.....</b>	<b>72</b>
5.1 Introduction .....	72
5.2 Experimental Methods.....	74
5.2.1 Materials .....	74
5.2.2 Sample Preparation Protocols .....	74
5.2.3 Scanning Kelvin Probe Force Microscopy (sKPFM).....	75
5.2.4 X-Ray Photoelectron Spectroscopy (XPS) .....	75
5.2.5 Transmission Electron Microscopy (TEM) .....	76
5.2.6 Photolithography.....	76
5.3 Results and Discussion .....	77
5.4 Multilayer Formation.....	86
5.4.1 Multilayer Development Stage 1.....	86

5.4.2 Multilayer Development Stage 2.....	87
5.4.3 Multilayer Development Stage 3.....	88
5.4.4 Multilayer Development Confirmation.....	89
5.5 Conclusions .....	91
6.0 Conclusion and Future Directions.....	92
6.1 Conclusion .....	92
6.2 Future Directions.....	96
Appendix A Supplementary Information for the Influence of Molecular Structure on a Self-Assembled Monolayer’s Piezoresponse.....	101
Appendix B Supplementary Information for the Optimization of Nanoscale Electromechanical Coupling Evaluation Methods .....	112
Appendix C Supplementary Information for the Lab Scale Manipulation of Single and Multilayer Organic Self Assembled Structures .....	121
Bibliography .....	131
B.1 Chapter 1 (Introduction).....	131
B.2 Chapter 2 (Influence of Molecular Structure on a Self-Assembled Monolayer’s Piezoresponse).....	132
B.3 Chapter 3 (Optimization of Nanoscale Electromechanical Coupling Evaluation Methods).....	135
B.4 Chapter 4 (Exploration of Organic-Molecular Based Ferroelectric Materials) ..	137
B.5 Chapter 5 (Lab Scale Manipulation of Single and Multilayer Organic Self Assembled Structures) .....	140
B.6 Chapter 6 (Conclusions and Future Directions) .....	143

## List of Tables

Table 1 Solution folding and monolayer properties for peptides 1-3 and peptoids 4-6. ....	29
Table 2 Summary of contact-dependent ( $k_c$ ) response across four organic self-assembled monolayers, indicating best-fit parameters from the fits in Figure 15.....	43
Table 3 Coefficient values and calculated $d_{\text{eff}}$ from tip response as a function of applied DC voltage at constant $V_{\text{AC}}$ of 4.0 V. ....	46
Table 4 Coefficient values and calculated $d_{\text{eff}}$ from tip response as a function of applied DC voltage at constant $V_{\text{AC}}$ of 3.0 V using 0.09 N/m $k_l$ levers. ....	50
Table 5 Coefficient values and calculated $d_{\text{eff}}$ from tip response as a function of applied DC voltage on peptoid B at constant $k_l$ of 0.09 N/m. ....	53
Table 6 TEM grid feature sizes with expected specification sizes, and TEM-measured average feature sizes including standard errors over at least ten samples.....	79
Appendix Table 1 MALDI-TOF MS data for peptides 1-3 and peptoids 4-6. ....	101
Appendix Table 2 Summary of tip-dependent ( $k_i$ ) response across four organic self-assembled monolayers, indicating best-fit parameters of tip response to $a + bx^c$ . ....	113
Appendix Table 3 Summary of tip-dependent ( $k_c$ ) response across four organic self-assembled monolayers, indicating best-fit parameters of tip response to $a + bx^{-1}$ . ....	114
Appendix Table 4 AMFM results for the measurement of $k_c$ with corresponding $k_l$ based on implemented lever.....	116
Appendix Table 5 Coefficient values and calculated $d_{33}$ from tip response as a function of $V_{\text{AC}}$ on peptoid B using 0.09 N/m $k_l$ levers at varying $V_{\text{DC}}$ . ....	116

Appendix Table 6 Coefficient values and calculated $d_{33}$ from tip response as a function of $V_{DC}$ on ZNO using 0.09 N/m $k_1$ levers at varying $V_{AC}$ .....	119
Appendix Table 7 Coefficient values and calculated $d_{33}$ from tip response as a function of $V_{AC}$ on ZNO using 0.09 N/m $k_1$ levers at varying $V_{DC}$ .....	119
Appendix Table 8 SKPFM results for the measurement of $V_{CPD}$ for various materials using 2.8 N/m levers.....	120

## List of Figures

Figure 1: Schematic of the piezoelectric effect from left to right: the direct piezoelectric effect, steady state, and converse piezoelectric effect; in which the arrows represent individual dipoles. <sup>7</sup> .....	3
Figure 2 Illustration of lead zirconium titanate (PZT) P4mm crystal lattice under zero field on the left and example deformation under an applied field on the right. In which the grey spheres represent lead atoms, red represents the oxygen atoms, and light blue represent either zirconium or titanium. <sup>2</sup> .....	4
Figure 3: Example responses from (a) dielectric materials, (b) paraelectric materials, and (c) ferroelectric materials. <sup>2</sup> .....	5
Figure 4: Schematic of ferroelectricity where the net polarization is manipulated by the application of an external electric field, in which the grey arrows represent individual dipoles. <sup>2,7</sup> .....	6
Figure 5: Schematic of electrostriction in which an applied electric field induces a temporary alignment of the polar units in a material creating a macrodipole moment in the material by which the material deforms in reaction to, in which the arrows represent individual dipoles. <sup>7</sup> .....	7
Figure 6: Schematic of flexoelectricity, in which the arrows represent individual dipoles. <sup>7</sup> .....	7
Figure 7: Schematic of the electrostatic effect. <sup>7</sup> .....	8
Figure 8: Schematic of the phases for the formation of self-assembled monolayers (SAMs). <sup>16</sup> ....	9
Figure 9 (A) Schematic depicting nanoscale piezo response of a self-assembled monolayer on gold upon applying an electric field. (B) Backbone chemical structures alongside models of the $\alpha$ -helix and PPI-helix folds formed by peptide and peptoid oligomers, respectively. ....	23
Figure 10 Peptides 1-3, peptoids 4-6, and control small molecule dodecanethiol (DDT).....	24

Figure 11 CD spectra of peptides 1-3 (50  $\mu\text{M}$  in 10 mM phosphate pH 7.2) and peptoids 4-6 (50  $\mu\text{M}$  in acetonitrile). Estimated helical folded population for each compound is indicated in parentheses..... 26

Figure 12 Summary of DART-PFM methodology used to determine piezoelectric response (see Supporting Information for details) and the resulting  $d_{33}$  values obtained from replicate independent experiments with peptides 1-3, peptoids 4-6, dodecanethiol (DDT), and quartz. Error bars are the SEM from 4-8 independent experiments (see Table 1)..... 28

Figure 13 (a) Traditional determination of piezoresponse using piezo-force microscopy by varied  $V_{AC}$  – the slope of the trend line should reflect the  $d_{eff}$  piezoresponse (pm/V). (b) Suggested  $V_{DC}$  sweep technique to determine the piezo response in soft-organic piezo in soft-organic piezo materials – the crossing point reflects the  $d_{eff}$  piezoresponse, and the slope reflects the electrostatic contribution of the material..... 39

Figure 14 Scheme of compounds under study.<sup>16</sup> ..... 41

Figure 15 Relationship between tip response ( $k_l$  and  $k_c$  as calculated using Equation 3.2) for various SAMs using AFM levers with spring constant from 0.02-2.8 N/m, for (a) DDT, (b) MUA, (c) peptide A and (d) peptoid B respectively. The best-fit line is to  $y = a + bx^c$ ..... 42

Figure 16 Influence of cantilever contact stiffness on measured film response as a function of DC field. Inset plots highlight the noise floor of the tip response ( $\sim 1$  pm) when the  $k_l$  is far greater than the modulus of the material. (a) Response of the DDT to varied DC field with three levers Asyelec.01 R2 (R2, 2.8 N/m), TR400PBS (TRS, 0.09 N/m), and TR400PBL (TRL, 0.02 N/m). (b) Response of peptide A to varied DC field with three levers Asyelec.01 R2 (R2), TR400PBS (TRS), and TR400PBL (TRL). ..... 46

Figure 17 PFM tip response from sweeping the DC field of several materials using TRS levers, and an applied AC field of 3.0 V. Response of (a) quartz crystal microbalance surface; inset provides rescaled y-axis, (b) DDT, (c) MUA, (d) Peptide A, and (e) Peptoid B. Note that all four organic monolayers show profoundly greater DC-field (electrostatic) response than the QCM surface as reflected in the slope of the DC-dependent response..... 49

Figure 18 (A) Effect of applied DC field on peptoid B film response at various AC fields using 0.09 N/m levers. (B) DC-dependent response. (C) PFM response as a function of  $V_{AC}$  with specified constant DC fields. (d) Measured surface potential as a function of applied  $V_{AC}$ . ..... 51

Figure 19 Schematic of 4,4',4'',4'''-(dibenzo[*ghi,mno*]fluoranthene-1,2,5,6-tetrayl)tetrabenzoic acid “H<sub>4</sub>DFT” (A). Schematic of the bowl to bowl inversion of a model corannulene molecule (B). ..... 62

Figure 20 Schematic of example electromechanically coupled responses from (A) dielectric materials, (B) paraelectric materials, and (C) ferroelectric materials.<sup>1, 15</sup> ..... 62

Figure 21 AFM amplitude topography of the resulting films from the drop-casting of decreasing H<sub>4</sub>DFT solution concentrations on a clean Au surface. The plot represents the correlation of decreasing root mean square (RMS) roughness of the Au/ H<sub>4</sub>DFT surface with decreasing solution concentration..... 63

Figure 22 (A) Effect of applied DC field on H<sub>4</sub>DFT film on Au response at various AC fields using 0.09 N/m levers. (B) DC-dependent response after removal of the AC field and averaging at each DC field..... 65

Figure 23 (A) Effect of applied DC field on H<sub>4</sub>DFT film on ITO response at various AC fields using 0.09 N/m levers. (B) DC-dependent response after removal of the AC field and averaging at each DC field. .... 65

Figure 24 (A) Schematic of 1-pyrenecarboxylic acid (B) Effect of applied DC field on 1-pyrenecarboxylic acid film on ITO with responses at various AC fields using 0.09 N/m levers. (C) DC-dependent response after removal of the AC field and averaging at each DC field. .... 66

Figure 25 Schematic of planned experimental procession for the confirmation of ferroelectric properties of H<sub>4</sub>DFT.<sup>2</sup> ..... 67

Figure 26 SKPFM surface potential of H<sub>4</sub>DFT on ITO after an applied DC field to substrate (A) 0.5 minute poling, (B) 1.0 minute poling, and (C) 2.0 minute poling, error bars represent the distribution of measured surface potentials over at least four samples. .... 68

Figure 27 SKPFM surface potential of a bare ITO surface, blue, and a monolayer of 1-pyrene carboxylic acid, red, after applied DC field, to substrate with a b 1.0 minute poling period, error bars represent the distribution of measured surface potentials over multiple samples. .... 69

Figure 28 SKPFM surface potential of H<sub>4</sub>DFT on ITO after an applied DC field to the substrate at (A) 17.0 °C, (B) 21.0 °C, and (C) 28.0 °C after a 1.0 min. dwell time; error bars represent the distribution of measured surface potentials over at least two samples. .... 70

Figure 29 (a) Rate of change in the incident intensity over a change in source-sample distance for a 175 W metal halide light source measured at  $\lambda = 380$  nm after filtration. (b) Calibration curve for the total energy exposure to a sample surface with a source-sample distance of 5.0 cm from a 175 W source for a given period. .... 78

Figure 30 SKPFM images illustrate the influence of total energy exposure and incident intensity on pattern formation. The inset times represent the exposure period at a given source-sample distance. .... 81

Figure 31 Calibration curves for the average relation between total energy exposure and pattern hole area for a given aperture size in which the error bars represent the standard error from at least

eight features. (a) Change in pattern hole area for an MUA SAM patterned and backfilled with DDT using a 2000 square mesh TEM grid as the photomask. (b) Change in pattern hole area for an MUA SAM patterned and backfilled with DDT using a 2000 circular mesh TEM grid as the photomask. The blue lines represent the pattern hole areas of the TEM grid masks used (Table 7). The red lines represent the line of best fit for which the equation of the line and the  $R^2$  are provided within in the individual plot. .... 83

Figure 32 (a) Example sKPFM potential scan of a patterned monolayer of MHDA/DDT using 2000 square mesh TEM grid as the photomask. (b) Resulting line scan from (a) indicating how the slope of the pattern interface is determined. (c) The migration of the pattern hole edge through the monitoring of the slope of an MHDA/DDT interface in a patterned film by sKPFM. (d) Example histogram of sKPFM potential scan of a patterned monolayer of MHDA/DDT using 2000 square mesh TEM grid as the photomask, all histograms A figure 7. (e) the change in the  $V_{CPD}$  of the pattern with the sample age as monitored by sKPFM in which blue represents the  $V_{CPD}$  of the MHDA and DDT respectively. (figure 4)..... 84

Figure 33 (A) Amplitude heat map after step 1 of patterned multilayer development and (B) KPFM heat map, both of an HDT monolayer patterned and backfilled with MHDA using the standard procedure..... 87

Figure 34 (A) Amplitude heat map after step 2 of patterned multilayer development and (B) sKPFM potential map, both of an HDT monolayer patterned and backfilled with MHDA using the standard procedure. The acid terminated sections of the patterned monolayer are then activated with PFP. Giving rise to an HDT/MHDA-PFP film..... 88

Figure 35 (A) AFM amplitude and (B) SKPFM surface potential of an HDT monolayer patterned and backfilled with MHDA using the standard procedure: the acid terminated sections of the

patterned monolayer activated with PFP, followed by reaction with DAH to form an HDT/MHDA-DAH film. ....	89
Figure 36 XPS confirmation of the patterned multilayer development. (A) is the N <sub>1s</sub> , and (B) is the F <sub>1s</sub> lines for an HDT monolayer that was patterned and backfilled with MHDA (black line), then the acid terminated molecules are activated with PFP (red line), and then reacted with DAH (blue line). C <sub>1s</sub> , Au <sub>4f</sub> , S <sub>2p</sub> and O <sub>1s</sub> can be found in the appendix. ....	90
Figure 37 Scheme of corannulene 1, sumanene 2, 1,4-dihydro-as-inaceno[2,1,8,7-cdefg]pyrene 3, and 1,6-dihydrodicyclopenta[ghi,pqr]perylene 4. Reproduced with permission from author. <sup>12</sup> ..	99
Appendix Figure 1 Analytical HPLC chromatograms of purified peptides 1-3 and peptoids 4-6. ....	102
Appendix Figure 2 Representative N <sub>1s</sub> , S <sub>2p</sub> , and Au <sub>4f</sub> XPS spectra for peptides 1-3. ....	103
Appendix Figure 3 Representative N <sub>1s</sub> , S <sub>2p</sub> , and Au <sub>4f</sub> XPS spectra for peptoids 4-6 and control dodecanethiol (DDT). ....	104
Appendix Figure 4 Representative raw DART PFM data for analysis of a self-assembled monolayer of DDT on gold. (A) Chemical structure of DDT. (B) Height image from DART-PFM measurement at an applied voltage of 1.5 V. (C) Images depicting q-corrected DART amplitude ( $\Delta t$ ) at the indicated applied voltage. (D) Histogram analysis of the images shown in panel (C). (E) Linear regression of the histograms in panel (D) vs applied voltage; equation for the best-fit line is shown, in which $d_{33}$ is the slope. ....	105
Appendix Figure 5 Representative raw DART PFM data for analysis of a self-assembled monolayer of peptide 1 on gold. (A) Chemical structure of peptide 1. (B) Height image from DART-PFM measurement at an applied voltage of 1.5 V. (C) Images depicting q-corrected DART amplitude ( $\Delta t$ ) at the indicated applied voltage. (D) Histogram analysis of the images shown in	

panel (C). (E) Linear regression of the histograms in panel (D) vs applied voltage; equation for the best-fit line is shown, in which  $d_{33}$  is the slope..... 106

Appendix Figure 6 Representative raw DART PFM data for analysis of a self-assembled monolayer of peptide 2 on gold. (A) Chemical structure of peptide 2. (B) Height image from DART-PFM measurement at an applied voltage of 1.5 V. (C) Images depicting q-corrected DART amplitude ( $\Delta t$ ) at the indicated applied voltage. (D) Histogram analysis of the images shown in panel (C). (E) Linear regression of the histograms in panel (D) vs applied voltage; equation for the best-fit line is shown, in which  $d_{33}$  is the slope..... 107

Appendix Figure 7 Representative raw DART PFM data for analysis of a self-assembled monolayer of peptide 3 on gold. (A) Chemical structure of peptide 3. (B) Height image from DART-PFM measurement at an applied voltage of 1.5 V. (C) Images depicting q-corrected DART amplitude ( $\Delta t$ ) at the indicated applied voltage. (D) Histogram analysis of the images shown in panel (C). (E) Linear regression of the histograms in panel (D) vs applied voltage; equation for the best-fit line is shown, in which  $d_{33}$  is the slope..... 108

Appendix Figure 8 Representative raw DART PFM data for analysis of a self-assembled monolayer of peptoid 4 on gold. (A) Chemical structure of peptoid 4. (B) Height image from DART-PFM measurement at an applied voltage of 1.5 V. (C) Images depicting q-corrected DART amplitude ( $\Delta t$ ) at the indicated applied voltage. (D) Histogram analysis of the images shown in panel (C). (E) Linear regression of the histograms in panel (D) vs applied voltage; equation for the best-fit line is shown, in which  $d_{33}$  is the slope..... 109

Appendix Figure 9 Representative raw DART PFM data for analysis of a self-assembled monolayer of peptoid 5 on gold. (A) Chemical structure of peptoid 5. (B) Height image from DART-PFM measurement at an applied voltage of 1.5 V. (C) Images depicting q-corrected DART

amplitude ( $\Delta t$ ) at the indicated applied voltage. (D) Histogram analysis of the images shown in panel (C). (E) Linear regression of the histograms in panel (D) vs applied voltage; equation for the best-fit line is shown, in which  $d_{33}$  is the slope..... 110

Appendix Figure 10 Representative raw DART PFM data for analysis of a self-assembled monolayer of peptoid 6 on gold. (A) Chemical structure of peptoid 6. (B) Height image from DART-PFM measurement at an applied voltage of 1.5 V. (C) Images depicting q-corrected DART amplitude ( $\Delta t$ ) at the indicated applied voltage. (D) Histogram analysis of the images shown in panel (C). (E) Linear regression of the histograms in panel (D) vs applied voltage; equation for the best-fit line is shown, in which  $d_{33}$  is the slope..... 111

Appendix Figure 11 Suggested  $V_{DC}$  sweep technique on non-fixed polar piezoelectric materials in which the remnant polarization switches under the coercive field. .... 112

Appendix Figure 12 Relationship between tip response and  $k_l$  for various SAMs using AFM levers with spring constants from 0.02-2.8 N/m, for (a) DDT, (b) MUA, (c) peptide A and (d) peptoid B respectively. The best-fit line is to  $y = a + bx^c$ . .... 113

Appendix Figure 13 Relationship between tip response and  $k_c$  for various SAMs using AFM levers with spring constants from 0.02-2.8 N/m, for (a) DDT, (b) MUA, (c) peptide A and (d) peptoid B respectively. The best-fit line is to  $y = a + bx^{-1}$ . .... 114

Appendix Figure 14 Relationship between tip response and  $k_c$  for various SAMs using AFM levers with spring constants from 0.02-2.8 N/m, for (a) DDT, (b) MUA, (c) peptide A and (d) peptoid B respectively. The best-fit line is to  $y = a + bx^c$ . A replotting of Figure 2 from the main text but in log linear scaling to emphasize the asymptotic nature of the fits. .... 115

Appendix Figure 15 PFM tip response from  $V_{DC}$  sweep technique on PZT at 3.0  $V_{AC}$  with R2 levers (2.8 N/m). The resulting slope of the fit was 5.51 pm/ $V_{DC}$  with an  $R^2$  value of 0.704. With a calculated  $d_{eff}$  of 143 pm/ $V_{AC}$ . ..... 117

Appendix Figure 16 (a) PFM tip response from  $V_{DC}$  sweep technique on ZNO with TRS levers (0.09 N/m) at varying  $V_{AC}$ . (b) DC- dependent response. (c) PFM response from  $V_{AC}$  at indicated  $V_{DC}$ . (d) Measure  $V_{CPD}$  as a function of  $V_{AC}$ . ..... 118

Appendix Figure 17 PFM tip response from  $V_{DC}$  sweep technique on PPLN at various  $V_{AC}$  using R2 levers (2.8 N/m). (a) and (b) represent measured response of PPLN with phase up (+180°) and phase down (-180°) respectively..... 120

Appendix Figure 18 Calibration curve for the total energy exposure to a sample surface with a source-sample distance of 2.5 cm from a 175 W source for a given period..... 121

Appendix Figure 19 Calibration curve for the total energy exposure to a sample surface with a source-sample distance of 10.0 cm from a 175 W source for a given period..... 122

Appendix Figure 20 TEM images of three mesh type TEM grids used as photomasks (a) 400 square mesh, (b) 2000 square mesh, and (c) 2000 circular mesh..... 122

Appendix Figure 21 Rate of change in the incident intensity over a change in source-sample distance for a 175 W metal halide light source measured at  $\lambda = 380$  nm fitted to a fixed exponent of -2..... 123

Appendix Figure 22 SKPFM surface potential ( $V_{CPD}$ ) images of a MUA SAM patterned and backfilled with DDT using a 2000 square mesh TEM grid as the photomask. .... 124

Appendix Figure 23 SKPFM surface potential ( $V_{CPD}$ ) images of a MUA SAM patterned and backfilled with DDT using a 2000 circular mesh TEM grid as the photomask. .... 124

Appendix Figure 24 SKPFM amplitude scans of a MHDA SAM patterned and backfilled with DDT using a 2000 square mesh TEM grid as the photomask as a factor of sample age with (a) 1 day, (b) 7 days, (c) 30 days, (d) 57 days, (e) 91 days, (f) 127 days, and (g) 171 days. .... 125

Appendix Figure 25 SKPFM surface potential ( $V_{CPD}$ ) scans of a MHDA SAM patterned and backfilled with DDT using a 2000 square mesh TEM grid as the photomask as a factor of sample age with (a) 1 day, (b) 7 days, (c) 30 days, (d) 57 days, (e) 91 days, (f) 127 days, and (g) 171 days. .... 126

Appendix Figure 26 SKPFM surface potential ( $V_{CPD}$ ) histograms of a MHDA SAM patterned and backfilled with DDT using a 2000 square mesh TEM grid as the photomask as a factor of sample age with (a) 1 day, (b) 7 days, (c) 30 days, (d) 57 days, (e) 91 days, (f) 127 days, and (g) 171 days. .... 127

Appendix Figure 27 XPS  $S_{2p}$  spectrum for monitoring the oxidation of S in an Au-thiol SAM of DDT. The black trace relates to a freshly prepared DDT SAM, and the red track is the same SAM after one week of exposure to ambient conditions. The blue trace represents a freshly prepared DDT SAM with the pink trace correlating to the same SAM after one week in an evacuated desiccator shielded in an Al foil wrapped Petri dish..... 128

Appendix Figure 28  $C_{1s}$  lines for multilayer confirmation by XPS..... 129

Appendix Figure 29  $Au_{4f}$  lines for multilayer confirmation by XPS..... 129

Appendix Figure 30  $S_{2p}$  lines for multilayer confirmation by XPS..... 130

Appendix Figure 31  $O_{1s}$  lines for multilayer confirmation by XPS. .... 130

## Preface

The long road to completion of my formal training in chemistry has had many ups and downs, but would not have been possible without the love, support and encouragement of many people over the years. This journey has shaped and molded me more than I can realize but has given me the ability to look at any situation and search for solutions instead of admitting defeat.

I would first like to thank my wife, Laura, who has been with me through every step of this journey from my first class in college more than a decade ago to long days of working while completing a master's degree, up to the completion of my Ph.D. Without your love and unending support over the years none of this would have been possible and for that I will forever be in our debt. To my children who have brought more meaning to my life than you will ever comprehend, thank you for being the loving bundles of joy that you are.

I would also like to thank the many mentors and advisors that I have had over the years for without your insights and wisdom this journey would have been would have been far more treacherous. Dr. Hutchison has seen me through these last few years helping and guiding and allowing me to grow as a researcher through my time here at Pitt. To Dr. Horne, Dr. Waldeck, and Dr. Levy, thank you for helpful guidance, questions, and contributions to my development as a scientist over the years. Thank you to Dr. Lake and Dr. Luderer who guided me and supported me through the completion of my master's and bachelor's degrees. Finally, I would like to thank Dr. Hung and Dr. Ma without whom I may have not taken the leap to pursue my Ph.D., but with your guidance and encouragement, I have been able to achieve what few have.

Lastly, I would like to thank my parents, sister, family and friends for your unending support and kind words of encouragement as I have progressed through this journey.

## **1.0 Introduction**

The goal of the research here in was to establish routes to soft-flexible organic-based molecular monolayers with high conversion efficiencies between electrical and mechanical energy. The following chapter will serve as an introduction and overview of materials whose response to electrical and mechanical stressors are invariably coupled and form the foundation for this thesis.

## **1.1 General Background**

### **1.1.1 Basics of Electromechanical Coupling**

At the nanoscale, the response of a material to outside stressors are often coupled. Piezoelectric materials are a class of these coupled materials in which their response to mechanical and electrical stressors are linked. This phenomenon has led to a wide range of applications from sensing, to high precision motors, and energy harvesting devices.<sup>1-6</sup> These applications have divided piezoelectric materials into three classes of materials: ceramics and inorganic crystals with polar unit cells, synthetic or natural polymers with polar domains, and solid forms of polar organic molecules.<sup>2, 4, 7-10</sup> The degree of polarization and electromechanical coupling within these materials determines the magnitude of their piezo activity.

### 1.1.1.1 Piezoelectricity

Piezo activity rises from electromechanical coupling in non-centrosymmetric polar materials. This phenomenon arises as either a direct-piezo effect, in which an applied mechanical stress induces an internal strain which is released in the form of an electrical current (pC/N) or the converse effect, in which the developed internal strain from an applied electrical stress causes mechanical deformation of the material (pm/V).<sup>4, 7, 8</sup> Therefore, the larger the mechanical or electrical stressor, the larger the internal strain and correlating piezo response will be. Both effects should match one another, but unless otherwise indicated the piezo response of a material will be measured from the converse effect and reported in pm/V. Equation 1.1 highlights that interconversion between the two sets of units in which C is coulombs, N is the mechanical force in newtons, V is the electrical stress in volts, F is farads, J in joules, and m is meters.

$$\frac{pC}{N} = \frac{pV * F}{N} = \frac{pV * J}{N * V^2} = \frac{pJ}{N * V} = \frac{pm}{V} \quad \text{Eq. 1.1}$$

This coupling is represented by the piezoelectric charge constant  $\mathbf{d}_{ij}$ . Here  $i$  is the direction of the applied stressor and  $j$  is the direction of the resulting stress inside the material. In example when both the stress and developed strain are in the z-axis the piezoelectric coefficient is represented as  $d_{33}$ .

A related metric is the piezoelectric voltage constant  $\mathbf{g}_{ij}$  in volt meters per newton (Vm/N), in which  $i$  and  $j$  are derived based on the directions of the applied stress and resulting internal strain, is the ratio of the magnitude of the piezo response to the stress applied.<sup>7</sup>

$$g_{ij} = \frac{d_{33}}{\epsilon} \quad \text{Eq. 1.2}$$

In which  $d_{33}$  is the piezoresponse in the z-axis to an applied stress in the z-axis over the relative permittivity of the material,  $\epsilon$ . When  $g_{ij}$  is large, a higher voltage difference will be created compared to materials that simply have a high  $d_{ij}$ . The difference between the two coefficients lends a high  $d_{ij}$  materials to be better suited for actuator type applications and high  $g_{ij}$  to be best applied in sensing applications, such as strain indicators.<sup>1, 7</sup>

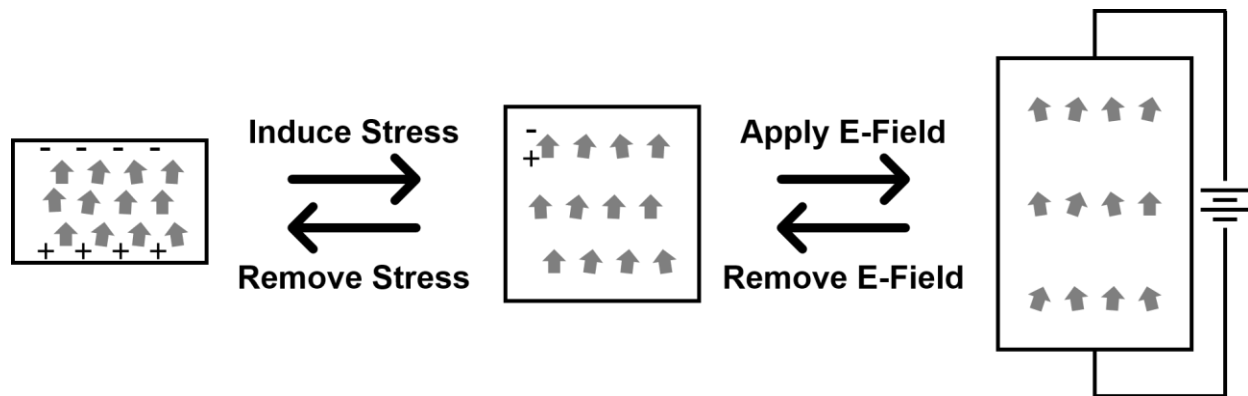


**Figure 1** Schematic of the piezoelectric effect from left to right: the direct piezoelectric effect, steady state, and converse piezoelectric effect; in which the arrows represent individual dipoles.<sup>7</sup>

### 1.1.1.2 Classical Piezoelectric Materials

Classical piezoelectric materials include hard ceramics and polymers, for example lead zirconium titanate (PZT), zinc oxide (ZnO), and polyvinylidene difluoride (PVDF). Here the application of mechanical stress causes strain developed through the repulsions within the aligned dipoles of their polar unit cells resulting in the generation of an electrical field known as the direct piezoelectric effect.<sup>2, 4, 7, 8</sup> Inversely, when an electrical field driven stress is applied to these polar materials a mechanical deformation is generated to reduce the strain generated by the stressor, the indirect piezo effect.<sup>7</sup> The magnitude of the piezoelectric response is dependent on the degree of alignment of the material's dipoles and the Young's modulus of the material.<sup>11, 12</sup>

### 1.1.1.3 Piezoelectricity in Ceramic and Crystalline Materials

For polar and non-polar ceramic/crystalline materials to exhibit piezoelectric electromechanical coupling, the material's crystalline structure must be non-centrosymmetric, poorly conducting, and exhibit a net polarization under an applied stress.<sup>2,7,8</sup> Twenty of the thirty-two crystal classes exhibit direct piezoelectric response to applied mechanical stressors. For most of these materials to exhibit piezoelectric response a net overall polar order must be induced. This net polarization is accomplished through a polling process; where a large directional electric field is applied to the material to induce and align the dipole moments of the unit cells. Once this process is completed the polarization of the unit cells are collectively aligned within the crystalline structure. This generates a net dipole moment within material.<sup>2</sup> This process has been exhibited in perovskite crystalline materials such as lead zirconium titanate (PZT) and its copolymers. Zinc oxide (ZnO) and silicon dioxide (quartz) are examples of natural non-centrosymmetric crystalline materials that exhibit intrinsic piezo response without polling.<sup>2</sup>

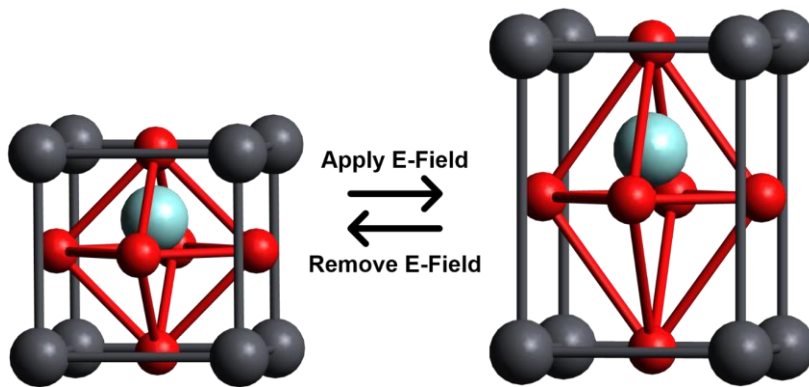


**Figure 2** Illustration of lead zirconium titanate (PZT) P4mm crystal lattice under zero field on the left and example deformation under an applied electric field on the right. In which the grey spheres represent lead atoms, red represents the oxygen atoms, and light blue represent either zirconium or titanium.<sup>2</sup>

### 1.1.1.4 Piezoelectricity in Organic Materials

As mentioned above, there are many organic polymers that can be poled to yield net polar order giving rise to piezoelectric character. There are many naturally occurring piezoactive materials; who's piezo character stems from either the natural dipole of the material or inter/intra molecular bonding such as hydrogen bonding, examples including cellulose, collagen, polyvinylidene difluoride (PVDF), etc.<sup>1, 7, 11, 13, 14</sup>

### 1.1.1.5 Ferroelectricity

Ferroelectric materials like piezoelectric materials possess directional polarization of their dipoles. This subset of piezoelectric materials carries a net dipole moment whose direction can be manipulated by a threshold electrotonic field termed a coercive field.<sup>2, 6</sup> This threshold field allows the spontaneous flipping of the material's net dipole moment. This dipole moment manipulation results in a hysteresis loop in which the direction of the net dipole manipulation remains after the field is removed. The progression from dielectric (linear response to applied field with no dipole memory), to paraelectric (nonlinear response to applied field with no dipole memory), to ferroelectric (nonlinear response to applied field with remnant dipole memory) is demonstrated in the **Figure 3**.<sup>2, 6</sup>

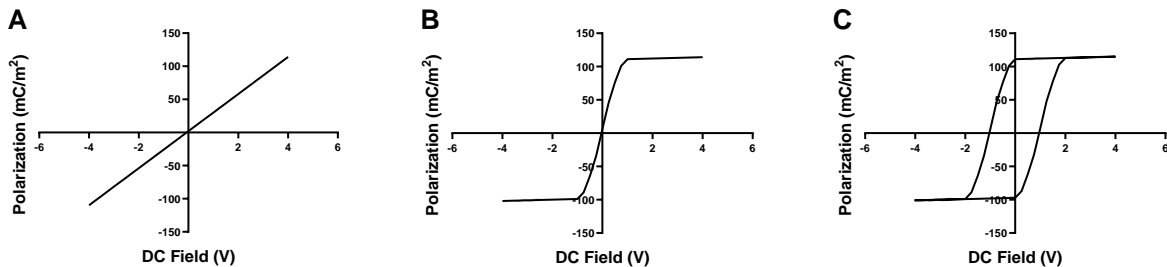


**Figure 3** Example responses from (a) dielectric materials, (b) paraelectric materials, and (c) ferroelectric materials.<sup>2</sup>

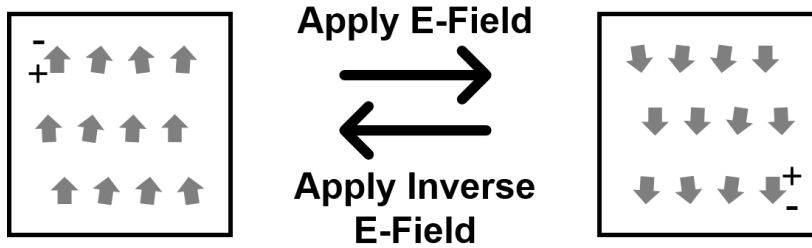


**Figure 4** Schematic of ferroelectricity where the net polarization is manipulated by the application of an external electric field, in which the grey arrows represent individual dipoles.<sup>2,7</sup>

#### 1.1.1.6 Alternative Forms of Electromechanical Coupling

##### *Electrostriction*

Electrostriction is the nonlinear coupling between an applied electric-field stress and material response. This quadratic response, developed strain, to an applied stress is present in many dielectric materials. In this case the application of stress causes the unaligned dipoles of the material to become increasingly aligned with the increasing magnitude of the applied stress, illustration below.<sup>1,7</sup> This effect, though present in piezoelectric materials, is generally small and inconsequential in comparison to the piezoelectric effect, which is linear in nature distinguishing it from electrostriction.

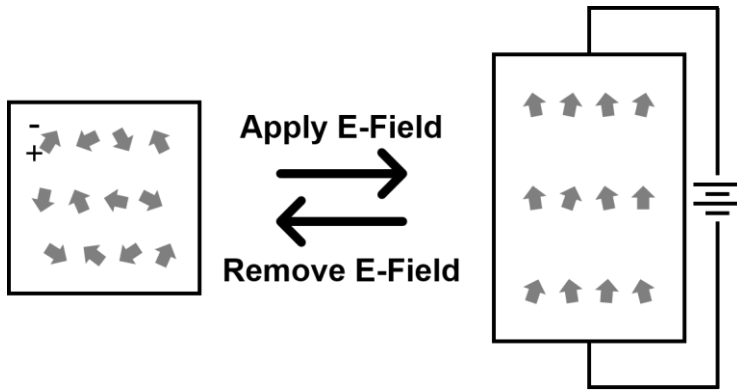


**Figure 5** Schematic of electrostriction in which an applied electric field induces a temporary alignment of the polar units in a material creating a macrodipole moment in the material by which the material deforms in reaction to, in which the arrows represent individual dipoles.<sup>7</sup>

### *Flexoelectricity*

Flexoelectricity is a non-linear coupling between an applied mechanical stress and material response, in which a stress-strain gradient is established by the non-uniform deformation of a material. This gradient induces electromechanical coupling by either breaking centrosymmetry of a material or bringing the dipoles into a net alignment, **Figure 6**. Unlike piezoelectricity and electrostriction flexoelectricity is size-dependent, from an insignificant effect in large bulk scale materials  $\geq \text{mm}^3$  moving to becoming a sizable effect in some nano-scale materials such as lipid bilayers.<sup>7</sup>

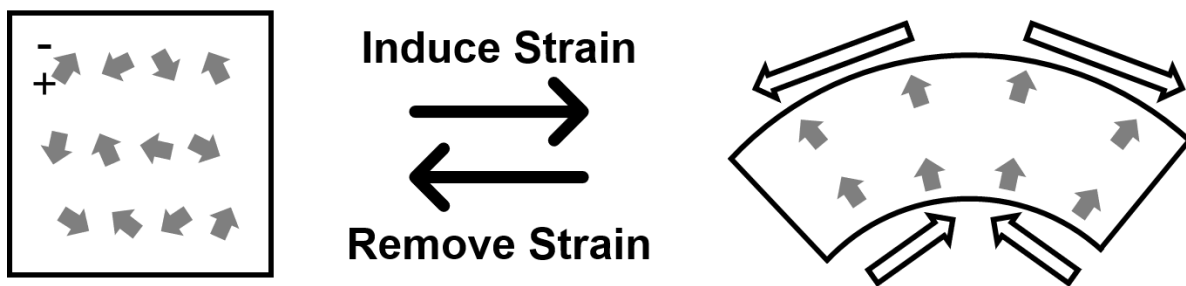


**Figure 6** Schematic of flexoelectricity, in which the arrows represent individual dipoles.<sup>7</sup>

## *Electrostatic*

The electrostatic effect (triboelectric effect) is the mechanical deformation in a material resulting from the Coulombic force generated between two separated charges. This non-linear effect can occur when two different materials are brought into close contact with each other generating a local electric field. The electrostatic effect can contribute to the magnitude of the measured piezoelectric effect but can be deconvoluted from the measurement due to its non-linearity and small contribution to the overall response.<sup>7</sup>

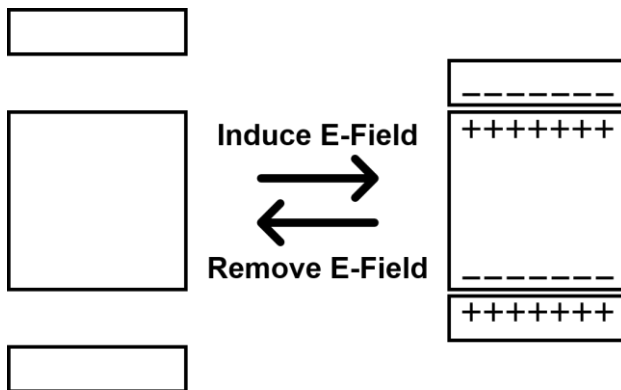


**Figure 7** Schematic of the electrostatic effect.<sup>7</sup>

## 1.2 Self-Assembled Monolayers

Self-assembled monolayers (SAMs) are widely used with applications in electronic devices.<sup>3,4,7,11,15</sup> SAMs are a subset of organic thin films where a single layer of organic molecules are deposited on a substrate generally by direct deposition from solution or by chemical vapor deposition (CVD).<sup>4,7</sup> We will focus on SAMs that are grown from solution onto a solid substrate (the defining difference between SAMs and Langmuir-Blodgett films).<sup>4,7</sup>

SAMs are prepared from solution when a solute, with a terminal group possessing a high affinity for the submerged substrate, chemisorbs to the substrate.<sup>3,4,7,11,16</sup> For most of this work, we will focus on thiol terminated alkanes which have a high affinity for evaporated Au (111) substrates. The Au (111) is the lowest energy surface of Au which can have minor crystalline defects caused by deposition and annealing treatments, but these defects should not affect analysis by atomic force microscopy (AFM).<sup>1</sup> The sulfur atoms will assemble from solution into a  $\sqrt{3}\times\sqrt{3}$  superlattice on top of the Au surface.<sup>16,17</sup>

SAMs grow from solution in three steps as illustrated in **Fig. 8**. First, the molecule adsorbs to the surface in a lying down fashion. During the initial phase (1), molecular surface density is approximately 30% of a final fully packed monolayer because the molecules are mostly “lying down” on the surface. Next (phase 2), the high-affinity head group chemisorbs to the surface and the molecules begin to stand up.

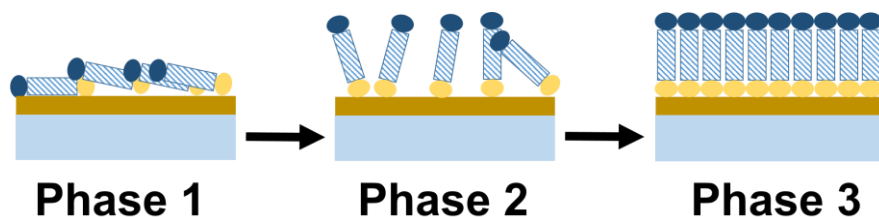


**Figure 8** Schematic of the phases for the formation of self assembled monolayers (SAMs).<sup>16</sup>

The molecules assemble “standing up” along the surface normal opening additional surface sites allowing more molecules to bond, thus increasing the packing density. The final step (phase 3) occurs when the molecules reorganize across the surface, due to imperfect substrates, creating molecular “islands” depositing on the edges. Step one occurs in a matter of seconds while steps 2 and 3 will occur over several minutes to several hours respectively.<sup>16</sup> Allowing time for all three phases to complete provides for a uniform monolayer with calculable packing densities and film thicknesses. Hence, part of the attraction of SAMs is their simplicity to be grown directly from solution while only requiring a clean substrate and relatively dilute millimolar-range solutions.

## **1.3 Methodology Overview**

### **1.3.1 Scanning Probe Microscopy**

The first scanning probe microscope (SPM) invented by Binnig and Rohrer in 1981-1982, Nobel Prize 1986, was a scanning tunneling microscope (STM). SPMs use a sharp probe brought within near contact to a surface to probe atomic scale properties of materials.<sup>12</sup>

#### **1.3.1.1 Topography**

Topographical SPM is characterized by the treatment of the probe during the experiment. In contact topographic SPM the probe is brought into near contact with the surface of the sample and is rastered across it in the x- and y-axis. Here the probe is not driven, and the magnitude of the force required to maintain constant pressure of the cantilever in the z-axis is recorded as the magnitude of the variance in the topography of the sample. In contrast tapping topographic SPM again brings the probe into near contact with sample surface but instead of dragging the probe across the surface like a record player and recording the deflection of the probe, instead the probe is driven by a piezoelectric actuator at the fundamental resonance frequency of the probe. The change in the frequency of the driven probe is then correlated to changes in the topography of the sample. With ideal conditions these mechanisms garner SPM atomic scale resolution of topographic features.<sup>12</sup>

### **1.3.1.2 Scanning Kelvin Probe Microscopy**

Scanning Kelvin Probe Microscopy (sKPFM) incorporates the principles of topographical SPM with an additional raster scan of the surface; during which the conductive probe is held at a set delta height above the surface. During the secondary raster a static DC field is established between the offset probe and the surface. As the probe is scanned over the sample changes in the surface potential of the sample will cause the probe to deflect. This deflection is then processed through a feedback loop where the DC field applied to the probe is adjusted to cancel out this deflection. The magnitude of the field required to cancel out the deflection of the probe is proportional to the surface potential of the sample. Additionally, if the work function, the minimum energy needed to move an electron from the sample to vacuum space outside of the sample, of the probe is known sKPFM can be used to determine the work function of the sample as well.<sup>12</sup>

### **1.3.1.3 Piezo Force Microscopy**

Piezoresponse force microscopy (PFM) was developed to probe the nano-scale morphological response of a sample to an applied electrical field.<sup>11, 12, 18</sup> PFM evaluates the converse piezoelectric effect by measuring sample deformation under an applied bias. The bias (generally AC) is applied through a conductive lever that induces periodic displacements in the material due to the converse piezoelectric effect. Traditionally this is known as single-frequency PFM (SF-PFM) where a lock-in amplifier is tuned to a single frequency either the amplitude or phase signal channels. Single frequency PFM suffers from low sensitivity and poor frequency tracking from crosstalk arising from the material's topography.<sup>11, 18</sup> This hindrance was initially compensated for by using large field constants to induce large responses from materials to boost the signal to noise ratio creating more stable measurements. Though this technique increases sensitivity it can suffer from the dielectric break down of either the target material or the cantilever

effectively reducing the reproducibility of experiments. To increase sensitivity and avoid dielectric breakdown of materials dual AC resonance tracking PFM (DART-PFM) was developed by Kalinin to allow the use of small bias voltages while maintaining good frequency tracking despite varying topographical features.<sup>18, 19</sup> Building on the principles of SF-PFM DART-PFM uses contact resonance to enhance the sensitivity of the PFM measurement coupled with a dual frequency feedback loop that tracks the variation in the amplitude of the contact resonance peak. Though an improvement over SF-PFM DART-PFM is still subject to distortions from electrostatics hindering the ability to acquire purely quantitative measurements.<sup>11, 12, 18, 19</sup>

### **1.3.2 X-Ray Photoelectron Spectroscopy**

X-Ray photoelectron spectroscopy (XPS) utilizes x-ray photons of a characteristic energy impinging on a surface. The massless photons interact with core electrons of the atoms in the sample surface. Upon collision the photons induce an ionized state in the atoms from which a photoelectron is ejected upon the return to the ground state. The ejected photoelectron carries a kinetic energy that is equivalent to the difference between the energy of the impeding photon and the binding energy of the ejected electron. XPS is primarily a surface sensitive technique with a maximum sampling depth of only a few nanometers. This is due to the short attenuation length of the incident photon and the high probability of an energy loss event, e.g. reabsorption of the ejected photoelectron. Though limited in sampling depth XPS is a very powerful analytical method allowing for the determination of even the most minute changes in the chemical environment surrounding an individual atom.<sup>20</sup>

### 1.3.2.1 XPS for Packing Density Determination in Self Assembled Monolayers

The XPS methodology for the determination of surface packing density in SAMs was developed by Weidner *et al.* Here Weidner describes the use of a SAM with a known packing density and similar distinctive characteristics to the unknown sample to establish the attenuation of the substrate signal based on surface coverage. An example implemented later in chapter 2 is the use of a dodecanethiol SAM on Au with a known packing density of  $4.62 \times 10^{14}$  molecules per  $\text{cm}^2$  as the reference material for unknown systems utilizing the same characteristic Au-Thiol anchoring motif. This allows the assignment of the known packing density of DDT to the ratio of the sulfur and gold peak maxima, at 162 eV and 84 eV respectively. This ratio establishes the attenuation of the Au signal for given surface coverage. The Au/S ratio of the unknown can then be compared to the reference ratio of the known sample allowing for the determination of the surface packing density of unknown sample.<sup>20, 21</sup>

## 2.0 Influence of Molecular Structure on a Self-Assembled Monolayer's Piezoresponse

This chapter has been adapted with permission from:

- Marvin, C. W.\*; Grimm, H. M.\*; Miller, N.C.; Horne, W. S.; Hutchison, G. R. Interplay Among Sequence, Folding Propensity, and Bio-Piezoresponse in Short Peptides and Peptoids. *J Phys. Chem. B* 2017, 121(44), 10269-10275 (\* equal author contribution)

### 2.1 Contributions

A collaborative effort with Christopher W. Marvin, Haley M. Grimm, and Geoffrey R. Hutchison whose individual contributions are as follows:

*Christopher W. Marvin developed and applied the AC voltage DART-PFM sweep methodology to the self-assembled monolayers to determine the piezo coefficients of the design materials. Haley M. Grimm isolated the synthesis protocols for the development of tailored peptide and peptoid sequences. Geoffrey R. Hutchison carried out density functional theory calculations on peptide and peptoid helices to ascertain the net macrodipole of the tailored organic molecules.*

## 2.2 Introduction to Tailored Organic Molecular based Piezoelectric Materials

Piezoelectric materials interconvert between electrical and mechanical energy, generating electric charge in response to mechanical stress (the direct piezoelectric effect) and undergoing deformation under an applied field (the converse piezoelectric effect).<sup>1</sup> Because piezoelectric materials allow direct mechanical to electrical conversion, they find wide use in touch and force sensors,<sup>2</sup> microscale actuators,<sup>3</sup> and related components. Devices utilizing such components have applications in areas from consumer to medical to military.<sup>4,5</sup>

Many bulk inorganic materials are piezoelectric, including lead zirconate titanate (PZT) perovskites,<sup>6</sup> zinc oxide,<sup>7</sup> and quartz.<sup>8</sup> Piezo response has also been shown in organic polymers such as polyvinylidene difluoride (PVDF).<sup>9</sup> While most applications have focused on the above materials due to their high responsiveness, the piezoelectric effect is a common molecular property<sup>10</sup> and is found in a number of biomaterials. As an example, proteins and their assemblies can show dramatic motion in response to environmental changes (e.g., redox, pH, chemical gradient), and this characteristic extends to applied electric fields. Prior work has shown the piezoelectric effect in collagen,<sup>11,12</sup> viruses,<sup>13</sup> aligned peptide crystals,<sup>14,15</sup> isolated peptide nanotubes,<sup>16</sup> as well as fibrils based on  $\alpha$ -helices.<sup>17</sup>

Despite widespread potential applications, limitations exist that hinder the advance of piezoelectric materials. From a practical standpoint, there is an unmet need for biocompatible materials that possess strong, stable piezo-coefficients and can be scaled to fit small devices. From a fundamental perspective, there are open questions as to what molecular properties give rise to a strong piezoelectric response. These issues are interrelated. Enhanced understanding of the mechanisms giving rise to piezo response will enable the bottom-up design of new systems that address practical needs.

## 2.3 Methods

### 2.3.1 General Information

All Fmoc  $\alpha$ -amino acids and resins used for solid phase synthesis were purchased from Novabiochem. All solvents and submonomer synthesis reagents were purchased from Sigma-Aldrich and used without further purification. Reverse phase HPLC was carried out using Phenomenex Luna C<sub>18</sub> columns. Products were eluted using gradients between 0.1% TFA in water [solvent A] and 0.1% TFA in acetonitrile [solvent B], monitored by UV detection at 220 nm and 280 nm. MALDI-TOF MS experiments were performed on a Voyager DE Pro (Applied Biosystems) or an ultrafleXtreme (Bruker) using  $\alpha$ -cyano-4-hydroxy cinnamic acid as the ionization matrix

### 2.3.2 Peptide Synthesis

Peptides **1-3** were synthesized by microwave-assisted Fmoc solid phase methods on a CEM MARS 5 microwave using NovaPEG rink amide resin (0.05 mmol scale). Resin was swelled in DMF for 15 min prior to the first coupling reaction. For a typical cycle, a 0.1 M solution of HCTU in NMP (4 equiv relative to resin, 2 mL, 0.20 mmol) was added to Fmoc-protected amino acid (4 equiv, 0.20 mmol), followed by DIEA (6 equiv, 0.30 mmol). After a 2 min preactivation, the solution was transferred to resin, and the mixture heated to 90 °C over 1.5 min, followed by a 2 min hold at that temperature. Fmoc deprotection was carried out by treatment with 20% 4-methylpiperidine in DMF (4 mL), and the mixture was heated to 90 °C over 2 min, followed by a 2 min hold at that temperature. The resin was washed 3 times with DMF after each coupling and

deprotection cycle. For Aib residues and those coupled to it, PyAOP (4 equiv, 0.20 mmol) was used in place of HCTU. The N-terminus of each peptide was capped with S-trityl-3-mercaptopropionic acid using the standard HCTU coupling described above. After the final coupling, the resin was washed 3 times each with DMF, DCM, and MeOH, and the resin was dried under vacuum for at least 20 min. Peptides were cleaved from resin by treatment with a solution of TFA/EDT/H<sub>2</sub>O/TIS (92.5%/3%/3%/1.5% by volume) for 3 hours followed by precipitation in cold ether. The pellets were collected by centrifugation and re-dissolved in 90:10 solvent A / solvent B for purification by preparative HPLC. The identity and purity of final products were confirmed by analytical HPLC (Figure S1) and MALDI-TOF MS (Table S1). Peptide stock solution concentrations were quantified by UV spectroscopy (Hewlett Packard 8452A Diode Array Spectrometer,  $\epsilon_{276} = 1450 \text{ cm}^{-1} \text{ M}^{-1}$  from the single Tyr in each sequence).

### 2.3.3 Peptoid Synthesis

Peptoids **4-6** were synthesized using a microwave-assisted submonomer solid phase approach on a CEM MARS 5 microwave using cysteamine 2-chlorotrityl resin (41.4 mg, 0.06 mmol). Resin was swelled in DCM for 30 min, then washed with DMF prior to the synthesis. In a typical cycle, a solution of 1.2 M bromoacetic acid in dry DMF (1.0 mL, 1.2 mmol) was added to resin, followed by DIC (188  $\mu\text{L}$ , 1.2 mmol). The reaction was heated to 35 °C over 2 min, followed by a 2 min hold at that temperature. The resin was washed three times with DMF, followed by addition of a 1.5 M solution of primary amine (*R*-(+)- $\alpha$ -methylbenzylamine or 2-methoxyethylamine) in NMP (1.6 mL, 2.4 mmol). The mixture was then heated to 90 °C over 2 min, followed by a 2 min hold at that temperature. The resin was washed again with DMF (3x) prior to the next cycle. The N-terminus of each peptoid was capped by treatment of resin with a

solution of DMF (800  $\mu$ l), DIEA (200  $\mu$ l), and acetic anhydride (100  $\mu$ l) and stirring at ambient temperature for 20 min. The resin was then washed 3 times each with DMF, DCM, and MeOH, and dried under vacuum for at least 20 min. Each peptoid was cleaved from resin by treatment with a mixture of TFA/H<sub>2</sub>O/TIS (95%:2.5%:2.5% by volume) for 30 min. The cleaved peptoid solution was diluted in H<sub>2</sub>O, lyophilized, and re-dissolved in 50:50 solvent A / solvent B for purification by preparative HPLC. The identity and purity of final products were confirmed by analytical HPLC (Figure S1) and MALDI-TOF MS (Table S1). Peptoid stock concentrations were determined by weight followed by dilution to a desired concentration.

#### 2.3.4 Circular Dichroism

CD measurements were performed on an Olis DSM17 circular dichroism spectrophotometer. Scans were performed at 20 °C from 200-260 nm with 1 nm increments, a bandwidth of 2 nm, and a 5 sec integration time. Cells with a 2 mm path length were used. Peptide solutions (50  $\mu$ M as determined by UV absorbance) were prepared in 10 mM phosphate buffer (pH 7.2). Peptoid solutions (50  $\mu$ M as determined by accurate weighing) were prepared in acetonitrile (HPLC grade). Percent helical population was calculated using a previously described method<sup>1</sup> that uses the assumption that the population only consists of two states, helical and random coil, and that the contribution to ellipticity from the random coil population is negligible at 222 nm. Fraction helical population was estimated by dividing the observed ellipticity at 222 nm,  $[\Theta_{\text{obsH}}]_{222}$ , in deg cm<sup>2</sup> dmol<sup>-1</sup> by the limiting value for ellipticity for a 100% helical backbone. The latter was calculated via the equation  $[\Theta_{\text{H}}]_{222} = 43000(1-[x/n])$ , in which n is the number of residues and x is a factor that accounts for end effects, for which a value of 2.5 was used.

### 2.3.5 Self-Assembled Monolayer Formation

Gold-thiol self-assembled monolayers (SAMs) were prepared using 1.0 mM dodecanethiol in ethanol, 1.0 mM peptide in distilled water, or 1.0 mM peptoid in acetonitrile. These solvents were chosen due to solubility of the molecule being deposited and have no impact on the production of the monolayers. Substrates consisted of gold metal deposited on glass (Thermo Scientific BioGold substrates produced by Electron Microscopy Sciences). Prior to SAM formation, substrates were cleaned by washing with ethanol and water, followed by sonication for 10 min in the corresponding solvent used for deposition (ethanol for **DDT**, water for **1-3**, acetonitrile for **4-6**). After cleaning, the substrates were dried with compressed air or N<sub>2</sub> and submerged into the solution of thiol ligand for 24 h at room temperature. The substrates were then taken out of the solution, rinsed three times with the respective solvent, blown dry, covered with aluminum foil, and placed in a desiccator for at least 1 h prior to analysis. Samples not measured immediately were stored in a desiccator, protected from light exposure.

### 2.3.6 X-Ray Photoelectron Spectroscopy (XPS)

XPS measurements were collected on a Thermo Scientific ESCALAB 250XI XPS spectrometer. Peptide, peptoid, and DDT monolayers were deposited on Thermo Scientific BioGold substrates produced by Electron Microscopy Sciences. A survey spectrum was collected at a pass energy of 150 eV and a dwell time of 10 ms. Au<sub>4f</sub> and N<sub>1s</sub> were averaged over 50 scans with a pass energy of either 100 eV for peptides **1-3** or 150 eV for peptoids **4-6** and a dwell time of 50 ms. S<sub>2p</sub> spectra were taken as an average of 100 scans with a pass energy of either 100 eV for peptides **1-3** or 150 eV for peptoids **4-6** and dwell time of 50 ms. Standard baseline subtraction,

normalization, and peak fits were performed. The surface density of each SAM was estimated using a previously published method,<sup>2</sup> in which ratio of the sulfur and gold peak maxima, at 162 eV and 84 eV respectively, were averaged across three different spots on a single SAM. The average peak ratio for a given SAM was compared to that of the measured DDT SAMs. DDT has a known packing density of  $4.62 * 10^{14}$  molecules per  $\text{cm}^2$ , which allows the surface density of each monolayer to be estimated by comparison.

### **2.3.7 Atomic Force Microscopy (AFM) and Piezo Force Microscopy (PFM)**

AFM and PFM measurements were performed using an Asylum Research MFP-3D SPM. PFM experiments were carried out using the dual-AC resonance tracing (DART-PFM) mode. Asyelec.01-R2 (Asylum Research) iridium-coated, conductive silicon probes were used for the characterization of the surface. These tips have a free-air resonance frequency of 70 kHz, but a contact resonance of  $\sim 280$  kHz. The low spring constant of 2.8 N/m was used due to the soft nature of the organic and biomaterial monolayers. Multiple tip-sample voltages from 1.5 - 4.5 V were applied for each sample, as described below. The deflection was set to -0.30 and the humidity in the sample box maintained below 30%. If ambient relative humidity was above 30%, the instrument was flushed with dry nitrogen during the measurement. For each sample, a  $1 \mu\text{m} \times 1 \mu\text{m}$  area was scanned with a scan rate of 1.0 Hz. Topography, piezoresponse amplitude, and phase images were recorded. The recorded amplitudes were q-corrected to take the tip-sample resonance amplification used by DART-PFM into account. This q-correction was performed using the default analyzing software. A histogram of the q-corrected amplitude scan was generated. The median value of the distribution was plotted versus the appropriate voltage. The slope from a linear regression of this plot for the same sample measured on the same day was used to determine a

single  $d_{33}$  value for a given compound. Multiple independent experiments performed for different samples and days provided multiple  $d_{33}$  values for each compound. These values were averaged to generate the statistics reported in Table 1.

### 2.3.8 Calculation of Dipole Moment for Model Helicies

Gaussian 09 revision D.01<sup>3</sup> was used to perform geometry optimizations using density functional theory (DFT), with the dispersion-corrected  $\omega$ B97X-D functional<sup>4</sup> and the 6-31G(d) basis set to optimize all computed structures. Initial geometries were generated using PyMol version 1.8.4<sup>5</sup> with idealized backbone dihedral angles for  $\alpha$ -helix (peptide) or PPI (peptoid) secondary structure. Computed dipole moments from DFT have been found to be highly accurate with errors in the 0.1-0.2D range.<sup>6</sup>

## 2.4 Results and Discussion

To gain insight into the molecular basis for electromechanical response in organic scaffolds, we have previously applied computational methods to probe the piezo effect of individual molecules<sup>10</sup> and hydrogen-bonded assemblies.<sup>18,19</sup> These results suggest that the two key features necessary for piezo response at the molecular level are (1) a dipole moment to couple to the applied electric field and (2) a deformable conformation along a low energy vibrational mode. Using standard solution self-assembly techniques, one can easily create monolayers with intrinsic polar order to screen molecules for the above properties (**Figure 9A**).<sup>20</sup> As a proof of concept for the above method, we recently demonstrated piezo response in simple oligo-alanine

peptide monolayers.<sup>20</sup> Comparison of the oligoalanine peptide monolayer to simple alkane monolayers indicated the conformational flexibility of the polypeptide backbone was essential for piezo response.<sup>20</sup> Not clear was the potential role of peptide folding in this effect. One possibility is that the  $\alpha$ -helix (**Figure 9B**), likely favored in the Ala-rich sequence, can act as a polar “molecular spring” that undergoes conformational deformation in an applied field. If true, this would imply a correlation between peptide helicity and the magnitude of piezo response. Here, we systematically probe the interplay among peptide chemical structure, folding propensity, and piezoelectric properties, uncovering in the process new insights into the origin of peptide electromechanical response.

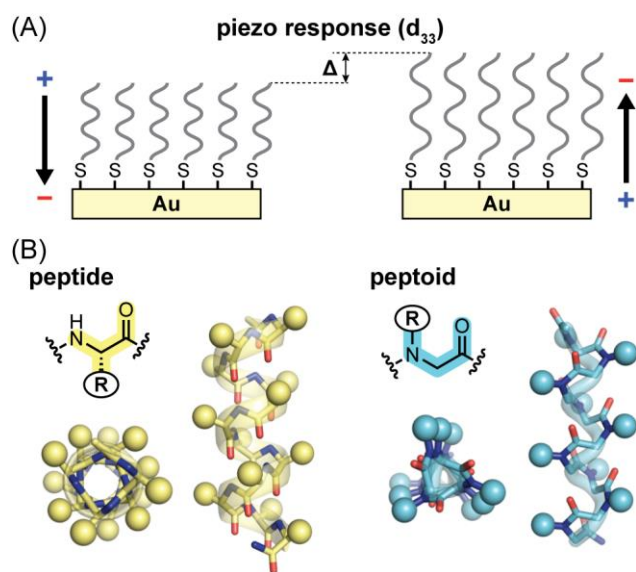
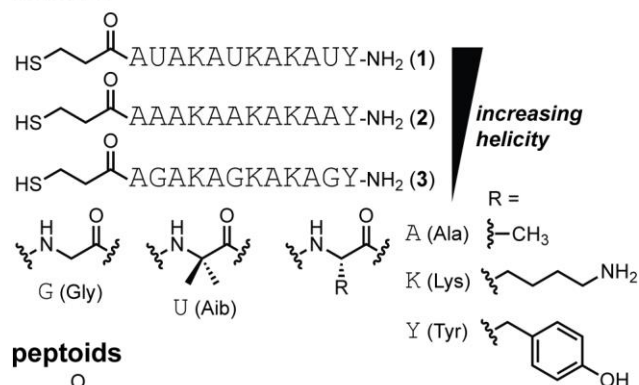


**Figure 9** (A) Schematic depicting nanoscale piezo response of a self-assembled monolayer on gold upon applying an electric field. (B) Backbone chemical structures alongside models of the  $\alpha$ -helix and PPI-helix folds formed by peptide and peptoid oligomers, respectively.

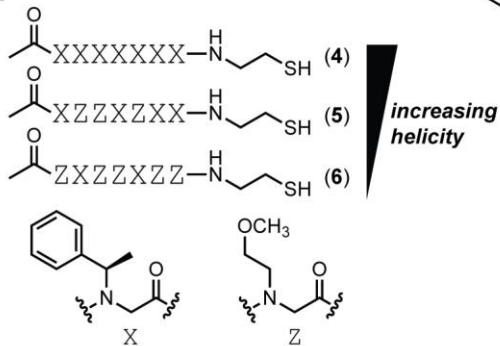
To evaluate the effect of helicity, and thus the molecular basis of peptide piezoresponse, we designed a series of peptides (**1-3**) of identical length but varying folding propensity (**Figure 10**). Keeping the molecule size comparable among the series focuses the analysis of structure-

function relationship on folding behavior. Peptide **1** is based on a previously reported sequence that is among the shortest known to show appreciable helical folded population in aqueous solution.<sup>21</sup> This characteristic results from the presence of three aminoisobutyric acid (Aib, U) residues that restrict backbone conformational freedom and promote the helical fold. We replaced the three Aib residues in **1** with either alanine (Ala, A) or glycine (Gly, G) to generate peptides **2** and **3**, respectively. Ala is also helix promoting, though to a lesser degree than Aib, while Gly is strongly helix disrupting. Each peptide was functionalized with a thiol group at the N-terminus to provide an anchor point for attachment to gold in the fabrication of polar monolayers.

### peptides



### peptoids



### control

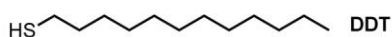


**Figure 10** Peptides **1-3**, peptoids **4-6**, and control small molecule dodecanethiol (**DDT**).

A powerful strategy complementary to sequence modification for controlling folding in peptides is to alter the chemical structure of the backbone. Many backbone compositions differing from nature can give rise to discrete folding motifs.<sup>22-25</sup> One of the first artificial scaffolds shown

to manifest such behavior is the peptoid, a variant of the  $\alpha$ -peptide backbone in which each side chain is transposed from  $C_\alpha$  to N.<sup>26,27</sup> Peptoids are intrinsically more flexible than peptides; however, incorporation of  $\alpha$ -chiral aromatic side chains such as the (*R*)- $\alpha$ -methylbenzyl moiety in residue X (**Figure 10**) gives rise to highly rigid chains that adopt polyproline-I (PPI) helical folds.<sup>26</sup>

Following logic analogous to that applied in peptides **1-3**, we designed a series of peptoids (**4-6**) of identical length but systematically altered helicity by combining known structure-promoting (X) and structure-disrupting (Z) residues in varying fractions.<sup>28,29</sup> The macrodipole of the PPI helix ( $\delta^+$  toward C-terminus) is oriented opposite that of a the  $\alpha$ -helix ( $\delta^+$  toward N-terminus). To keep the alignment of the helix dipole the same in the polar monolayers across the oligomers examined, we placed the thiol for anchoring to gold at the C-terminus in the peptoid series through incorporation of a terminal cysteamine. Density functional theory calculations indicate the macrodipole for a 12-residue peptide  $\alpha$ -helix (54 D) is approximately double that of a 7-residue peptoid PPI helix (27 D). These values assume fully folded helical states, and the magnitude of the macrodipole will vary greatly with folded structure.

Peptides **1-3** and peptoids **4-6** were prepared by standard solid-phase methods (Fmoc strategy for the peptides, submonomer approach for the peptoids). Each oligomer was purified by preparative reverse phase HPLC, and the identity and purity of the final products were confirmed by analytical HPLC and MALDI-TOF mass spectrometry (see Supporting Information [SI] for details on synthesis and purification).

To establish that relative solution folding propensity in **1-6** followed the intended trends, we used circular dichroism (CD) spectroscopy (**Figure 11**). Solvent conditions for CD measurements were selected based on the solutions used for monolayer preparation (aqueous for the peptides, acetonitrile for the peptoids). The CD spectrum of peptide **1** showed minima at 222

and ~208 nm, characteristic of right-handed helical secondary structure. Moving through the series **1-3**, the band at 222 nm decreased in magnitude and the lower wavelength signal blue shifted to ~200 nm. These changes are both diagnostic of an increase in random coil character and support our design hypothesis regarding the relative helicity across the series (**1** > **2** > **3**). Qualitative features of the CD spectra of the peptoids were consistent with the expected left-handed PPI helical fold. The decrease in the intensity of the band at 222 nm with increasing fraction of flexible Z residues supported the relative trend in helical character **4** > **5** > **6**. On an absolute scale, estimated folded populations (Table 1) vary from 3% for the least helical peptide (**3**) to ~100% for the most helical peptide (**4**).

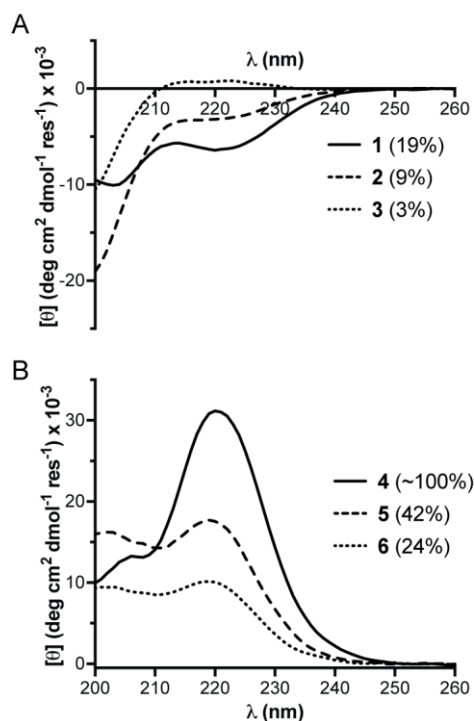


**Figure 11** CD spectra of peptides **1-3** (50  $\mu$ M in 10 mM phosphate pH 7.2) and peptoids **4-6** (50  $\mu$ M in acetonitrile). Estimated helical folded population for each compound is indicated in parentheses.

To compare the electromechanical response of the peptides and peptoids, monolayer films were deposited by solution self-assembly on gold substrates. Using dual AC resonance tracking piezoresponse force microscopy (DART-PFM), we determined the change in thickness ( $\Delta t$ ) of each film over a series of applied voltages (1.5 to 4 V) averaged across a  $1 \mu\text{m}^2$  area. The slope from a linear fit to a plot of  $\Delta t$  vs. applied voltage provides a measure of the piezoelectric response along the polarization axis ( $d_{33}$ ). Ideally, the intercept of this line would pass through zero (i.e., no mechanical response with no applied field); however, due to electrostatic and tip-sample interactions, that is rarely the case. We repeated this experiment for each oligomer across independently prepared films on multiple days using different tips (**Figure 12, Table 1**). Averaging across multiple samples and tips minimizes artifacts arising from tip-surface interactions; and averaging across a large area (rather than a single point) for each measurement samples an ensemble of different molecular conformations and monolayer packing motifs. The validity of the methodology was supported by the determination of the piezo response of quartz by the same approach, yielding a  $d_{33}$  ( $3.8 \text{ pm V}^{-1}$ ) close to the known value for  $d_{11}$  ( $2.3 \text{ pm V}^{-1}$ ).<sup>8</sup> We note that in general, across all monolayers of **1-6**, the distribution of piezo response showed high positive skewness, which did not have a clear trend with voltage. On the other hand, for five out of six compounds (**1-3**, **4**, and **6**) the distributions yielded voltage-dependent increases in peak width and standard deviation. For peptoid **5**, three out of four samples showed slight broadening with increasing voltage.

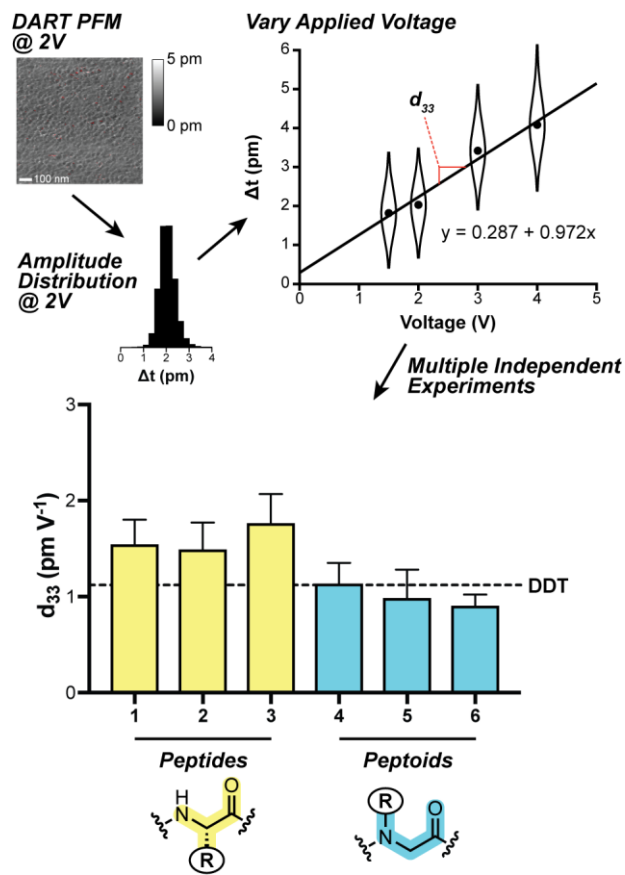


**Figure 12** Summary of DART-PFM methodology used to determine piezoelectric response (see Supporting Information for details) and the resulting  $d_{33}$  values obtained from replicate independent experiments with peptides **1-3**, peptoids **4-6**, dodecanethiol (**DDT**), and quartz. Error bars are the SEM from 4-8 independent experiments (see **Table 1**).

**Table 1** Solution folding and monolayer properties for peptides **1-3** and peptoids **4-6**.

Compound	$d_{33}$ (pm V <sup>-1</sup> ) <sup>a</sup>	$n^a$	Monolayer density (molecules cm <sup>-2</sup> x 10 <sup>14</sup> )	Fraction helical (%) <sup>b</sup>
<b>1</b>	1.53 ± 0.27	8	3.3 ± 0.4	19
<b>2</b>	1.48 ± 0.29	6	4.0 ± 0.4	9
<b>3</b>	1.75 ± 0.32	6	3.9 ± 0.4	3
<b>4</b>	1.12 ± 0.23	4	4.1 ± 0.1	100
<b>5</b>	0.97 ± 0.31	4	4.2 ± 0.1	42
<b>6</b>	0.89 ± 0.13	4	4.3 ± 0.2	24
<b>DDT</b>	1.12 ± 0.25	4	4.6 <sup>c</sup>	–
<b>quartz</b>	3.80 ± 0.50	2	–	–

<sup>a</sup> Average ± SEM for piezo coefficient ( $d_{33}$ ) as determined from  $n$  independent PFM experiments (see supporting information for details). <sup>b</sup> Fraction helicity as estimated by CD (see supporting information for details) in solution (water for **1-3**, acetonitrile for **4-6**). <sup>c</sup> From ref.<sup>30</sup>

Comparing the two different backbone compositions, the average response from monolayers of peptides **1-3** was significantly greater than that of monolayers made up of **DDT** or peptoids **4-6** ( $p$  0.016 for peptides vs peptoids). On average, peptides **1-3** yielded PFM response ~41% larger than **DDT** and ~59% larger than peptoids **4-6**. Interestingly, no statistically significant trends beyond experimental uncertainty were discernable within a given backbone (i.e., among **1-3** or among **4-6**). While one might expect both peptides **1-3** and peptoids **4-6** to yield much greater conformational flexibility than a straight-chain alkane such as **DDT**, the high packing density in the monolayers may diminish this difference. Placing these results in context of known bulk biomaterials that are piezoactive, the  $d_{33}$  of the peptide monolayers, while small, is greater than the response of bulk collagen (0.8 pm V<sup>-1</sup>),<sup>11</sup> bone (0.29 pm V<sup>-1</sup>),<sup>31</sup> and wood (0.04 pm V<sup>-1</sup>).<sup>32</sup> It is likely that the alignment and parallel arrangement of molecular dipole moments in the monolayer samples enhances piezo response. Still, the magnitudes are modest compared to crystalline

piezoelectric polymers, such as PVDF ( $\sim 30 \text{ pm V}^{-1}$ ),<sup>1</sup> molecularly-doped polyurethane foams ( $\sim 150\text{-}250 \text{ pm V}^{-1}$ ),<sup>33</sup> or PZT ceramics ( $\sim 300\text{-}500 \text{ pm V}^{-1}$ ).<sup>6</sup>

To rule out the possibility that differences in piezo response observed resulted from differences in monolayer packing density rather than molecular structure, we carried out X-ray photoelectron spectroscopy (XPS). We determined the ratio of XPS peak intensities for sulfur versus gold signals for representative monolayers of **1-6** and **DDT** (**Figure A2-A3**). Calibrating against a reported packing density for **DDT**,<sup>30</sup> we estimated the surface coverage density for the peptides and peptoids (**Table 1**). Variation among the observed packing densities were small and not sufficient to explain the observed differences in piezo response. Moreover, no significant trend was apparent based on backbone composition (peptides vs peptoids) or helicity in solution. The XPS data also served to show the chemical integrity of the peptide and peptoid monolayers and that sulfur-gold linkages were not oxidized over the course of sample preparation and storage.

## 2.5 Conclusions

In summary, the results suggest that peptide-based materials exhibiting piezo response have regions of highly aligned flexible backbones. Our initial hypothesis on the molecular basis for piezoelectric response focused on the effect of helical conformational preferences and the magnitude of the piezo response. That is, as “molecular springs,” an unstructured peptide **3** would show low response. The data here argue the opposite is true and that a balance between helicity and flexibility is needed for increased molecular piezoelectric response. Small changes in helical secondary structure between peptides **1-3** results in no statistical difference in measured piezo response; however, more rigid peptoids **4-6** show significantly lower response, on par with the

control **DDT** alkane thiol monolayer. Since any molecular monolayer will have intrinsic order and thus piezo response, we believe that combining systematic synthesis, PFM monolayer characterization, and computational design will unlock new avenues to highly responsive piezoactive materials.

### 3.0 Optimization of Nanoscale Electromechanical Coupling Evaluation Methods

This chapter has been adapted with permission from:

- Miller, N.C.; Grimm, H. M.; Horne, W. S.; Hutchison, G. R. Accurate Electromechanical Characterization of Soft Molecular Monolayers Using Piezo Force Microscopy. *Nanoscale Adv.* 2019, 1, 4834-4843

#### 3.1 Contributions

A collaborative effort with Haley M. Grimm whose individual contributions are as follows:

*Haley M. Grimm isolated the synthesis protocols for the development of tailored peptide and peptoid sequences.*

#### 3.2 Introduction

Since the discovery of piezoelectric activity in muscle tissue and other biological materials, the molecular origin of the electromechanical response has been a topic of interest. At the nanoscale, the electrical and mechanical properties of materials are often linked – for example giving rise to phenomena such as piezo-, flexo-, and ferroelectricity.<sup>1-5</sup> These phenomena, in turn, enable a wide range of applications from sensing to optoelectronics.<sup>3, 4, 6-15</sup> The piezoelectric effect (PE) comprises two effects: a direct effect, in which mechanical stress generates an electric charge.

Inversely, the converse PE generates a mechanical response to an applied electric field. Materials exhibiting piezoelectric response are generally non-centrosymmetric, polar, and poorly conductive. A range of materials exhibit piezoelectric properties including lead zirconate titanate (PZT), quartz, and various polymers such as polyvinylidene difluoride (PVDF). At the nanoscale the lack of centrosymmetry coupled with high polarities give rise to piezoelectric response, yielding a vast diversity of piezoelectric materials. For example, self-assembled monolayers, in which the attachment of target molecules to surfaces inherently breaks symmetry and generates a polar system, have been shown recently to be inherently piezoelectric.<sup>16</sup>

Accurate and reliable methods to measure piezoelectric outputs from a given material are vital to investigating these phenomena and realizing their potential range of applications. Atomic force microscopy (AFM) was initially developed to map the morphological variations in materials at the nanoscale.<sup>6,17</sup> Beyond simple topology and morphology, functional AFM methods have been developed to map properties including surface potential, charge transport, magnetic response, and piezoresponse.<sup>17-21</sup> The latter, piezo force microscopy (PFM), determines the mechanical response of materials to an applied electrical field by measuring the converse piezoelectric effect. However, classical single frequency PFM suffers from low sensitivity and poor frequency tracking due to crosstalk in the phase feedback loop between material topology and electromechanical response. To increase sensitivity and avoid dielectric breakdown of materials, dual AC resonance tracking (DART) was developed by Kalinin to allow the use of small bias voltages while maintaining good frequency tracking despite varying topological features.<sup>4, 6, 18, 20-24</sup> Building on the principles of PFM, DART drastically improved the sensitivity of PFM measurements and helped move the field towards more quantitative piezoelectric measurements. Beyond DART, the band excitation (BE) method was intended to overcome distortions associated with tip-sample interactions experienced

in DART, in which the lever is excited at multiple frequencies around the fundamental frequency to alleviate shifts in the fundamental, due to topography.<sup>25</sup> More recently, several groups have tried to reduce/eliminate these distortions by using high spring-constant ( $k_l$ ) levers, with or without a fixed external DC field, or by creating new lever technologies, such as “inner paddled levers”.<sup>2, 3, 26-28</sup> These techniques reduce the electrostatic component of the measurement for specific cases; however, this may not be true for systems, such as organic polymers and biomaterials, in which the electrostatic component is quite large or in which the Young’s modulus of the material is small in comparison to the lever.

The above methods, particularly the use of high spring-constant levers, perform best with materials in which the elastic modulus is significantly higher than that of the lever. Unfortunately, when the modulus of the material under study is small in comparison to modulus of the lever, such as organic and biomaterials, the lever may deform the target surface, reducing or eliminating the sensitivity enhancements garnered by DART or band excitation techniques.

In this work, we describe a method for improved accuracy in measurements of the piezo-response ( $d_{33}$ , the response of a material in the  $z$ -axis to a field applied in the same axis) of soft organic monolayers. The method entails the use of a soft (low- $k_l$ ) lever, coupled with the quantification of the electrostatic component of tip response by completing a DC field sweep in addition to the AC field sweep already employed to measure the independent lever electrostatics. By compensating for the electrostatic component, the true  $d_{33}$  of the material can be established.

## 3.3 Methods

### 3.3.1 Monolayer Formation

Solvents and reagents were purchased from Sigma-Aldrich without further purification. BioGold substrates were purchased from Thermo Scientific and consist of a glass substrate with a titanium (10 nm) adhesion layer and gold (100 nm). The peptide and peptoid were synthesized and purified following procedures described previously.<sup>16</sup> Gold-thiol based self-assembled monolayers were prepared from 1.0 mM solutions of dodecane thiol (DDT) or mercaptoundecanoic acid (MUA) in ethanol, a peptide in water, and peptoid in acetonitrile. The various solvents were used to ensure maximum solubility of target molecules and have no bearing on SAM formation. Substrates were prepared for SAM formation by multiple ethanol and water washings followed by a 15-minute sonication in the solvent used for deposition (ethanol for MUA/DDT, water for peptide and acetonitrile for peptoid). After the corresponding solvent wash, substrates were rinsed with solvent and dried with N<sub>2</sub>. SAMs were formed by placing clean/dry substrates into 1.0 mM thiol ligand solution for 24 hours in ambient conditions. After the deposition period, samples were removed from solution rinsed, dried with N<sub>2</sub>, covered and placed in a desiccator for a minimum of one hour before analysis. All samples were stored under vacuum conditions in a UV blocking container to prevent thiol oxidation.

### 3.3.2 Equipment

All atomic force microscopy (AFM), scanning Kelvin probe force microscopy (sKPFM), piezo force microscopy (PFM), and amplitude modulated force microscopy (AMFM) experiments were carried out on an Asylum Research model MFP-3D SPM. PFM experiments were conducted using dual-AC resonance tracking (DART-PFM) mode. Three sets of cantilevers consisting of six individual probes of varying spring constants were used: ASYELEC-01 R2 (R2), Asylum Research, are iridium-coated conductive silicon probes with a  $70.0 \pm 19.5$  kHz free air resonance frequency, and a  $\sim 280$  kHz contact resonance. The R2 has a free air spring constant of  $2.8 \pm 1.4$  N/m. HQ: NSC36/PT (NSC: A, B, and C), MikroMash, are platinum-coated conductive silicon probes with three independent levers per chip. The levers have a  $90 \pm 65$ ,  $130 \pm 98$ ,  $65 \pm 45$  kHz free air resonance frequency for levers A, B and C respectively, giving a  $\sim 340$ ,  $520$ , and  $260$  kHz contact resonance for each lever. The NSC levers have a free air spring constant of  $1.0 \pm 2$ ,  $2.0 \pm 4.5$ , and  $0.6 \pm 1.25$  N/m. TR400PB (TR: S and L), Asylum Research, are gold-coated conductive silicon nitride probes with a  $32.0 \pm 14.5$  and  $10.0 \pm 7$  kHz free air resonance frequency, but a  $\sim 120$  and  $40$  kHz contact resonance. The TR levers have a free air spring constant of  $0.09 \pm 0.12$  and  $0.02 \pm 0.02$  N/m respectively.

### **3.3.3 Dual AC Resonance Tracking Piezo Force Microscopy (DART-PFM)**

DART experiments were conducted at multiple tip-sample AC, and DC biases ranging from  $|0-4|$  V. Deflection was set to -0.30 V with a tune z-voltage of  $\sim 15$  V and a scan z-voltage of  $\sim -7.0$  V, to maximize signal and ensure stable contact between probe and sample during scanning, unless otherwise stated. Relative humidity was maintained below 30 % with a dry N<sub>2</sub> purge inside the AFM enclosure. Each sample was examined in a  $1.0 \mu\text{m} \times 1.0 \mu\text{m}$  area with a rate of 0.75 Hz at a 90° scan angle to minimize topological artifacts. The topography, piezo-response amplitude and phase images were recorded and q-corrected to account for tip-sample resonance amplification using the built-in simple harmonic oscillator (SHO) function.<sup>16, 24</sup> Histograms of the resulting q-corrected piezo-response amplitude were generated, and the mean value of the distribution was extracted and correlated with the appropriate applied DC and AC fields, as discussed below.

### **3.3.4 Scanning Kelvin Probe Force Microscopy (sKPFM)**

sKPFM measurements were conducted solely with the R2 levers to attain the contact potential difference ( $V_{\text{cpd}}$ ) of each target material. Deflection was set to  $\sim 0.0$  V via tuning, with a scan z-voltage of 100 V. Start and delta heights were set to 10 nm for all contact potential images (NAP scanning in Asylum software) with a trigger voltage of 800 mV. A static 1.0 V DC field was established for each measurement with no sample grounding due to the dielectric nature of the monolayers being examined. The implemented scan rate was 0.5 Hz at a 90° scan angle.

### 3.3.5 Amplitude Modulated Force Microscopy (AMFM)

AMFM measurements were conducted with R2 and TRS levers to represent the contact stiffness across the range of the cantilever  $k$  values represented. Mirroring conditions used in DART scans a deflection of  $-0.30$  V with tune/scan  $z$  voltages of  $\sim 15.0$  V and  $-7.00$  V respectively were used. The manufacture provided tip radius for TRs =  $42$  nm and  $25$  nm for R2 were used to model tip-sample interactions assuming spherical contact. Scan areas of  $10.0$   $\mu\text{m}$  x  $10.0$   $\mu\text{m}$  at a  $1.0$  Hz scan rate were used to maximize sampling area, despite resolution loss.

## 3.4 Results and Discussion

We recently measured the piezoresponse of fixed polar molecular self-assembled monolayers, anchored by gold-thiol interactions to gold-coated glass substrates.<sup>16</sup> These well-formed monolayers represent model systems for the investigation and development of soft, flexible, fixed polar organic piezoelectric materials.<sup>29</sup> In that work, piezoresponse was determined using DART-PFM by sweeping the applied AC electric field and plotting the corresponding measured response against it. The slope of the linear regression should yield the effective  $d_{33}$  ( $d_{\text{eff}}$ ), in recognition of the lack of direct measurement of the true fields experienced by the material and minor yet contributing electromechanical effects, of the material under study, as illustrated in **Figure 13A**. Unfortunately, the regression rarely passes through the origin due to electrostatic effects present when the tip is brought into contact with the surface; resulting in a sizeable inherent error in the measurement regardless of the care taken in the data acquisition.

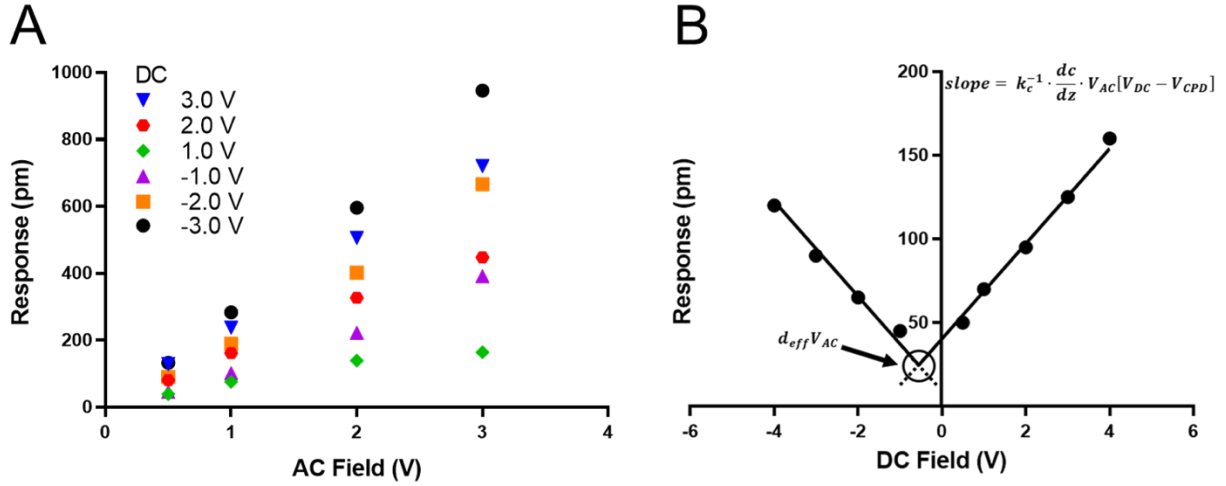


**Figure 13** (a) Traditional determination of piezoresponse using piezo-force microscopy by varied  $V_{AC}$  – the slope of the trend line should reflect the  $d_{eff}$  piezoresponse (pm/V). (b) Suggested  $V_{DC}$  sweep technique to determine the piezo response in soft-organic piezo in soft-organic piezo materials – the crossing point reflects the  $d_{eff}$  piezoresponse, and the slope reflects the electrostatic contribution of the material.

The tip response can be determined as in **Equation 3.1**<sup>17, 24</sup>

$$R = d_{eff}V_{AC} + k_c^{-1} \cdot \frac{\partial c}{\partial z} \cdot V_{AC}[V_{DC} - V_{CPD}] \quad \text{Eq. 3.1}$$

in which cantilever response  $R$  is equal to the  $d_{eff}$  (effective piezo coefficient) at the applied AC field ( $V_{AC}$ ) plus the contact stiffness ( $k_c$ ) augmented by the differential capacitance in the  $z$ -axis,  $V_{AC}$ , and the electrostatics at the surface composed of any applied or established DC field ( $V_{DC}$ ) and the contact potential voltage  $V_{CPD}$ .<sup>17, 24</sup> This equation relates the observed tip response to the piezoelectric response of the material combined with response due to tip-sample electrostatic interactions. Naturally, a conventional sweep of  $V_{AC}$  to determine the piezo response (e.g., **Figure 13A**), does not compensate for the electrostatic component – the second term of **Eq. 3.1**. Recent

efforts have attempted to minimize this electrostatic response using high  $k_l$  AFM levers to drive  $k_c$  towards zero. This effectively reduces the electrostatic component but does not eliminate it.<sup>27</sup> Unfortunately, while using stiff, high  $k_l$ , AFM levers lowers the electrostatic component with conventional ceramic-based piezoelectric materials, it is only effective in cases in which (1) the electrostatic component is small compared to the effective piezoresponse from the material and (2) the elastic modulus of the surface is much greater than the tip.

In the case of soft materials, such as organic and biomaterials, using stiff, high  $k_l$  levers will likely cause significant deformation of the target material. Since DART-PFM uses contact resonance for signal enhancement, the mismatch between the soft surface and stiff AFM lever leads to small tune amplitudes even under large applied fields and thus poor signal to noise. An apt analogy to this situation would be measuring the response of grass with a hammer – compressing the plant and limiting the observable response. Consequently, as proposed in the introduction, softer, low  $k_l$  levers should minimize surface deformation in soft organic and biomaterials; however, they bring additional complications in the form of significant electrostatic contributions to the observed  $d_{\text{eff}}$ . Unlike in traditional AC sweep methods here the electrostatic component is expected to be non-zero at zero applied field highlighting the effects of electrostatics on the measurement system. To account for this electrostatic effect, we envisioned sweeping the DC field to accurately determine the electrostatic component of the observed response, as well as the  $V_{\text{DC}}$  point at which the electrostatic response is minimized (**Figure 13B**). If successfully realized, we hypothesized this new technique would allow for increased quantitative accuracy in determining the  $d_{\text{eff}}$  piezo response even in soft materials.

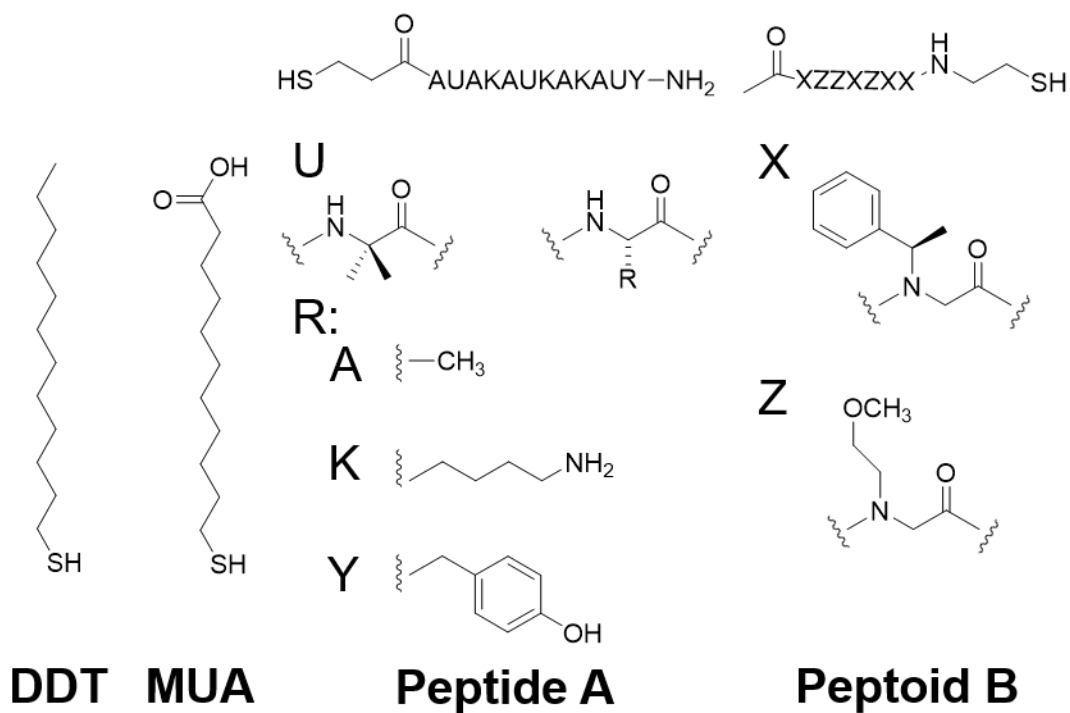


**Figure 14** Scheme of compounds under study.<sup>16</sup>

To test the proposed DC field sweeping DART-PFM technique, five different levers were chosen with spring constants ( $k_l$ ) varying from 0.02 to 2.8 N/m and used to determine the electromechanical response of four organic self-assembled Au-S monolayers (**Figure 14**). These organic SAM systems were chosen due to their innate polar alignment; thus, reducing or eliminating any electrostriction or flexoelectric response of the films in conjunction with being non ferroelectric. The SAMs tested included small molecule ligands (**DDT**, **MUA**) as well as bio-inspired peptide and peptoid oligomers (**A** and **B**) examined in our prior work.<sup>16</sup> The response of each target film was measured at varying piezo stack voltages, generating varying effective  $k_l$  values. **Figure 14** illustrates the resulting experiment, in which the recorded response for a given target material increases exponentially as the effective  $k_l$  value of the lever used in the measurement decreases. The results confirm that for soft materials like SAMs, using levers with spring constants comparable to the modulus of the material's leads to increased response. In some

cases, experimental tip responses reach 250 pm/V, far exceeding previously reported electromechanical response in these soft materials. Though the overall electromechanical response is high, as discussed below, these responses are influenced more by electrostatics than the intrinsic piezo response of the materials ( $d_{33}$ ). While the spring constant of the lever ( $k_1$ ) is shown to influence the response of the films, it is merely contributing to changes in the contact stiffness ( $k_c$ ).<sup>17, 20, 24</sup>

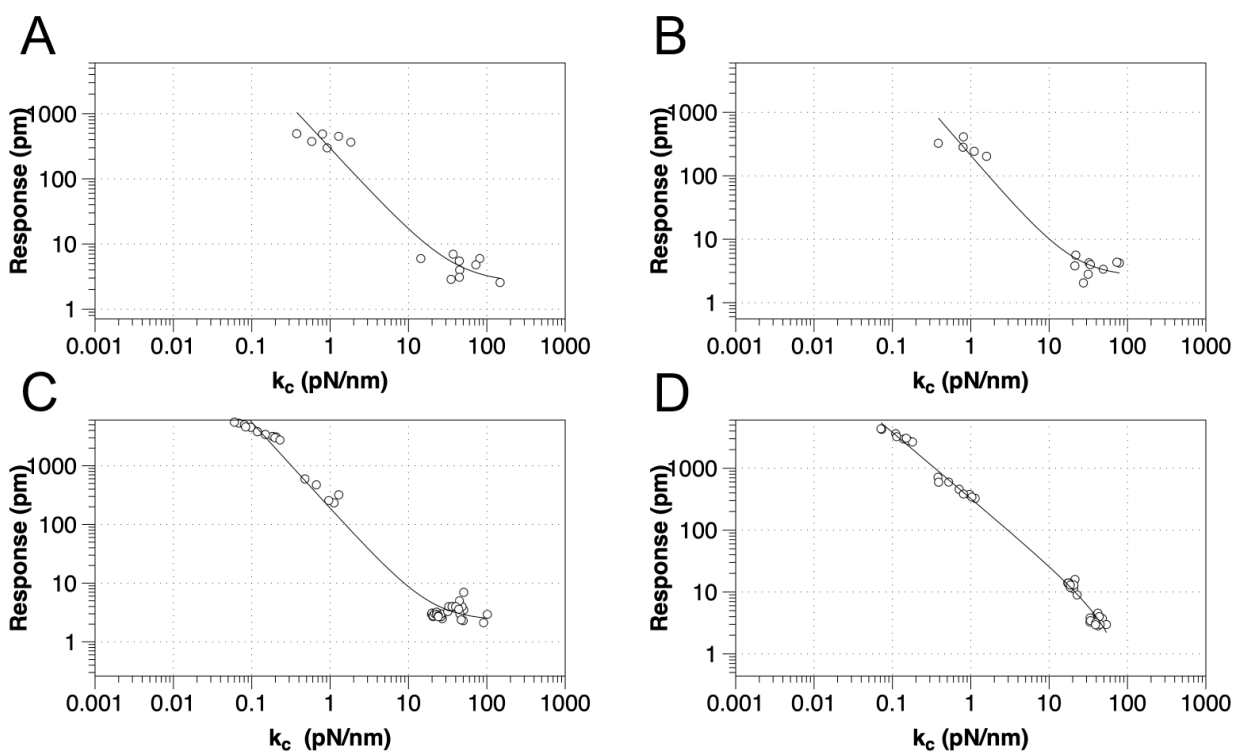


**Figure 15** Relationship between tip response ( $k_1$  and  $k_c$  as calculated using **Equation 3.2**) for various SAMs using AFM levers with spring constant from 0.02-2.8 N/m, for (a) DDT, (b) MUA, (c) peptide A and (d) peptoid B respectively. The best-fit line is to  $y = a + bx^c$ .

**Table 2** Summary of contact-dependent ( $k_c$ ) response across four organic self-assembled monolayers, indicating best-fit parameters from the fits in Figure 15.

Material	Constant (a)	Coefficient (b)	Power (c)	$R^2$
DDT	2.53	293	-1.30	0.948
MUA	2.56	206	-1.44	0.959
Peptide A	2.32	187	-1.47	0.985
Peptoid B	-2.42	327	-1.07	0.993

As **Equation 3.1** illustrates, while stiffer levers affect the response, it is the contact stiffness ( $k_c$ ) that directly influences the measurement.<sup>24</sup> While the distinction may seem subtle,  $k_l$  is merely a single component of the contact. Thus, the spring constant of the contact derives from the lever, the mechanical response of the material in the x, y, and z-axis, influence of surface electrostatics, and any tip-sample meniscus that may be present (e.g., in ambient conditions). Fortunately, these factors can be estimated by applying **Equation 3.2** to the already measured  $k_l$  values (as part of tip-sample tuning in DART-PFM).<sup>17</sup>

$$k_c = k_l \left[ \left( \frac{w_1}{w_0} \right)^2 - 1 \right] \quad \text{Eq. 3.2}$$

**Equation 2** approximates the spring constant of contact ( $k_c$ ) from the spring constant of the lever ( $k_l$ ) by taking the ratio of the resonance frequency of the free lever ( $\omega_0$ ) to the lever in contact with the sample ( $\omega_1$ ) used in the DART experiment.<sup>17</sup>

While the use of stiffer levers is correlated to an increased contact stiffness, using the calculated  $k_c$  values to model tip response, yield better fits (**Table 2**), reflecting the correct physics due to the higher spring constant of the contact stiffness dominating. The comparable fits of tip

response to  $k_1$  values, found in **Table S1**, qualitatively maintain the same trend – decreased spring constant yields increased electromechanical tip response, albeit with lower quality of fit ( $R^2$ ).

However, as indicated in **Equation 3.1**, an ideal dependence would yield an exponent of  $k_c^{-1}$  (example plot in SI), but the values determined by fits in **Figure 14** and **Table 2** deviate significantly. In all the organic monolayers, the tip response falls off faster than predicted (i.e., exponents closer to ca. -1.3) with increasing contact stiffness. We speculate that this derives from the stiffer levers distorting the monolayers instead of remaining at the interface. The only exception is for the peptoid **B** SAMs, in which the tip-response curve yields an exponent close to -1.0, suggesting that the peptoid film is significantly stiffer than the other films, as confirmed by AMFM measurements discussed below, and consistent with expectations of a peptoid PPI helix.<sup>27</sup>

While **Equation 3.2** allows an approximate conversion of  $k_1$  to  $k_c$  values, assuming a uniform shift from the fundamental frequency of the lever to the measured frequency of the lever while interacting with surface,  $k_c$  was also measured directly using amplitude modulated force microscopy (AMFM).<sup>10, 30-32</sup> Due to the trends observed in the original  $k_1$  measurements, the  $k_c$  was not directly measured by AMFM for all levers. Only the ASYELEC.01 R2 and the TR400PB (S) levers, 2.8 and 0.09 N/m respectively, were chosen as the relative extremes of contact stiffnesses observed in the initial study, (Table in SI). We note that the measured  $k_c$  values deviate substantially from **Equation 3.2** for stiffer levers, again suggesting that the stiffer levers are distorting the monolayers, effectively limiting the ability of the soft materials to mechanically respond to the applied electric fields.

As mentioned above, while soft levers give higher tip response, they also suffer from greater levels of electrostatic interference than stiffer levers. One way to account for this effect would be to apply a  $V_{DC}$  to the tip that is equal to  $V_{CPD}$ , thus eliminating the electrostatic term in

**Equation 3.1.** Intuitively one simple solution would be to measure the  $V_{CPD}$  by sKPFM, and then apply that  $V_{DC}$ , as has been previously implemented.<sup>27</sup> The problem arises from the nature of the DART measurement in which a  $V_{AC}$  is applied on top of the  $V_{DC}$ , altering the electrostatic environment around the contact, modulating the intrinsic  $V_{CPD}$  of the sample. Instead, we swept the DC field to find the point of minimal tip response at which the contact potential equals the applied DC field under a constant  $V_{AC}$  (**Figure 13B**).

The tip response ( $R$ ) is the measured output of the DART experiment after the simple harmonic oscillator (SHO) calculation corrects for the tip-sample resonance enhancement. This tip response can be separated, using **Equation 3.1**, into the intrinsic piezoresponse of the material and the electrostatic response. When  $V_{DC}$  is equal to  $V_{CPD}$ , the electrostatic component of the measurement will go to zero leaving only the mechanical response of the material under the applied field. The organic SAM films are intrinsically polar, permanent piezoelectric materials, since one end is attached via an Au-S bond. Consequently, one expects no ferroelectric hysteresis from sweeping  $V_{DC}$ , only two intersecting lines of equal slope proportional to  $kc^{-1} dC/dz$  (**Figure 13B**). The intersection point will represent the piezoelectric response  $d_{eff} \cdot V_{AC}$ . The results are highlighted in **Figure 15** and summarized in **Table 3**, in which three different AFM levers are used on two different organic SAMs.

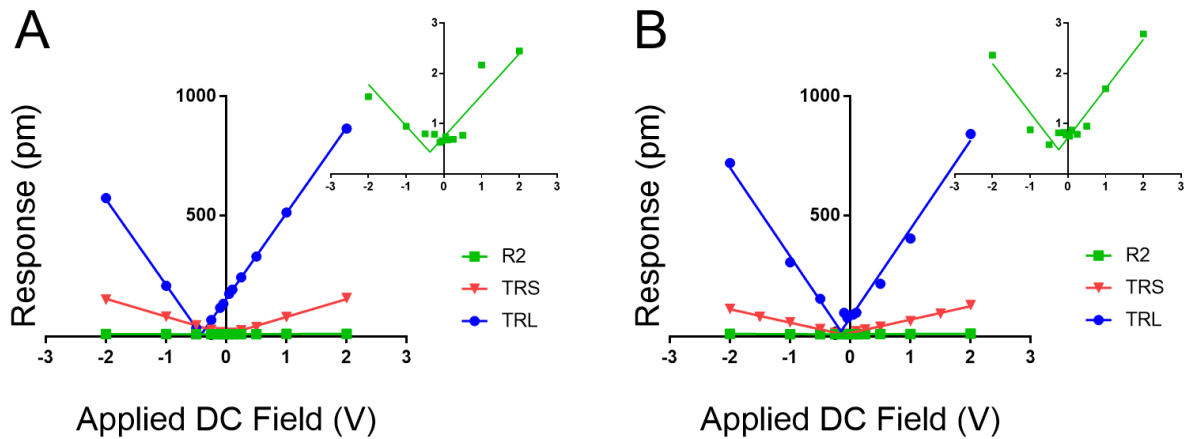


**Figure 16** Influence of cantilever contact stiffness on measured film response as a function of DC field. Inset plots highlight the noise floor of the tip response ( $\sim 1$  pm) when the  $k_l$  is far greater than the modulus of the material. (a) Response of the **DDT** to varied DC field with three levers Asyelec.01 R2 (R2, 2.8 N/m), TR400PBS (TRS, 0.09 N/m), and TR400PBL (TRL, 0.02 N/m). (b) Response of peptide **A** to varied DC field with three levers Asyelec.01 R2 (R2), TR400PBS (TRS), and TR400PBL (TRL).

**Table 3** Coefficient values and calculated  $d_{\text{eff}}$  from tip response as a function of applied DC voltage at constant  $V_{\text{AC}}$  of 4.0 V.

Material	$k_l$ (N/m)	$V_{\text{CPD}}$ (V)	Slope (A)	$R^2$	$d_{\text{eff}}$ (pm/V)
<b>DDT</b>	2.8	-0.369	0.827	0.818	0.12
<b>DDT</b>	0.09	0.001	75.1	0.998	-0.28
<b>DDT</b>	0.02	-0.419	360	0.999	-0.32
<b>Peptide A</b>	2.8	-0.245	0.979	0.921	0.12
<b>Peptide A</b>	0.09	-0.111	56.3	0.995	-0.16
<b>Peptide A</b>	0.02	-0.153	373	0.987	3.2

**Figure 15** establishes that the proposed new method works for fixed polar molecular monolayer films. The technique is demonstrated on two SAMs: one piezo activepeptide<sup>16</sup> and a control of DDT, used to highlight the natural polarization of organic SAMs when adsorbed to a metallic surface. The high electrostatic component of the low  $k_l$  levers is easily compensated through the new method. The results point to a piezoresponse range of -0.33 to 0.11 pm/V for DDT and -0.16 to 3.2 pm/V for peptide **A**. The measured  $d_{\text{eff}}$  of peptide **A** using the 0.02 N/m lever is significantly larger than the values determined with the stiffer levers.

Further, by highlighting three different spring constant levers ranging from 0.02 to 2.8 N/m the results from **Figure 14** can be reaffirmed. Here, film response increases with decreasing  $k_l$  due to electrostatic effects, reducing the maximal response at 2.0 V<sub>DC</sub> and 4.0 V<sub>AC</sub> from near 1000 pm to ~3 pm. These results represent a greater than 300-fold decrease in measured response; moreover the inset charts in **Figure 15** demonstrate that at high  $k_c$ , relative to the sample material, the instrument sensitivity bottoms out, effectively identifying the noise floor of the measurement technique. The inset charts emphasize the trend towards higher  $R^2$  values in which at high  $k_c$  and  $k_l$ , response is sporadic and hard to model in contrast to the low  $k_l$  levers. The increase in sensitivity is further confirmed by the changes in the tune amplitude, at the described set points, from <2 V to >50 V. These, results reflect the benefits of the new method by demonstrating increased precision in the determination of the  $d_{\text{eff}}$  for soft monolayers through enhanced signal to noise ratios.

Based on the evidence in **Figures 14-15**, the use of soft, low-spring-constant the TRS levers (0.09 N/m) are less likely to perturb organic monolayers, and the DC-sweep DART-PFM technique enables separation of inherent piezoelectric response of a material from the electrostatic components to tip response. Consequently, TRS levers were used with DC-sweep DART-PFM

across four organic SAMs and a quartz crystal microbalance (QCM). The latter serves as a non-ferroelectric control with known piezoresponse ( $d_{33}$ ), while DDT and MUA SAMs were used as control organic monolayers with low expected piezoresponse, but varying hydrophobicity. If the contact stiffness depends on the effects of a meniscus at the tip sample interface under ambient conditions, modulating from a hydrophobic DDT monolayer to a hydrophilic MUA monolayer should reveal such effects on measured electromechanical response. Peptide **A** and peptoid **B** represent helical piezoactive materials with different backbone motifs that give rise to differences in helical propensity.<sup>16</sup>

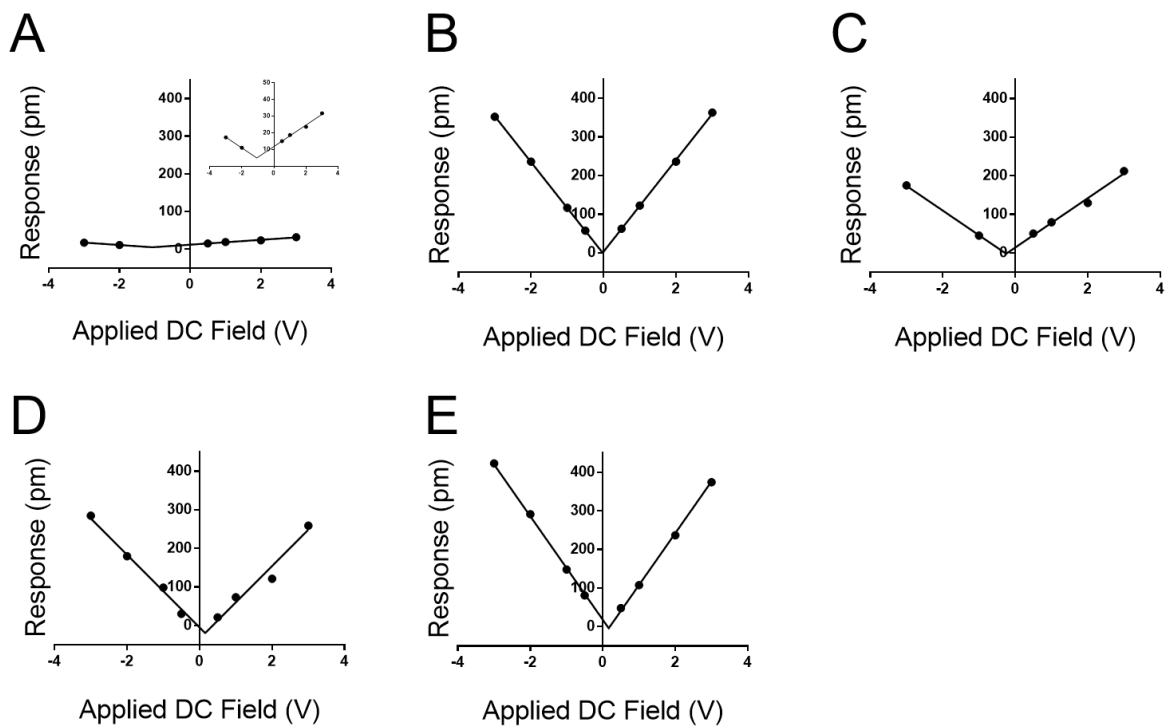


**Figure 17** PFM tip response from sweeping the DC field of several materials using TRS levers, and an applied AC field of 3.0 V. Response of (a) quartz crystal microbalance surface; inset provides rescaled y-axis, (b) DDT, (c) MUA, (d) Peptide **A**, and (e) Peptoid **B**. Note that all four organic monolayers show profoundly greater DC-field (electrostatic) response than the QCM surface as reflected in the slope of the DC-dependent response.

**Table 4** Coefficient values and calculated  $d_{\text{eff}}$  from tip response as a function of applied DC voltage at constant  $V_{\text{AC}}$  of 3.0 V using 0.09 N/m  $k_l$  levers.

<b>Material</b>	<b><math>V_{\text{CPD}}</math> (V)</b>	<b>Slope (A)</b>	<b><math>R^2</math></b>	<b><math>d_{\text{eff}}</math> (pm/V)</b>
<b>QCM</b>	-1.06	6.40	0.993	1.68
<b>DDT</b>	-0.022	119	0.999	0.100
<b>MUA</b>	-0.249	63.9	0.991	-0.560
<b>Peptide A</b>	0.157	94.1	0.975	-6.42
<b>Peptoid B</b>	0.165	134	0.999	-1.35

The DC-sweep DART-PFM response of these films under a constant 3.0  $V_{\text{AC}}$  field is illustrated in **Figure 17** and compiled in **Table 5**. The resulting field plots yield  $d_{\text{eff}}$  of the varying materials. QCM stands out with a  $d_{\text{eff}}$  value consistent with literature (i.e. 1.68 pm/V vs 2.3 pm/V),<sup>19</sup> but the observed tip response is small compared to the other monolayer samples. The low slope indicates that the magnitude of the  $d_{\text{eff}}$  in quartz is not significantly different from that of the monolayers, but its electrostatic component is minimal compare to the monolayer films. This likely indicates that the ability of quartz to build a large differential capacitance in the z-axis is compromised in comparison to the SAMs. Further, these results reconfirm previously reported conclusions that the helix forming peptide and peptoid have higher piezo electric coefficients than DDT and MUA.<sup>16</sup>

More significant than the magnitude of the tabulated piezo coefficients in **Table 5** is the sign. Noticeably three out of four SAMs have a negative  $d_{\text{eff}}$ , indicating that they compress under an applied field. Only DDT produced a positive  $d_{\text{eff}}$ , albeit close to zero. This negative piezo response differs from conventional piezo ceramics such as ZnO or PZT, but is similar to that observed in PVDF and a variety of piezoelectric materials.<sup>33-35</sup> Thus, the new method not only determines positive, but also negative piezoresponse, even at low applied voltages.

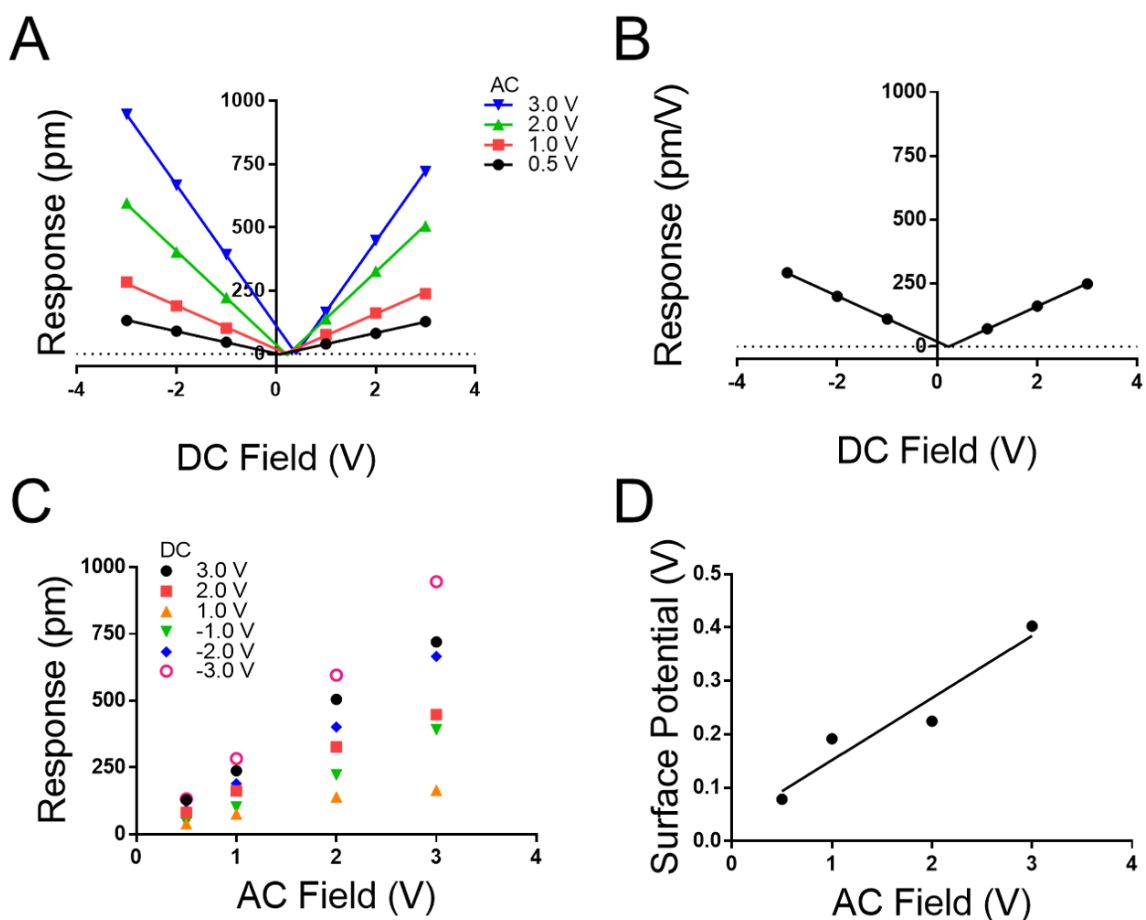


**Figure 18** (A) Effect of applied DC field on peptoid **B** film response at various AC fields using 0.09 N/m levers. (B) DC-dependent response. (C) PFM response as a function of  $V_{\text{AC}}$  with specified constant DC fields. (d) Measured surface potential as a function of applied  $V_{\text{AC}}$ .

We note both the  $d_{\text{eff}}$  and  $V_{\text{CPD}}$  from the peptide **A** monolayer shifts by applying different  $V_{\text{AC}}$  between **Figure 15** and **Figure 16** ( $4.0 V_{\text{AC}}$  and  $3.0 V_{\text{AC}}$  respectively). To test if the  $V_{\text{CPD}}$  and  $d_{\text{eff}}$  is subject to shifting under various experimental conditions a film of peptoid **B** was tested against four different AC voltages sweeping through six DC voltages at each AC voltage. Extracting the surface potential under experimental conditions from **Figure 18A** and comparing it to the applied AC field a linear trend emerges. As the applied electric field increases under the experimental conditions so does the  $V_{\text{CPD}}$ . This indicates that a static  $V_{\text{DC}}$  determined by sKPFM cannot be used directly to eliminate the electrostatic component of the measured response, as has been previously suggested.<sup>27</sup> Further Figure 5A represents the equivalent of eight experimental runs on one sample using the more traditional AC sweep method, thus confirming the repeatability of the new measurement system and the lack of dielectric brake down of the films due to the applied fields.

**Figure 18A** highlights that the maximal response of the film increases with increasing  $V_{\text{AC}}$  as suggested in conventional piezoelectric materials and measurement techniques. To confirm this, a map was extracted from **Figure 18A** to generate **18C** in which the response of the film is plotted against the applied  $V_{\text{AC}}$  at each DC voltage, recreating the conventional approach to the determination of  $d_{\text{eff}}$  by DART-PFM. This exercise emphasizes the ability of the new DC sweep method to remove the effects of electrostatic response and thereby reduce the variation in the measured  $d_{\text{eff}}$ . The new method gives the  $d_{\text{eff}}$  of peptoid **B** to be  $-0.24 \pm 1.36 \text{ pm/V}$  in comparison to the traditional method with the electrostatics unaccounted for at  $188.50 \pm 39.25 \text{ pm/V}$ . To supplement these conclusions the points at each  $V_{\text{DC}}$  in **Figure 18A** were averaged with  $V_{\text{AC}}$  removed to generate **Figure 18B**. In **Figure 18B** the variation at each point is so insignificant that the error does not show on the plot. As expected, the calculated  $d_{\text{eff}}$  from **Figure 18B** agrees with

**Figure 18A** at -0.223 pm/V. Though, these figures are not identical to the  $d_{\text{eff}}$  values determined in **Figure 17**, they are within error of each other.

**Table 5** Coefficient values and calculated  $d_{\text{eff}}$  from tip response as a function of applied DC voltage on peptoid **B** at constant  $k_1$  of 0.09 N/m.

$V_{\text{AC}}$ (V)	$V_{\text{CPD}}$ (V)	Slope (A)	$R^2$	$d_{\text{eff}}$ (pm/V)
3.0	0.403	277.6	0.999	0.360
2.0	0.225	184.9	0.999	-2.18
1.0	0.192	85.99	0.996	3.37
0.5	0.079	43.86	0.999	-2.51
NA	0.227	89.67	0.999	-0.223

The comparison between the molecular monolayers and quartz highlights a significant shift of material response to an applied field. The slopes of the plots in **Figure 15** represent the electrostatic component of the material response. When comparing the materials there is a significant shift in the slope of the fits indicating a variation in the effect of electrostatics on the reported response. Quartz has a fundamentally shallower slope than any of the molecular films. Likely the applied AC field or the differential capacitance in the z-axis are the influencing factors. The AC field however is uniformly applied at 3.0 V across all samples and accounted for when the final response is computed. In addition, a humidity-controlled chamber held at approximately 20 % provides no likely outside source for field augmentation, ensuring little to no variation in the meniscus formed at the tip-sample interface. Hence, the contribution from the differential capacitance in the z-axis is likely the source of the discrepancy in the overall measured response.

This difference in capacitance is likely due to a difference between the relatively high dielectric constant of quartz ( $\epsilon \sim 4$ ) compared to the lower dielectric constant of the SAMs (MUA  $\sim 2$ ).<sup>36, 37</sup>

To test this hypothesis, several conventional hard-ceramic piezoelectric materials were tested, in addition to the non-ferroelectric quartz material sampled above, including: ferroelectric PZT ( $\sim 1$  cm thick), PPLN ( $\sim 1$  mm thick), and a second non-ferroelectric material ZnO ( $\sim 1$  mm thick), and (results in SI). Only ZnO gave responses signaling significant influence of electrostatics on the reported response (see SI). The testing of PZT and PPLN mirrored the results of quartz, in which the slopes of the fits are shallow, but present higher baseline piezo response. These results confirm that soft-molecule based piezoelectric materials are fundamentally different from classical ceramic based materials and must be analyzed with new methods that allow for operation at higher signal to noise ratios while simultaneously removing the electrostatic component of the response. This has been demonstrated to be achievable by alternatively sweeping the  $V_{DC}$  instead of the  $V_{AC}$  and finding the point of inflection in which the  $V_{DC}$  is equal to the  $V_{CPD}$  and extracting the  $d_{eff}$  from that point instead of the slope of the fit.

### 3.5 Conclusions

This work has coupled multiple AFM techniques together to establish and validate a new method for quantitatively separating the electrostatic component from the purely piezoelectric response of low Young's modulus piezo-active materials using DART-PFM. We find that organic monolayers, and other soft electromechanical materials, require the use of low spring constant tips to better match the elastic modulus of the materials. In turn, this increases the electrostatic component of the tip response, which can be minimized by sweeping the DC voltage until the minimum response is found. In principle, this point should reflect the contact potential of the film. We find through scanning Kelvin probe microscopy that the potentials are close, but effects of applied fields during the DART-PFM experiment modulate the  $V_{DC}$  potential that minimizes the electrostatic tip response. Elastic AMFM results established the necessity to match lever stiffness ( $k_l$ ) with the modulus of the material under study. Simultaneously, AMFM results confirmed that the contact stiffness ( $k_c$ ) is directly influenced by the  $k_l$ , yet  $k_c$  is the optimal parameter for the accurate determination of the piezoelectric coefficient, unlike previous reports.<sup>27</sup>

We find incredibly large electromechanical tip responses, nearing 250 pm/V, which derive from large differential capacitance of the films rather than the innate piezoresponse. This large electrostatic component from organic monolayers is in stark contrast to a range of inorganic materials studied, which may show greater intrinsic piezoresponse, but much lower electrostatic components. We speculate that while the organic monolayers have lower dielectric constants than piezo ceramics such as PZT, the differential capacitance is high due to their lower elastic modulus and thin layer thickness (e.g., ~2 nm).

The new method of DC-sweep DART-PFM was used to determine the  $d_{\text{eff}}$  piezoresponse and electrostatic components of four organic monolayers and four conventional inorganic piezo materials. The method finds peptide and peptoid SAMs with both positive and negative piezo response and, coefficients in agreement with previously reported values.<sup>16</sup> Control molecular SAMs composed of DDT and MUA show close to zero piezoresponse. While scans across multiple films and different AC voltages do affect the measurement somewhat, the DC-sweep DART-PFM technique shows much improved reproducibility relative to previous efforts using varied AC voltages with DART-PFM.

We believe this new technique will improve accurate measurements of electromechanical response in organic and biomaterials. Moreover, the large electrostatic component of electromechanical response found in organic materials can likely be utilized for sensing or other applications.

## 4.0 Exploration of Organic-Molecular Based Ferroelectric Materials

### 4.1 Contributions

A collaborative effort with Allison Rice of the Shustova group at the University of South Carolina and Keith Werling whose individual contributions are as follows: *Allison Rice isolated the synthesis protocols for the development of 4,4',4'',4'''-(dibenzo[ghi,mno]fluoranthene-1,2,5,6-tetrayl)tetrabenzic acid and provided materials for testing and Keith Werling provided the computational predictions for the target materials.*

### 4.2 Introduction

Organic molecular materials possess highly tailorable properties at the nanoscale. These tunable properties include, but are not limited to, the net polarization, capacitance, breakdown voltage, and piezoresponse of the resulting material.<sup>1-6</sup> Within these properties lies a subset of materials that exhibit spontaneous electric polarization of the molecular dipoles upon the application of an external electric field.<sup>1,4</sup> These ferroelectric materials are related to piezoelectric materials, examined previously, with the additional property that their net polarization can be manipulated by the application of an external field.

The degree of polarization manipulation is dependent on the magnitude and direction (positive/negative) of the applied field. The resulting remnant polarization hysteresis allows for unique applications of ferroelectric materials such as non-volatile memory, sensing, tunnel

junctions, and even some catalysis.<sup>1, 6-8</sup> In classical ceramic materials, this phenomenon manifests in a displacement of ions within the unit cell. For organic materials such as polymers and solids, the applied field can either induce a reorientation of the polymer, often liquid crystals, with the applied field or a dynamic proton transfer within an organic solid.<sup>1, 2, 9-11</sup> In our previous work with molecular piezoelectric materials, field-induced conformational changes, the molecular dipole moment remained fixed in direction, determined by the direction of the molecular attachment to the surface of the substrate.

Quan *et al.* computationally predicted that organic molecules based on corannulene, sumanene, pyrene, and perylene structures could produce both piezoelectric and ferroelectric response in the presence of an applied electric field.<sup>11</sup> Furthermore, the degree of response and the required coercive field for the inflection of the directional polarization can be influenced by the type and placement of substituents on the core molecule. These substituents influence the bowl depth of these "buckybowl" structures, thus modulating the energy required for inversion. The ability to control the inversion energy enabled the discovery of new derivatives of corannulene with inversion energies below the dielectric break down voltage. The decrease in the inversion energy barrier, through the destabilization of the ground state energy, was achieved through electron-withdrawing substituents inducing a significant dipole moment coupled with a reduction in the molecular-bowl depth.<sup>1, 11-15</sup>

## 4.3 Methods

### 4.3.1 Sample Preparation

Solvents and reagents were purchased from Sigma-Aldrich without further purification. BioGold and indium tin oxide (ITO) substrates were purchased from Thermo Scientific and consist of a glass substrate with a 100 nm ITO layer or a titanium (10 nm) adhesion layer and gold (100 nm). 4,4',4'',4'''-(dibenzo[*ghi,mno*]fluoranthene-1,2,5,6-tetrayl)tetrabenzonic acid (**H4DFT**) was synthesized by a previously outlined method.<sup>7</sup> One hundred percent pure ethanol was used to ensure maximum solubility of target molecules and have no bearing on SAM film formation. Substrates were prepared for drop casting by multiple ethanol and water washings followed by a 45-minute sonication in the solvent used for deposition. After the corresponding solvent wash, substrates were rinsed with solvent and dried with N<sub>2</sub>. The films were formed by taking the clean/dry substrates and drop-casting an optimized concentration of the target molecule on the surface. Samples were then covered and placed in a desiccator under vacuum for a minimum of one hour before analysis. All samples were stored under vacuum conditions in a UV blocking container to prevent film degradation.

### 4.3.2 Dual AC Resonance Tracking Piezo Force Microscopy (DART-PFM)

DART-PFM measurements were conducted on an Asylum Research MFP3D AFM with BL-TR400PB levers, purchased from Asylum Research. Experiments were conducted at multiple tip-sample AC, and DC biases ranging from  $\pm 0-4$  V. The cantilever deflection was set to  $-0.30$  V with a tune z-voltage of  $\sim 15$  V and a scan z-voltage of  $\sim -7.0$  V, to maximize signal and ensure

stable contact between probe and sample during scanning, unless otherwise stated. Relative humidity was maintained below 25 % with a combination of a dry N<sub>2</sub> purge and desiccant inside the AFM enclosure. Each sample was examined in 1.0 μm x 1.0 μm areas with a rate of 0.75 Hz at a 90° scan angle to minimize topological artifacts. The topography, piezo-response amplitude, and phase images were recorded and q-corrected to account for tip-sample resonance amplification using the built-in simple harmonic oscillator (SHO) function within the Asylum Research software, version 14.<sup>16</sup> Histograms of the resulting q-corrected piezo-response amplitude were generated, and the mean value of the distribution was extracted and correlated with the appropriate applied DC and AC fields. The correlated points are then plotted against the applied DC field to find the point in which the applied DC is equal to the surface potential of the sample under experimental conditions. This point is then used to find the effective piezo coefficient,  $d_{\text{eff}}$ , of the sample with the electrostatic component of the measured response removed.<sup>17</sup>

### **4.3.3 Scanning Kelvin Probe Force Microscopy (sKPFM)**

SKPFM measurements were conducted with Asyelec.01 R2 levers, purchased from Asylum Research, to attain the contact potential difference ( $V_{\text{cpd}}$ ) of each target material on an Asylum Research MFP3D. Relative humidity was maintained below 25 % with a combination of a dry N<sub>2</sub> purge and desiccant inside the AFM enclosure. The deflection was set to ~0.0 V via tuning, with a scan z-voltage of 100 V. Start and delta heights were set to 20 nm for all contact potential images (NAP scanning in Asylum software) with a trigger voltage of 600-800 mV depending on the tune of the lever. A static 1.0 V DC field was established for each measurement with sample grounding due to the large applied fields before measurement. The implemented scan rate was 0.8 Hz at a 90° scan angle with a 500 x 500 nm scan area. Prior to the measurement of the

surface potential, the sample was exposed to a DC field applied via the substrate using the MFP3D scan head.

#### 4.4 Results and Discussion

Quan *et al.* used computational methods to predict the ferroelectric properties of corannulene and its substituted derivatives.<sup>11</sup> Corannulene is a bowl-shaped molecule that can be tailored with electron-withdrawing substituents to manipulate the molecular-bowl depth and, thus, the energy of the inversion barrier, when anchored to a substrate. A lower inversion barrier accesses a pathway for a bowl to bowl inversion of a corannulene derivative below the dielectric breakdown voltage of the material.<sup>11, 13, 18</sup> If a bowl to bowl inversion becomes possible below the dielectric break down voltage, it is likely the molecular film will then have a conformational memory to an applied electric field. This "conformational memory" is known as ferroelectric character, **Figure 20C**, where the molecular film undergoes a conformational change in relation to the magnitude and direction of the applied field. If this conformational change is retained over time the material can be considered ferroelectric. This "conformational memory" for corannulene is illustrated in **Figure 19B**, where the molecule displays three separate states of bowl up or down and a flat transition state between the two.<sup>11</sup>

Here in a model corannulene derivative, 4,4',4'',4'''-(dibenzo[*ghi,mno*]fluoranthene-1,2,5,6-tetrayl)tetrabenzoic acid referred to as **H<sub>4</sub>DFT**, **Figure 19A**, is used to assess the ferroelectric nature of these bowl-shaped molecules as a well-formed monolayer under ambient conditions.<sup>7, 11</sup> The benzoic acid substituted derivative of corannulene was chosen as the electron-

withdrawing groups give a large overall dipole moment, as well as an attachment point for oxide surfaces.<sup>2, 12, 14, 19-23</sup>

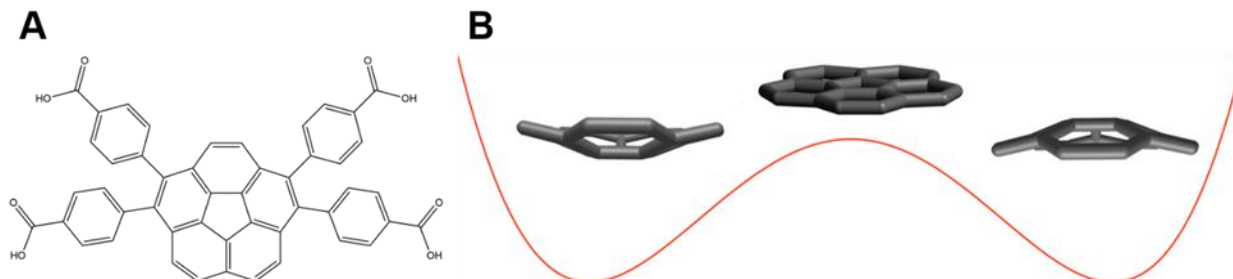


**Figure 19** Schematic of 4,4',4'',4'''-(dibenzo[*ghi,mno*]fluoranthene-1,2,5,6-tetrayl)tetrabenzoic acid “H<sub>4</sub>DFT” (A). Schematic of the bowl to bowl inversion of a model corannulene molecule (B).

**Figure 20** highlights the difference in film response to an applied field when the material is (a) dielectric, (b) paraelectric, or (c) ferroelectric. Here a dielectric material would display a linear change in polarization to an applied field with no net change in polarity over time. Similarly, a paraelectric material presents no net polarization shift with time but instead has a nonlinear shift in polarization to an applied field. In contrast, a ferroelectric material not only displays a nonlinear change in polarization to an external field but a remnant polarization to that field, i.e., there is a “memory” to the change in polarization in the material to an applied electric field.<sup>1, 24</sup>

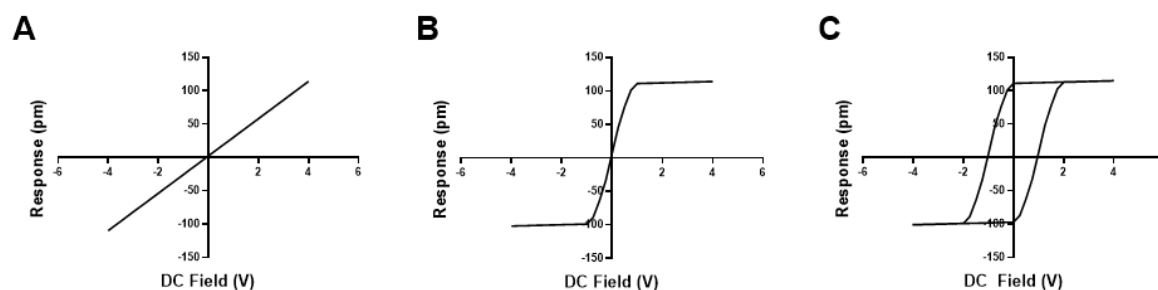


**Figure 20** Schematic of example electromechanically coupled responses from (A) dielectric materials, (B) paraelectric materials, and (C) ferroelectric materials.<sup>1, 15</sup>

As stated previously, most ferroelectric materials demonstrate piezoelectric coupling in addition to the ferroelectric character at the nanoscale. To investigate the piezoelectric response, **H4DFT** was deposited onto an indium tin oxide (ITO) surface in which the terminal acid groups should serve as anchoring points to the substrate in addition to an Au surface where there should only be absorption to the surface.<sup>20, 21, 23, 25-27</sup> **Figure 21** illustrates decreasing aggregate formation and surface roughness with decreasing **H4DFT** solution concentration. Ideal monolayer formation requires low surface coverage with little to no aggregate formation after sample washing.<sup>25, 28, 29</sup> **Figure 21** indicates that the threshold solution concentration for these conditions occurs at a solution concentration of 0.125mM. Here, the appearance of aggregates on the Au surface is sufficiently suppressed, ensuring all measured responses are derived from a near single monolayer, not an unknown aggregate.

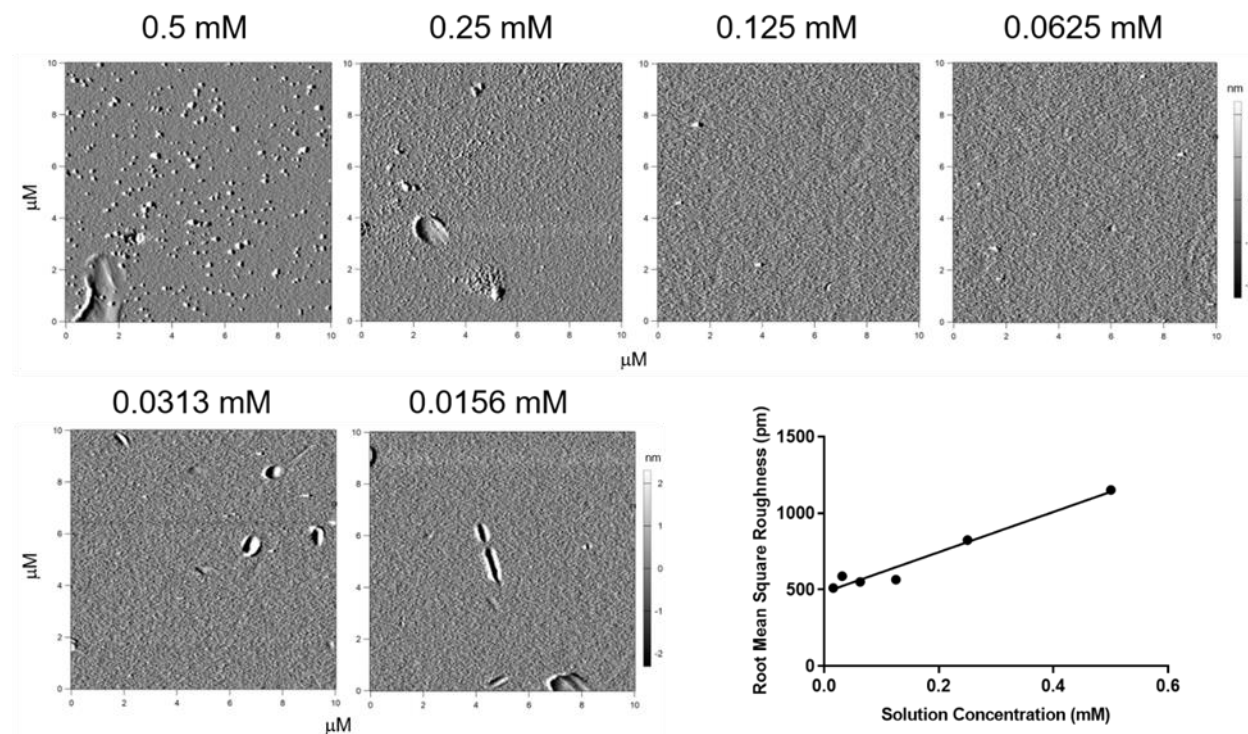


**Figure 21** AFM amplitude topography of the resulting films from the exposure to decreasing **H4DFT** solution concentrations on a clean Au surface. The plot represents the correlation of

decreasing root mean square (RMS) roughness of the Au/ **H4DFT** surface with decreasing solution concentration.

The organic molecular nature of the **H4DFT** film should yield a soft, flexible material requiring the implementation of the recently developed and above described DC sweep dual AC resonance tracking piezo force microscopy (DC-Sweep DART-PFM).<sup>17</sup> By sweeping the DC field, the electrostatic response of the film can be separated from the piezoresponse ( $d_{\text{eff}}$ ) under ambient conditions. Here the electromechanical response was measured under three different AC fields from 2.0 up to 3.0 V<sub>AC</sub>. The responses were then corrected for the V<sub>AC</sub> and averaged, the resulting  $d_{\text{eff}}$  of **H4DFT** was recorded to be 26.49 pm/V on ITO, **Figure 23B**. In contrast, when **H4DFT** is solution deposited on an Au surface, where the acid termini do not provide sufficient molecular anchoring to the substrate, the recorded  $d_{\text{eff}}$  of the molecular film is 7.71 pm/V, **Figure 22B**. These results correlate with computational predictions computed by Keith Werling and literature predictions of molecular confirmation on the substrate surface.

A previous study of similar low coverage corannulene based molecular films on Au by STM confirm the molecular bowl to favors a bowl down confirmation, conjugated pi system down, on the Au surface.<sup>2</sup> In this confirmation the computed piezoelectric constant,  $d_{33}$ , is ~9 pm/V. The correlation between the predicted  $d_{33}$  of ~9 pm/V and the measured  $d_{\text{eff}}$  of ~8 pm/V indicates the **H4DFT** molecule is likely in a bowl down confirmation on the Au surface. Stockl *et al* provided a systematic study for the standing up of molecular bowls on a metallic surface.<sup>23</sup> Based on Stockl's predictions the carboxylic acid termini of **H4DFT** should provide sufficient anchoring, chemisorption, to the ITO substrate to stand the molecular bowl up on its edge on the surface. The computationally predicted  $d_{33}$  for **H4DFT** in a standing conformation is ~20 pm/V. At roughly 20 pm/V the computationally predicted value is lower than the experimentally determined effective

constant but does not include the possibility of a wagging type motion of the unanchored benzoic acid groups. Thus, illustrating the possible effect of molecular orientation on resulting electromechanical response of the molecular based film.

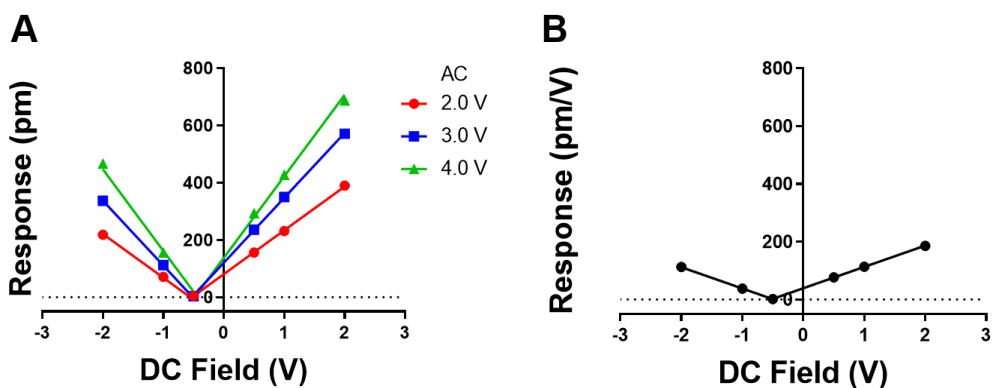


**Figure 22** (A) Effect of applied DC field on H<sub>4</sub>DFT film on Au response at various AC fields using 0.09 N/m levers. (B) DC-dependent response after removal of the AC field and averaging at each DC field.

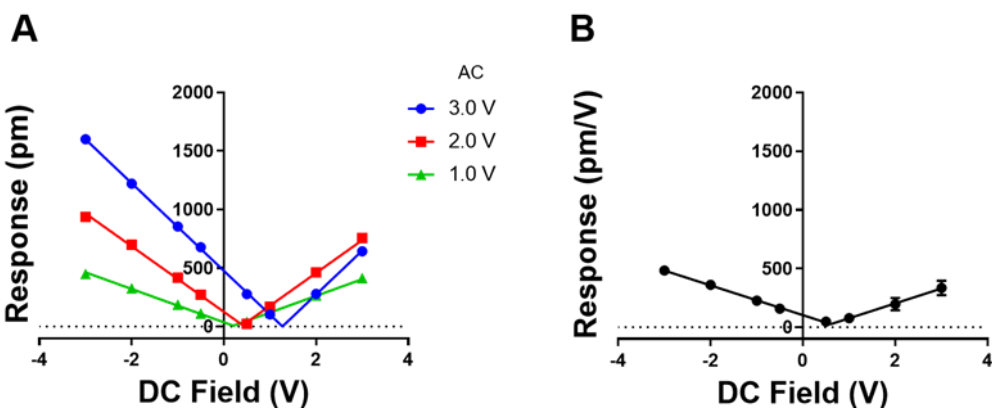


**Figure 23** (A) Effect of applied DC field on H<sub>4</sub>DFT film on ITO response at various AC fields using 0.09 N/m levers. (B) DC-dependent response after removal of the AC field and averaging at each DC field.

To ensure the sizeable measured response from the **H4DFT** film is due to the conformational changes of the bowl shaped molecular film and not an effect of the substituents or the conjugated pi system, a control molecule, 1-pyrenecarboxylic acid **Figure 24 A**, was tested based on its similar pi system and acid termination. These features should allow the 1-pyrenecarboxylic acid to adopt the same confirmation as **H4DFT** on the ITO surface. The resulting response curve from the DC Sweep DART-PFM experiment, **Figure 24C**, gives a  $d_{\text{eff}}$  electromechanical response of 0.291 pm/V when deposited on an ITO surface from a 0.125 mM solution. Thus, confirming the large piezoelectric response of the **H4DFT** film is likely due to its molecular bowl confirmation, not the conjugated pi system or the anchoring carboxylic acid.

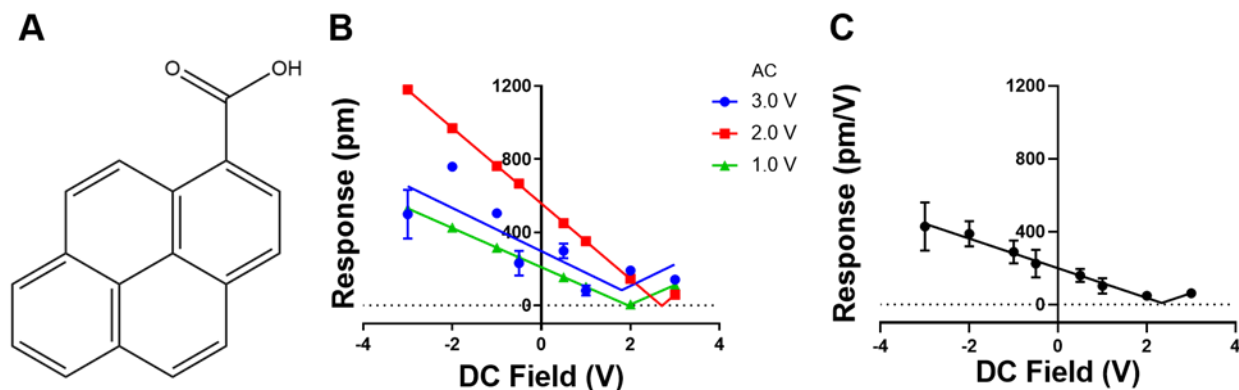


**Figure 24** (A) Schematic of 1-pyrenecarboxylic acid (B) Effect of applied DC field on 1-pyrenecarboxylic acid film on ITO with responses at various AC fields using 0.09 N/m levers. (C) DC-dependent response after removal of the AC field and averaging at each DC field.

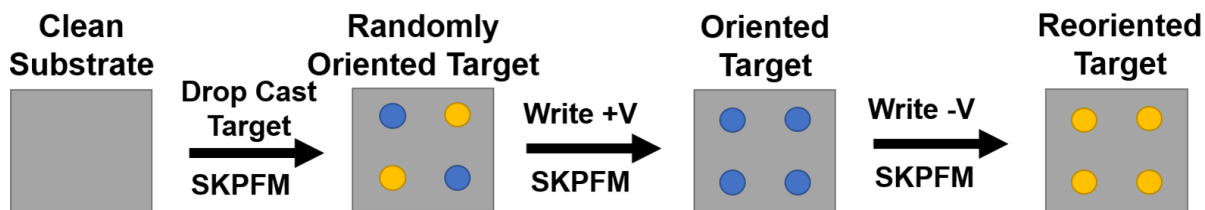


**Figure 25** Schematic of planned experimental procession for the confirmation of ferroelectric properties of **H4DFT**.<sup>2</sup>

With the confirmation of the piezoelectric properties of **H4DFT**, a schematic of the experimental plan to isolate its ferroelectric properties is outlined in **Figure 25**.<sup>10</sup> Here, it is hypothesized that when **H4DFT** is drop cast on to a clean ITO surface, the molecules are initially randomly oriented. Once a directional DC field is applied to the substrate, the molecular film will reorient, creating a uniform orientation of the molecules on the surface, akin to the polling process for classical piezoelectric materials.<sup>2, 12</sup> This reorientation can then be enhanced by applying fields of increasing magnitudes until the maximum field possible,  $\pm 10 \text{ V}_{\text{DC}}$  via the standard orca holder for the MFP3D, is reached, at which point the magnitude of the applied field is inversed until the opposite magnitude field is achieved. During this process, after each time a new field is applied to the substrate, the surface potential of the film is measured by sKPFM to quantify any changes in the electronic structure of the film.

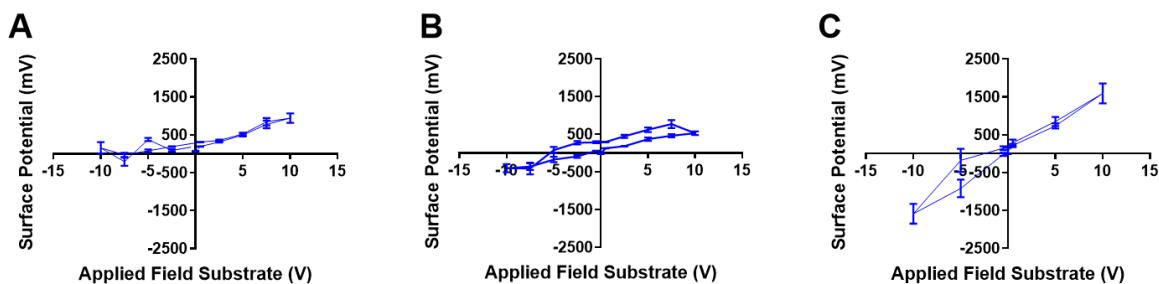


**Figure 26** SKPFM surface potential of **H4DFT** on ITO after an applied DC field to substrate (**A**) 0.5 minute poling, (**B**) 1.0 minute poling, and (**C**) 2.0 minute poling, error bars represent the distribution of measured surface potentials over at least four samples.

**Figure 26** illustrates the resulting hysteresis loops from the sweeping of the applied DC field to the conductive substrate at different dwell times. Here the “memory” of the molecular film to the applied field increases with increasing poling periods. The most significant conformational memory occurred at a two-minute poling period under negative DC fields; but a minute poling period represents the most uniform remnant polarization. The effect of poling duration on the surface potential memory of the material is not unique to this material system. With traditional ferroelectric materials, the reorganization of the net polarization should occur on a vibrational time scale upon the application of an electric field but often requires a poling period to elucidate.<sup>1, 2, 15, 24, 30</sup> This change in polarization is generally affected by the magnitude and frequency of that field, not the duration.<sup>1, 24</sup>

Unlike traditional ceramic materials, like lead zirconium titanate (PZT) where the ferroelectric character is determined by the degrees of displacement of the central atom in the unit cell, the polarization effect in **H4DFT** is derived from conformational changes in the molecular film. Likened to the poling process used with classic piezoelectric materials in which the duration of the applied field plays a pivotal role in the net polarization of the material. Since the molecular monolayer must reorient under the applied field to generate a change in the net polarization, a

likely hindrance in the reorientation exists. This hindrance is likely caused by intermolecular interactions, molecule-molecule binding within the monolayer. Additionally, the samples are grounded during and after the application of the applied field, indicating that the memory effect witnessed in the differing surface potentials of the material is likely due to a conformational change in the molecular film, not a charging effect. This is further confirmed by the duration of the experimental process in which each point in **Figure 25** requires approximately thirty minutes to collect, allowing enough time for charge dissipation of the film. This indicates that the effect of the poling duration is likely due to steric type hindrances due to the high packing densities of a well-formed monolayer.

The resulting magnitude of the film memory, how open the hysteresis loop is, for the **H4DFT** film on ITO is low under ambient conditions. This is likely due to the film being at a more paraelectric state than ferroelectric.<sup>1, 15</sup> Ferroelectricity is a temperature-dependent phenomenon in which the magnitude of the macro dipole memory will increase with decreasing temperatures—indicating that ambient conditions are near or above the requirements for the optimal ferroelectric character of the **H4DFT** film to be measurable by the surface potential methodology.

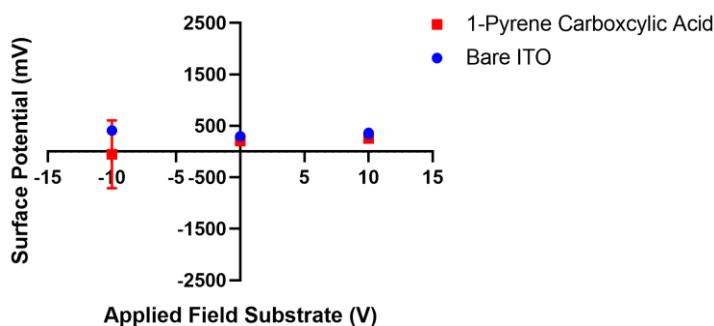


**Figure 27** SKPFM surface potential of a bare ITO surface, blue, and a monolayer of 1-pyrene carboxylic acid, red, after applied DC field, to substrate with a b 1.0 minute poling period, error bars represent the distribution of measured surface potentials over multiple samples.

Using the above outlined experimental procedure, a bare ITO surface and a **1-pyrenecarboxylic acid** film on ITO were tested as controls for the **H<sub>4</sub>DFT** molecular film. These samples demonstrated little to no change in surface potential at maximal applied fields,  $\pm 10$  V<sub>DC</sub>, further indicating the observed response in **H<sub>4</sub>DFT** is due to its para/ferroelectric nature not an artifact of the substrate or a charging mechanism as illustrated in **Figure 27**.

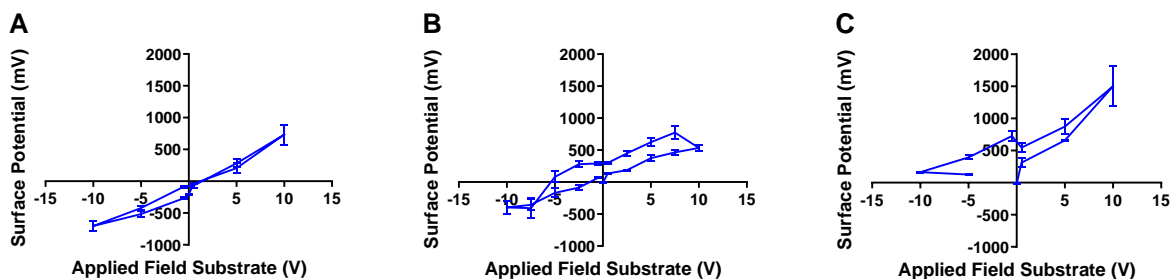


**Figure 28** SKPFM surface potential of **H<sub>4</sub>DFT** on ITO after an applied DC field to the substrate at (A) 17.0 °C, (B) 21.0 °C, and (C) 28.0 °C after a 1.0 min. dwell time; error bars represent the distribution of measured surface potentials over at least two samples.

To isolate the onset of ferroelectric character in the **H<sub>4</sub>DFT** film, a set of temperature-dependent experiments were conducted using a 1.0 min dwell time, representing the most consistent remnant polarization in **Figure 26**. **Figure 28** illustrates the increase in remnant polarization, witnessed by the change in surface potential, with decreasing temperature. This trend towards increasing remnant polarization with decreasing temperature is consistent with classical ferroelectric behavior.<sup>1, 24, 31</sup> Here, the molecular film's response to the external stressor moves from a more paraelectric state to a more ferroelectric with decreasing temperature. These results indicate that the **H<sub>4</sub>DFT** film is undergoing a conformational change to the applied field and not a redox mechanism, as this would result in no temperature effect. Additionally, the shift in surface potential from native conditions to the initial application of an electric field increases with

decreasing temperature. Thus, indicating that the initial reorganization of the film to the applied field becomes more uniform with the decrease in temperature.

#### 4.5 Conclusions

Here in a predicted ferroelectric material, **H4DFT**, was tested and confirmed to likely be in a transition state from a more paraelectric to more ferroelectric state near ambient conditions. The molecular film's remnant polarization to an applied field, optimized at a 1-minute poling period, indicates the film's ferroelectric character. However, long poling times are required to generate this conformational change in the film. Suggesting that the molecular dipoles of the film are not free to reorganize spontaneously, likely due to the chemisorption of **H4DFT** to the ITO surface through the acid terminated substituents on the corannulene, indicated through the correlation of the measured piezoresponse with the computationally predicted values. Further, **H4DFT** displays changes in the magnitude of the remnant polarization with a corresponding change in temperature. Indicating that the ten-degree window tested represents the transition from a paraelectric to a more ferroelectric state for **H4DFT** film on ITO. Moreover, **H4DFT** was confirmed to be piezoelectric with a significant piezo coefficient,  $> 26$  pm/V, more than eight times higher than previously reported molecular films.<sup>6, 8, 17, 24, 32</sup>

Finally, the **H4DFT** molecular film represents a new class molecular structures that are both highly responsive and biocompatible. Still, further testing is required to isolate the conditions necessary for a sizeable conformational memory and to isolate the mechanism responsible for the long poling periods needed for the exhibition of ferroelectric character.

## 5.0 Lab Scale Manipulation of Single and Multilayer Organic Self Assembled Structures

This chapter has been adapted with permission from:

- Miller, N.C.; Hutchison, G. R. Robust Photopatterning of Gold-Thiol Self-Assembled Monolayers. ChemRxiv. Preprint.

### 5.1 Introduction

Nanoscale materials are prized for their unique and tailorable surface properties. To control surface properties, self-assembled monolayers (SAMs) are often implemented as model systems based on their ability to form highly tailorable, organized, and precise structures.<sup>1-9</sup> These attributes have driven the development of many patterning approaches for SAMs, in pursuit of increased tailorability for various applications such as nanoscale electronics.<sup>2, 3, 5, 10-12</sup> Patterning techniques have included micro-contact printing ( $\mu$ -CP), subtractive transfer printing, scanning probe-based lithography, energetic beam lithography, and many others.<sup>2, 7, 8, 11, 13-16</sup> These techniques though adaptable, are often limited in scalability and ease of adaptation to new systems.<sup>7, 17</sup> Alternatively, photolithography, specifically UV photolithography (UVPL), has been shown to be a robust and scalable technique for patterning nanoscale soft materials.<sup>3, 14, 17-20</sup> Photolithography, as a non-contact method, minimizes potential for contamination and enables the production of arbitrarily complex architectures. UVPL uses a photomask placed on or above a SAM, which serves as the photoresist for UV photons. The exposed area of the SAM is

photooxidized (e.g., thiols to sulfoxides)<sup>21-23</sup> and can be removed or replaced by a secondary SAM either through sonication or an exchange mechanism.<sup>9, 14, 19, 24-26</sup>

In this work, we will quantify the kinetics controlling the photooxidation of Au-thiol SAMs serving as photoresists and gain insight into the stability of the resulting patterned SAM for future device implementation. These aspects will be probed using scanning Kelvin probe force microscopy (sKPFM) and x-ray photoelectron spectroscopy (XPS). Previous work has indicated that a minimum threshold of intermolecular forces must be achieved for SAMs to remain stable during the photooxidation process.<sup>22, 23, 27-29</sup> This threshold can be reached via long backbones or substituents that generate increased intermolecular interactions such as hydrogen bonding.<sup>7</sup> Additionally, research has probed the mechanism for photooxidation with some results showing that the presence of ozone is not required for the oxidation of the Au-thiol bond but is a likely catalyst.<sup>22, 23, 28, 30</sup> Although previous work has generated insights into the reactions occurring at the Au-thiol interface, it has yet to quantify the kinetics required for the photooxidation process to occur. Additionally, the long-term stability of SAMs and the induced patterns must be tested.

## 5.2 Experimental Methods

### 5.2.1 Materials

SAMs were formed from 16-mercaptohexadecanoic acid (MHDA) (90%), 11-mercaptoundecanoic acid (MUA) (95%) and 1-dodecanethiol (DDT) (>98%) in pure ethanol purchased from Sigma Aldrich and used without further purification. Au-thiol SAMs were formed on Bio Gold substrates (90 nm Au with 10 nm Ti adhesion layer on glass)<sup>31</sup>, which were purchased from Thermo Fisher Scientific. TEM grids were used as low-cost, robust photomasks. Grids were purchased from TED PELLA Inc. with three different mesh types to give multiple local aperture sizes: glider 2000 mesh Cu grids, glider extra fine 2000 circular mesh Cu grids, and glider 400 mesh Cu grids (~56  $\mu\text{m}^2$ , 33  $\mu\text{m}^2$ , and 1370  $\mu\text{m}^2$  feature sizes respectively).

### 5.2.2 Sample Preparation Protocols

Substrates were used after a cleaning process consisting of multiple ethanol and ultrapure water (generated from a Millipore Synergy system, resistivity = 18.2 M $\Omega$ cm) washings before sonication in ethanol for 15 min followed by drying under a N<sub>2</sub> flow. Monolayer samples were prepared by placing the clean substrate in 1 mM ethanolic solutions of the target material for a period of 24 h to ensure maximum uniformity of the resulting monolayer. After the incubation period the sample were rinsed with ethanol and water then dried under an N<sub>2</sub> flow before being placed in a UV blocking container and stored under vacuum.

### 5.2.3 Scanning Kelvin Probe Force Microscopy (sKPFM)

Atomic force microscopy (AFM) measurements were carried out on an Asylum Research MFP-3D atomic force microscope with an N<sub>2</sub> gas purge to maintain relative humidity in the research chamber below 30%. Scanning Kelvin probe force microscopy (sKPFM) measurements were conducted with ASYELEC.01 R2 (R2) silicon cantilevers with an iridium/platinum (5/20) coating on the tip/lever (purchased directly from Asylum Research).<sup>32,33</sup> R2 probes have a spring constant ( $k_i$ ) of  $2.8 \pm 1.4$  N/M, a tip radius of  $25 \pm 5$  nm, and a resonant frequency of 70 Hz. SKPFM mode on the MFP-3D utilizes a conductive probe that is maintained at a set delta height (distance above the sample based on the frequency tune of the tip and the initial topography scan) and not driven at its resonant frequency. Instead, a DC field is established between the tip and sample where a feedback loop cancels out tip vibrations caused by variations in the contact potential difference ( $V_{CPD}$ ) of the sample surface. To maintain scan stability while increasing resolution, the delta, and scan heights were kept at 40.0 nm.<sup>33</sup> No sample grounding is required due to the low dielectric nature of the organic monolayers being investigated.<sup>33</sup> All resulting sample data were processed using Asylum Research software version 14.23.153 using Igor Pro version 6.37.

### 5.2.4 X-Ray Photoelectron Spectroscopy (XPS)

All XPS measurements were conducted on a Thermo Fisher Scientific ESCALAB 250XI XPS utilizing an Al  $K\alpha$  x-ray source (1486 eV) in constant analyzer energy mode. The use of maximum allowable spot size, 900  $\mu$ m, and sample surface neutralization (*via* an ion gun) were implemented to overcome the low density and insulating nature of the SAMs under study.

Additionally, the samples were analyzed at higher pass energies and longer dwell times with increased averaging to optimize the signal to noise ratio.<sup>30</sup>

### **5.2.5 Transmission Electron Microscopy (TEM)**

An FEI-Morgagni transmission electron microscope (TEM) was used to image the mesh photomasks. Collected images were then processed using Image J software version 1.48 to calculate photomask parameters.

### **5.2.6 Photolithography**

UV induced soft photolithography was carried out using a 175 W GE47760 metal halide bulb held at variable distances from the sample surface. The radiation dosage was optimized to ensure minimum exposure period while maintaining a wide exposure window to allow for precise pattern manipulation. The optimization was performed by measuring the intensity at variable distances and then converting the intensity to total energy exposure to the exposure period. The incident intensity was measured using a Coherent Field Mate laser power meter coupled with a Coherent Power Max PM10 detector. After exposure, the resulting SAM can then be exposed to a secondary SAM material for replacement or sonicated to be removed from the surface to fully develop the pattern (it is noted that a patterned monolayer does exist before this step).<sup>28</sup>

### 5.3 Results and Discussion

UV photolithography (UVPL) is a low cost, robust, and scalable technique for introducing desired patterns into soft organic materials. Previous work has focused on applications of UVPL for the patterning of Au-thiol SAMs, but not focused on calibration and quantification of the lithography process for this application.<sup>18, 28, 29</sup> A photodetector was implemented to quantify the parameters of the lithography system. Specifically, to ascertain the magnitude of the incident irradiation (dosage) present at various source-sample distances. To maintain system simplicity, thus allowing for greater ease of application, columnated light was not implemented in the lithography system, but a short pass UV filter was implemented to reduce sample heating from stray IR radiation.

It is well known that the incident intensity from the radiation source decreases at a rate of  $r^{-2}$ .<sup>14</sup> In **Figure 29A** a calibration of incident intensity, 175 W source measured at center of the UV emission peak  $\lambda \sim 380$  nm, vs. source-sample distance gives a relation of  $r^{-1}$ .<sup>33</sup> This result deviates from theory in part due to the reflective nature of the shielding used as an engineering safety barrier, generating an increase in background radiation impeding on the detector. This coupled with localized heating of the detector, from other reflected unfiltered wavelengths, gives rise to the slower drop off in incident intensity over space. Beyond quantifying the incident intensity, the total energy exposure was calculated as a function of time, at a source-sample separation of 5.0 cm (**Figure 29B**) after an initial warming period.

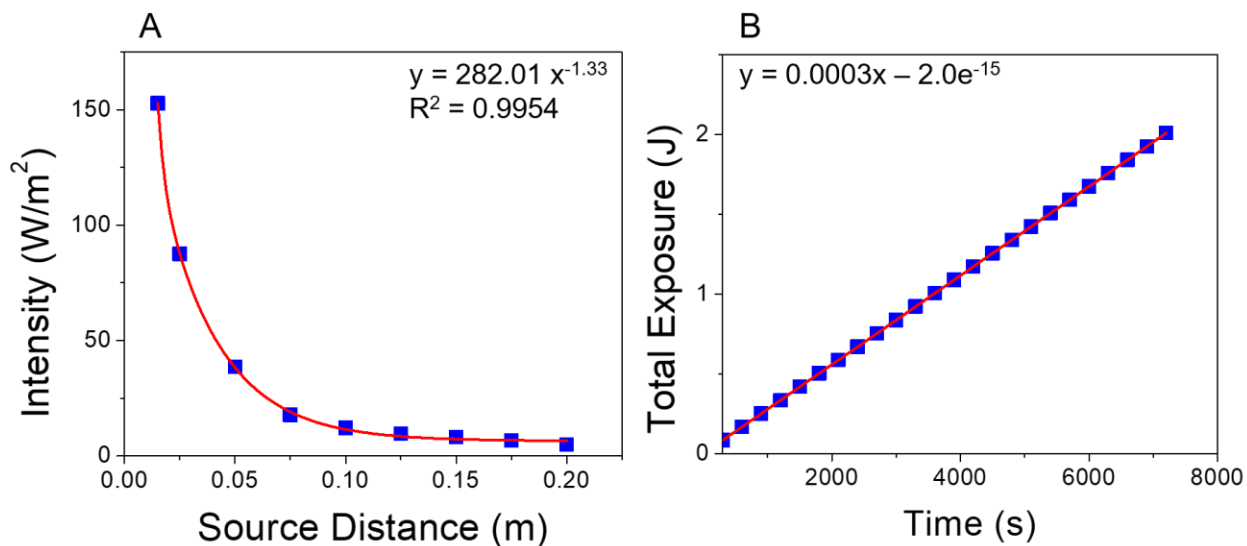


**Figure 29** (a) Rate of change in the incident intensity over a change in source-sample distance for a 175 W metal halide light source measured at  $\lambda = 380$  nm after filtration. (b) Calibration curve for the total energy exposure to a sample surface with a source-sample distance of 5.0 cm from a 175 W source for a given period.

Given an accurate calibration of radiation dosage, the relation between the local aperture size of the mask and the resulting SAM pattern size can be considered. The local aperture size in this case is determined by the mesh of the transmission electron microscope (TEM) grid used as a photomask. While any photomask could be used, commercial TEM grids provide a wide variety of choices at minimal cost with robust feature sizes. As photomasks, the precise feature sizes associated with each TEM grid mesh type was determined using a TEM. Representative samples of each grid were viewed under high magnification with at least eight holes in each image. After collection, each image was processed using ImageJ software to precisely calculate the width of the bar and the area of each hole in the grid, considering the rounded corners of the square mesh grids. **Table 7** lists the measured feature sizes, averaged over at least ten grids sampled from multiple

lots. Unless otherwise noted, these dimensions will be the assumed feature sizes used for pattern calibrations below.

**Table 6** TEM grid feature sizes with expected specification sizes, and TEM-measured average feature sizes including standard errors over at least ten samples.

Grid Type	Specified Hole Area ( $\mu\text{m}^2$ )	Hole Area ( $\mu\text{m}^2$ )	Specified Bar Width ( $\mu\text{m}^2$ )	Bar Width ( $\mu\text{m}$ )
400 Square	1369.0	$2038.3 \pm 57.5$	25.0	$28.61 \pm 0.42$
2000 Square	56.3	$70.01 \pm 1.31$	5.0	$5.92 \pm 0.08$
2000 Circular	33.2	$52.16 \pm 0.85$	6.0	$5.04 \pm 0.13$

Photopatterning of SAMs consists of a photon source (UV light), a photo mask (TEM grids), and a photoresist (SAM). The photon source is generally a metal halide bulb capable of emitting UV photons.<sup>4, 20, 26, 28</sup> The UV light generates localized radical oxygen species that detectably oxidize the thiol terminus of the SAM. Hindering this technique is the localized heating of the SAM by infrared radiation present from the light source causing degradation of the film. Zhou *et al.* previously reported a threshold of intermolecular interactions necessary for stable UV photooxidation of Au-Thiol SAMs by using alkane thiols with a backbone length of  $\geq 12$  carbons or a tail group capable of hydrogen bonding.<sup>28</sup> With a stable oxidized SAM exchange or removal, *via* exposure to a fresh thiol solution or sonication respectively, is possible due to the lower bond energy between the oxidized thiol and the Au surface.<sup>21, 28</sup> Given the previous exploration of this system we chose to use 16-mercaptohexadecanoic acid (MHDA) and 11-mercaptopundecanoic acid (MUA) as the photoresist SAMs ensuring both the stability of long alkane backbone and from the intermolecular hydrogen bonding from the carbocyclic acid tail group.

MUA SAMs were formed on Au coated glass substrates from a 1 mM MUA ethanol solution and exposed to varying amounts of UV radiation, using a 2000 square mesh TEM grid as the photomask. Once photooxidized, the films were placed in a 1 mM 1-dodecanethiol (DDT) ethanol solution for exchange.

To visualize the patterned SAMs, sKPFM was used to provide surface potential contrast between the MUA and DDT regions – the two SAM ligands are similar in height (15 Å vs 15 Å for MUA and DDT respectively) so that minimal topographic or phase contrast is present.<sup>34</sup> In particular, the sKPFM images can be used to determine optimal exposure times in which the resulting patterns match the expected feature size from the TEM photomask itself. A film is thus defined as underexposed when the resulting surface feature is smaller than the local-aperture dimensions and overexposed when the surface feature exceeds the dimensions of the aperture.<sup>17, 19, 35</sup> The relationship between the onset of photooxidation and optimal exposure is illustrated in **Figure 30**. In the sKPFM images, the darker background represents the unphotooxidized MUA SAM used as the photoresist, and the brighter regions represent the DDT replacement of photooxidized MUA.

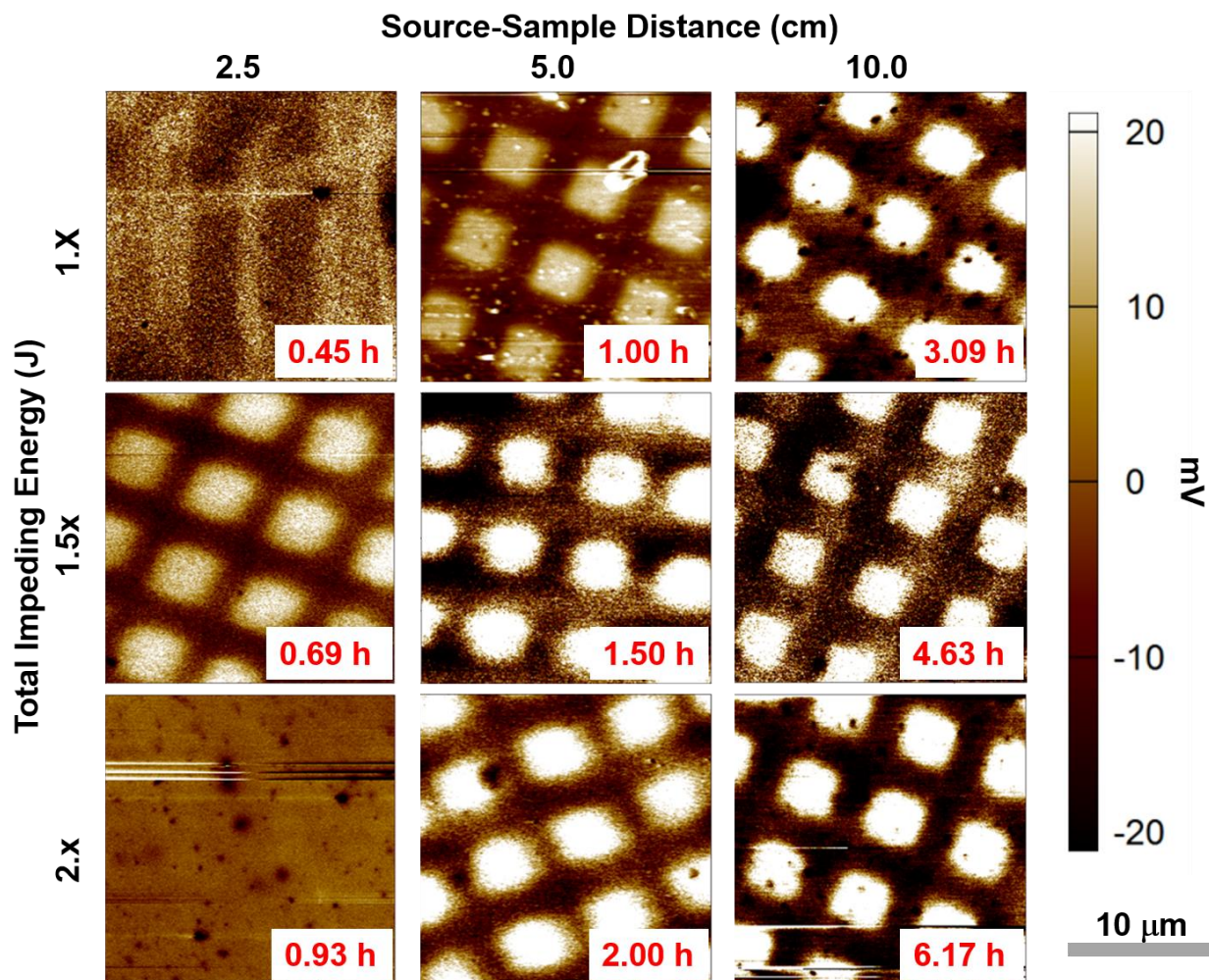


**Figure 30** SKPFM images illustrate the influence of total energy exposure and incident intensity on pattern formation. The inset times represent the exposure period at a given source-sample distance.

These results in **Figure 30** indicate that a dosage equivalent to 1.5 J is required for robust pattern formation with this Au-Thiol system. When the incident intensity is high (e.g., 2.5 cm source-sample distance), the period needed to reach 1.5 J is short ( $\sim 0.69$  hr); and the exposure window between under and overexposure is equally limited. In comparison, when incident intensity is low (e.g., at 10.0 cm source-sample distance), the exposure window becomes so large that after six hours of UV exposure the photoresist is still underexposed. An optimized balance

between controllable exposure and minimal operation time is at an approximate incident intensity of  $38 \text{ W/m}^2$ , correlating to a source sample distance of 5.0 cm. In addition to using sKPFM, topographic contrast was attempted by exposing 16-mercaptohexadecanoic acid (MHDA) monolayers and exchanging with DDT (i.e., an expected height of  $20 \text{ \AA}$  and  $15 \text{ \AA}$  for MHDA and DDT, respectively), but greater contrast between the two regions was still found with sKPFM than with topology.

Using an optimal dosage of  $38.20 \text{ W/m}^2$ , the relationship between local aperture size and resulting film features was determined. **Figure 31** illustrates how the pattern feature size is affected by local aperture size for an MUA/DDT system. Both a 2000 square mesh and 2000 circular mesh were used, resulting in pattern features to be varied from the smallest reported feature size  $45 \text{ \mu m}^2$  up to  $80 \text{ \mu m}^2$  before the resulting pattern is overexposed. In contrast, the shift in local aperture size from  $52$  to  $70 \text{ \mu m}^2$  does not increase the sample dosage for the onset of pattern wash, where the film is wholly oxidized resulting in no discernable pattern after ligand exchange. There is a notable shift between the two types of mesh for the point at which the patterned feature sizes equals the aperture size (i.e.,  $\sim 2.2 \text{ J}$  for the 2000 square mesh vs.  $\sim 1.8 \text{ J}$  for the 2000 circular mesh). This difference is likely due to the square mesh grids having 16.7% larger bar areas. The larger surface area of the square mesh itself absorbs more of the incident photons requiring a higher dosage to achieve equivalent feature sizes in the SAMs. This confirms that resulting feature size and pattern quality is ultimately controlled by quantifying and tuning the incident intensity, not the photomask.

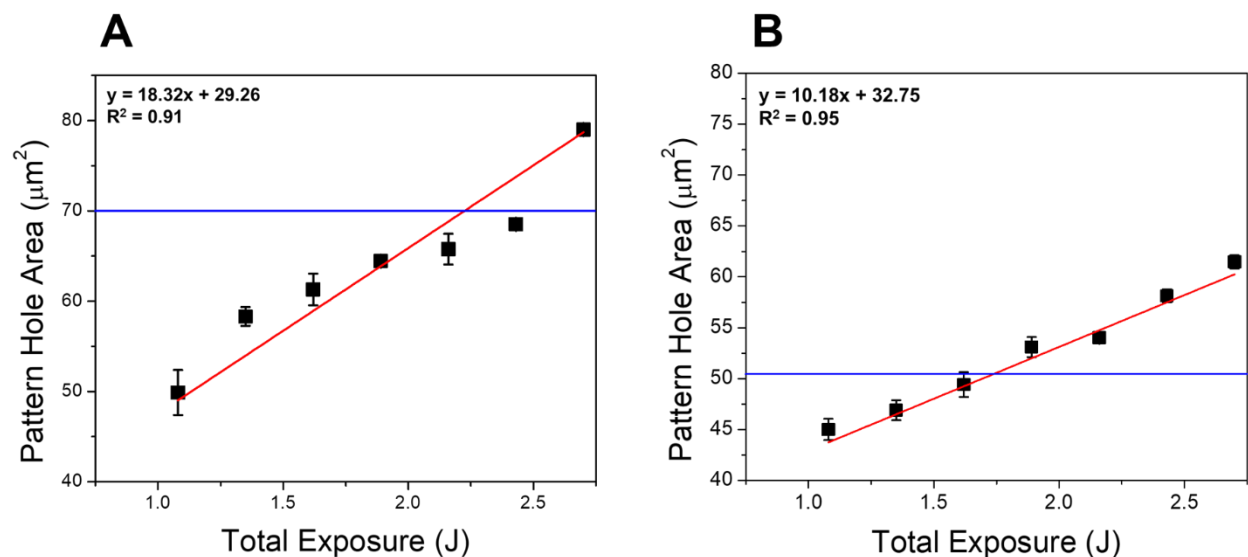


**Figure 31** Calibration curves for the average relation between total energy exposure and pattern hole area for a given aperture size in which the error bars represent the standard error from at least eight features. (a) Change in pattern hole area for an MUA SAM patterned and backfilled with DDT using a 2000 square mesh TEM grid as the photomask. (b) Change in pattern hole area for an MUA SAM patterned and backfilled with DDT using a 2000 circular mesh TEM grid as the photomask. The blue lines represent the pattern hole areas of the TEM grid masks used (**Table 7**). The red lines represent the line of best fit for which the equation of the line and the  $R^2$  are provided within in the individual plot.

Finally, the long-term stability of the resulting patterned films must be tested. It has previously been shown that alkane-thiol monolayers can oxidize in atmospheric conditions.<sup>36</sup> **Figure A26** illustrates that, when properly stored, the autoxidation of the films can be mitigated. By using XPS to monitor the oxidation in the  $S_{2p}$  lines, the effectiveness of various storage conditions can be examined. In **Figure A26** a notable shift in the unoxidized  $S_{2p}$  peak at 162 eV to an oxidized  $S_{2p}$  peak at 168 eV occurs when films are left in environmental conditions, but no shift in the  $S_{2p}$  line occurs when films are placed in UV protected containers and stored under

vacuum.<sup>30</sup> Therefore, if samples placed in UV blocking containers (e.g., aluminum foil wrapped Petri dishes) and stored under vacuum, there is no detectable oxidation of the Au-thiol bond by XPS after one week. Indicating the autooxidation of the Au-Thiol bond can be easily prevented; resulting in increased stability derived from the removal of atmospheric oxygen (oxidation source) and UV photons (catalyst), thus providing long-term stability of the films.

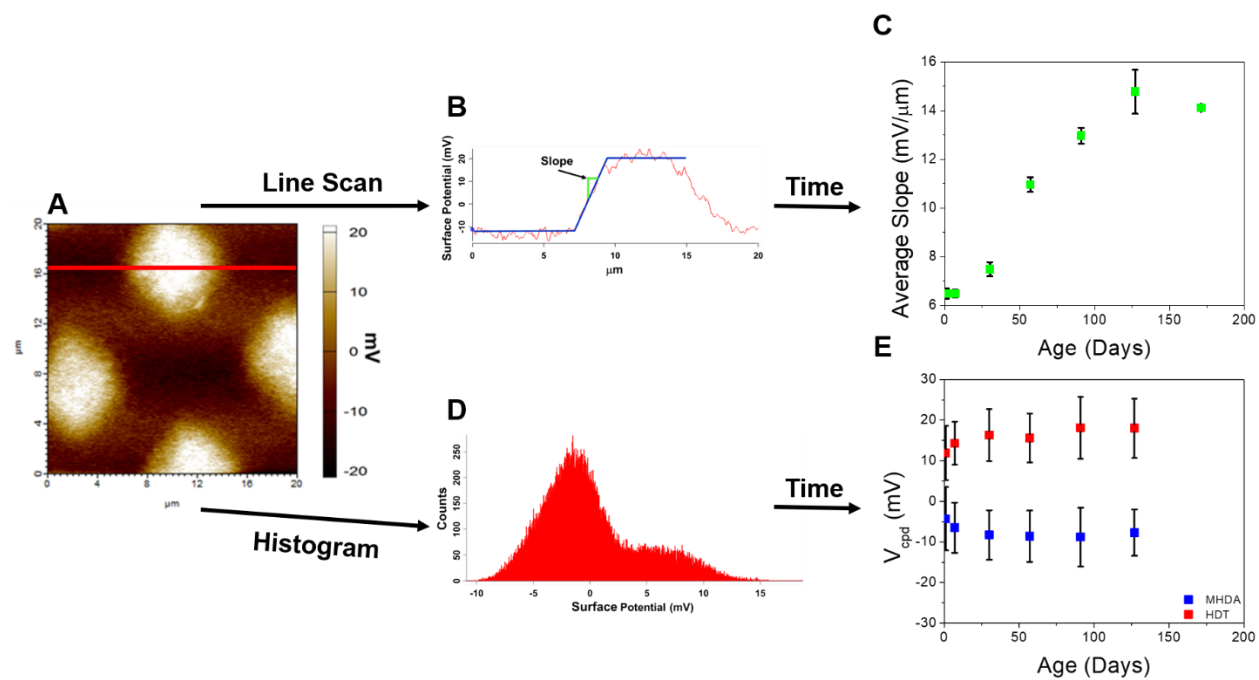


**Figure 32** (a) Example sKPFM potential scan of a patterned monolayer of MHDA/DDT using 2000 square mesh TEM grid as the photomask. (b) Resulting line scan from (a) indicating how the slope of the pattern interface is determined. (c) The migration of the pattern hole edge through the monitoring of the slope of an MHDA/DDT interface in a patterned film by sKPFM. (d) Example histogram of sKPFM potential scan of a patterned monolayer of MHDA/DDT using 2000 square mesh TEM grid as the photomask, all histograms SI figure 7. (e) the change in the  $V_{CPD}$  of the pattern with the sample age as monitored by sKPFM in which blue represents the  $V_{CPD}$  of the MHDA and DDT respectively.

Beyond photo-oxidation of the SAMs, the long-term stability of the patterns themselves were examined by monitoring edge migration along a hole/bar interface by sKPFM and the variation of the  $V_{CPD}$  in both regions over time, **Figure 32**. **Figure 32 A-C** walks through the process used to determine the slope of the interface between the hole/bar features of the resulting patterned monolayer. Here the potential scan of the sKPFM experiment is extracted and a line scan is performed to get the variation across the scan. A flattened base and maximal line are determined by averaging points in each region. Once these lines are established, the slope between the terminus of one region and the start of the other region is determined. This slope analysis is repeated for four-line scans and features on each potential scan, as illustrated in **Figure 32B**. **Figure 32C** indicates that the slope of the interface between the two the components of the patterned film (MHDA and DDT, respectively) *increases* over time. If entropic mixing between the two patterned areas were occurring, the slope of the interface would decrease with time; establishing an interfacial region with intermediate surface potential. Instead, the slope of the interface increases with time, generating a more well-defined interface as the two materials self-segregate over time.<sup>12,</sup>

24, 37

To confirm the results from the slope measurements the  $V_{CPD}$  was tracked via histograms as well, as illustrated in **Figure 32A, D, and E**. Here the trend toward a higher ordered monolayer causes an increased separation in the bimodal distribution of surface charges, as witnessed by the increased asymmetry in the histograms of the potential scans, **Figure 32C and A25**. This increase signifies that the surface potentials are self-segregating into two distinct populations, rather than becoming more homogenous due to increased intermixing.<sup>12.</sup>

## 5.4 Multilayer Formation

Controllable patterned multilayer thin films are of critical importance for device development for the creation of nanocircuitry and tunable film response. Additionally, multilayers can enhance the contrast of uniform thickness patterned monolayers making the pattern observable using contact and or tapping topography modes on a standard AFM.

### 5.4.1 Multilayer Development Stage 1

**Figure 33** shows the establishment of a patterned monolayer developed to form an hexadecanethiol (HDT) monolayer and backfilled with MHDA to establish a mixed alkane/acid surface. There is approximately 0.13 nm molecular length difference between HDT and MHDA; hence there is no visible pattern in the topography scan by AFM. The KPFM scan reveals the pattern due to a difference in the  $V_{\text{cpd}}$  between the HDT ( $V_{\text{cpd}} = 4.0$  mV) and MHDA ( $V_{\text{cpd}} = -11.2$  mV); which can be further monitored for additional reactions.

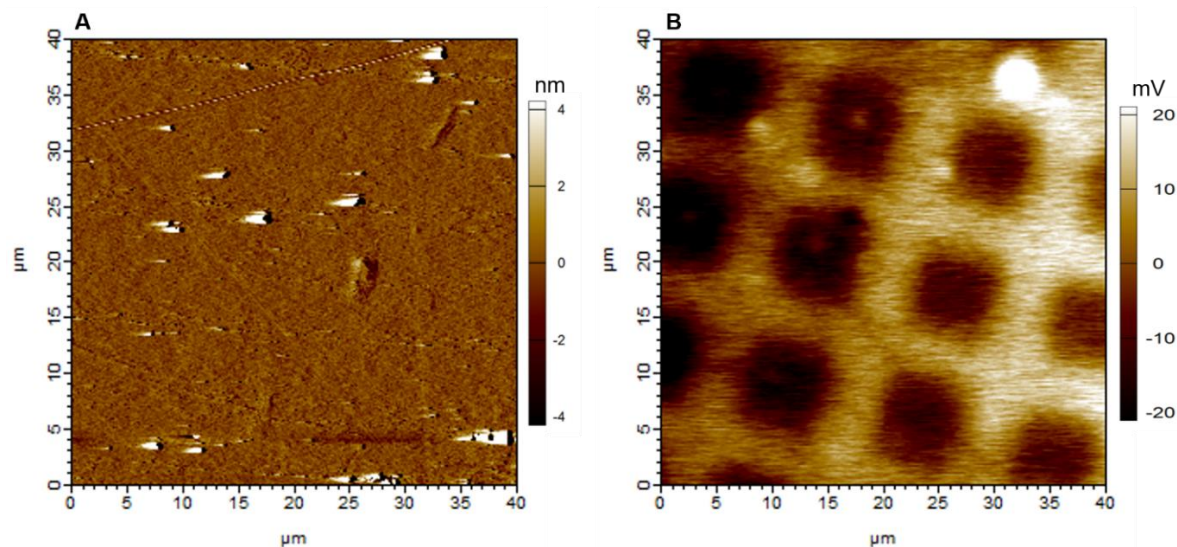


**Figure 33** (A) Amplitude heat map after step 1 of patterned multilayer development and (B) KPFM heat map, both of an **HDT** monolayer patterned and backfilled with **MHDA** using the standard procedure.

#### 5.4.2 Multilayer Development Stage 2

Once the mixed terminal surface was confirmed the acid terminated molecules could be activated through deprotonation by EDC and attachment of PFP to create a selectively reactive film. **Figure 34** shows that the film and pattern will remain intact after further reaction at the surface. The topography scan still displays no visible pattern which is related to the fact that the height difference between the two sections of the pattern should only be approximately 0.4 nm. Though this height difference is greater than that after step 1 it is still at the resolution limit of the AFM. Again, the maintenance of the pattern and the activation of the acid-terminated molecules can be confirmed by KPFM. The KPFM images show a change in the  $V_{cpd}$  from -11.2 mV to -10.9 mV at the acid terminated sites.

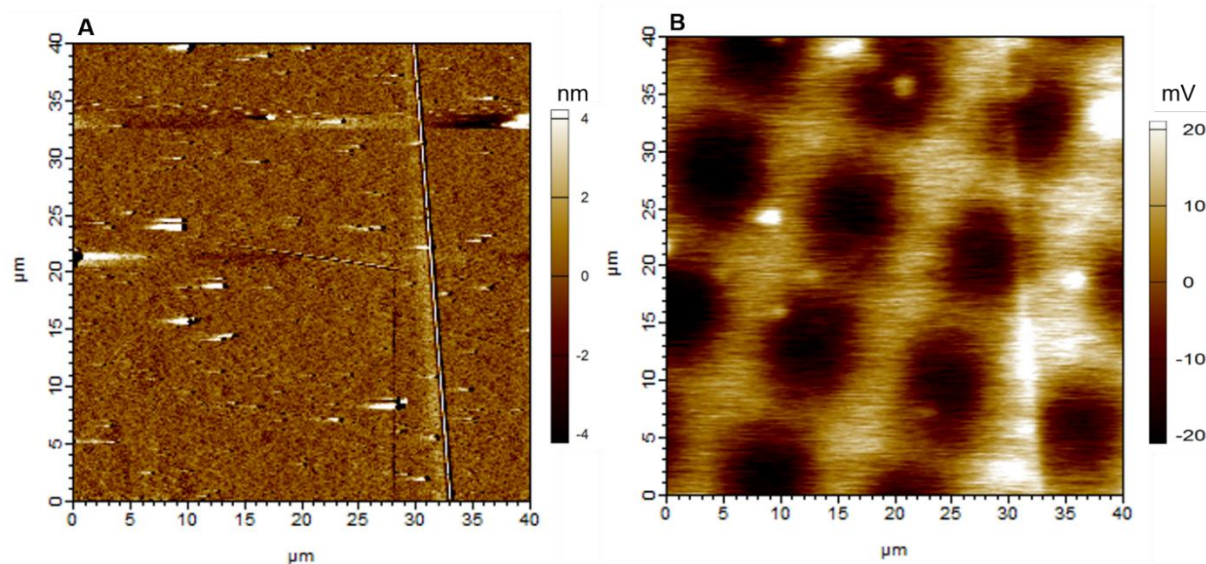


**Figure 34** (A) Amplitude heat map after step 2 of patterned multilayer development and (B) sKPFM potential map, both of an **HDT** monolayer patterned and backfilled with **MHDA** using the standard procedure. The acid terminated sections of the patterned monolayer are then activated with PFP. Giving rise to an **HDT/MHDA-PFP** film.

### 5.4.3 Multilayer Development Stage 3

After the activation of the acid terminated molecules, they are further reacted with DAH to replace the PFP with a diamine. This generates an amine terminated layer that is still Boc-protected to prevent further reactions at the terminus until desired. The topography scan in **Figure 35** does not confirm the attachment of the diamine even though the height difference between the two sections of the pattern should be approximately 0.8 nm. However, the KPFM image in Fig. 14 does confirm the maintenance of the film and the attachment of the diamine through a change in the  $V_{cpd}$  at the acid terminated molecules from -10.9 mV to -5.2 mV.

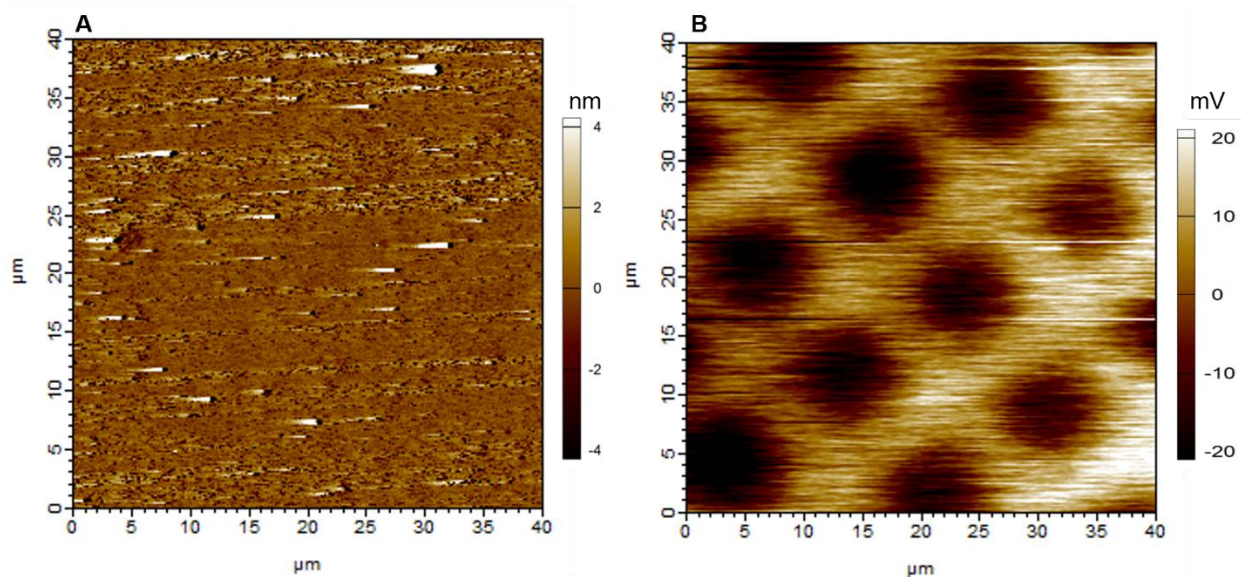


**Figure 35** (A) AFM amplitude and (B) SKPFM surface potential of an **HDT** monolayer patterned and backfilled with **MHDA** using the standard procedure: the acid terminated sections of the patterned monolayer activated with **PFP**, followed by reaction with **DAH** to form an **HDT/MHDA-DAH** film.

#### 5.4.4 Multilayer Development Confirmation

The step by step development of the multilayer was also monitored by XPS. **Figure 36** shows the N1s and F1s XPS lines (all other recorded spectral lines can be found in the appendix). The N1s no observable signal through the first two steps which involves the addition of an acid terminated molecule to the monolayer (black) and its activation by PFP (red), both of which result in a film without nitrogen present. But, step three (blue) involves the addition of a diamine to the film surface which is why there is the appearance of a peak in the N1s line at that step indicating a successful multilayer formation. The F1s line further confirms the progression of the multilayer development by showing the appearance of a peak at step 2 (red) and its disappearance at step 3

(blue), corresponding to the attachment and replacement of PFP on the film surface. It has now been confirmed that it is possible to selectively develop a multilayer on a patterned film making it available for different chemistries down the road. Unfortunately, there is no evidence that the attachment of a single multilayer grants access to film analysis by standard AFM techniques.

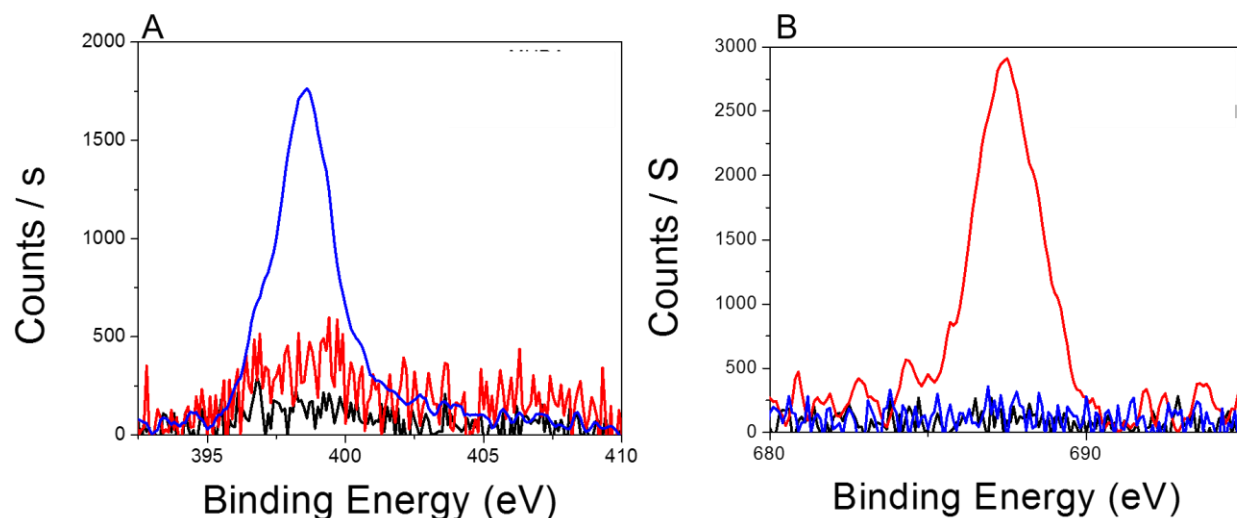


**Figure 36** XPS confirmation of the patterned multilayer development. (A) is the N<sub>1s</sub>, and (B) is the F<sub>1s</sub> lines for an **HDT** monolayer that was patterned and backfilled with **MHDA** (black line), then the acid terminated molecules are activated with **PFP** (red line), and then reacted with **DAH** (blue line). C<sub>1s</sub>, Au<sub>4f</sub>, S<sub>2p</sub> and O<sub>1s</sub> can be found in the appendix.

## 5.5 Conclusions

Photolithographic patterning is widely used in inorganic materials because of the high reproducibility. Through careful calibration, UV photopatterning can be a facile, reliable method for organic SAMs. Using inexpensive TEM grids as shadow masks with well-defined feature sizes and quantifying the impeding energy at the sample surface, it is possible to correlate the resulting pattern features with total energy exposure, allowing a predictive model for the desired feature size. Both underexposure and overexposure can be minimized using well-defined source-sample spacing.

Quantitative pattern control also confirms the stability of the patterned film, both through proper storage and the monitoring of pattern migration at the interfaces across 4 months. Instead of entropic mixing, phase segregation is found, at a slow rate not directly obvious by sKPFM images. Instead, the change in the slope of the surface potential across interfaces can be monitored to confirm pattern stability.<sup>12</sup> Based on this careful calibration of exposure and pattern stability, UV photopatterning of organic monolayers can be used widely, not only for lab-scale processes, but also integrated into micro-nano electronics for future device applications<sup>2, 3, 9, 17</sup>.

Further, with well-defined pattern formations the drive toward well tailor devices can be realized through the formation of multilayer SAMs. The demonstration of *in situ* multilayer formation, confirmed by XPS and sKPFM, provides an additional tool for the future evaluation of previously studied piezoactive materials and the assessment of new materials.

## 6.0 Conclusion and Future Directions

### 6.1 Conclusion

This dissertation has explored the electromechanical properties of molecular-based piezoelectric materials and the measurement systems used to determine their unique properties. The goal of the above-outlined research was to leverage previously computationally predicted insights into the origins of the electromechanical coupling properties in organic molecules to gain experimental insight and create a feedback loop to develop new methods to accurately determine the electromechanical properties of self-assembled monolayers of these predicted materials. Enhancing the accuracy and predictability of future work and drive toward device scale implementation of new materials.

Utilizing atomic force microscopy (AFM), organic molecular self-assembled monolayers (SAMs) were investigated to elucidate their nanoscale properties. A set of tailored macromolecules (peptides and peptoids) was determined to be piezoactive. The lower Young's modulus of the peptide-based monolayers resulted in statistically higher effective-piezo coefficients ( $d_{\text{eff}}$ ) than the higher modulus peptoid motif. Interestingly, the control SAM of dodecane thiol was determined to have similar piezoresponse to the molecular spring structured macromolecules. This phenomenon indicates that the polarization induced by the anchoring of these organic molecules to a metallic surface could likely be a contributing factor to their measured response to applied voltages. Though this is a possible mechanism it is unlikely that these three vastly different molecular structures would give similar response due to the large variance in the theoretical Young's modulus of these films. Due, to this, difficulties with reproducibility, and the large

percentage of error points in all the collected data, due to poor frequency tracking, it was determined that a new method with increased sensitivity to these low-response soft materials needed to be developed to confirm these trends hold true.

Through contact resonance enhancement of the tip-sample interface by dual AC resonance tracking piezo force microscopy (DART-PFM) it is possible to simultaneously increase the sensitivity of the measurement system while reducing the sources of error in the measurement system. This contact resonance enhancement can be further leveraged to enhance the signal to noise ratio of the experiment by using low spring constant levers. With the implementation of lower spring constant levers the molecular films are no longer being restricted by the force applied by the in-contact lever when an electric field is applied. The drawback to this increased freedom is the electrostatic component of the measured film response is no longer being restricted by the lever and must be accounted for to attain the true electromechanical response of the films. Based on the physics controlling the measurement system a new DC-Sweep DART-PFM methodology was developed allowing for the accurate determination of the  $d_{\text{eff}}$  of the previously studied macromolecules, plus several small-molecule controls and crystalline based reference materials. The addition of a DC field sweep to the classical AC field sweep method allows for the determination of the *in-situ* point in which the electrostatic component of the resulting measured electromechanical response is at absolute zero. By implementing this new methodology, we were able to determine that the previously reported responses were attained at the noise floor of the AC sweep methodology and the root cause of the high error density in the collected data. With the retesting of a representative peptide and peptoid, from the previously reported experiments in chapter 2, it was determined that not only were the peptides more responsive than the peptoids; but the likely have a negative effective piezo coefficient.

Further, we confirmed that the dodecane thiol and mercaptoundecanoic acid films have effective piezocoefficients close to zero which is more in line with their small macrodipoles and lack of a low resistance mechanism for molecular deformation. These findings will open the door to the accurate determination of the vast library of “soft” piezoactive materials, as well as those with negative piezo coefficients (meaning the material compresses under an applied field opposed to expanding) that were previously inaccessible by PFM methods.

Leveraging the newly developed DC-sweep DART-PFM methodology in chapter 3 the scope of the possible organic-macromolecular based films that can be tested for piezoelectric character was expanded to include potentially ferroelectric organic materials in which the net polarization of the film can be manipulated with the application of a coercive field. The  $d_{\text{eff}}$  of an example corannulene derivative, tetrabenzoic corannulene (**H4DFT**), was determined and strides towards the confirmation of its ferroelectric properties were made. As stated in chapter 3 for a material to have ferroelectric character it will additionally possess piezoelectric character. Thus, the effective piezoelectric coefficient of **H4DFT** and a control molecule were determined. The effective piezo coefficient of **H4DFT** was found to be much higher,  $\sim 26$  pm/V, than that of the not only the pyrene control molecule but the molecular-spring based peptides/peptoids.

At  $\sim 26$  pm/V the H4DFT film represents an approximately **ten-fold** increase in piezoresponse for this bowl-shaped molecule when compared to the molecular spring-based molecules. With the establishment of the piezoelectric nature of **H4DFT** we could progress to the investigation of its possible ferroelectric properties. Under ambient conditions it was determined that **H4DFT** was likely operating at a near paraelectric state in which there is minimal remnant polarization, but still a nonlinear response to an applied electrical field. This response is likely due to ambient conditions being too high in energy for the ferroelectric properties of the film to

persist. Further temperature-controlled investigations revealed that the **H4DFT** film moves from ferroelectric to paraelectric at near room temperature conditions. Here the remnant polarization of the film was maintained/increased with decreasing temperature, consistent with classical ferroelectric materials. With the likely confirmation of ferroelectric character and relatively high effective piezocoefficients these new bowl-shaped materials, represent a new class of macromolecular based films in the drive toward record organic-based electromechanical materials.

The work conducted in chapters 2 through 4 has steadily expanded the understanding of the design principles necessary for the optimization of organic molecular-based piezoelectric materials. Though important, these strides are useless without the ability to harness these materials and turn them into usable devices. In chapter 5 we explored lab-scale UV photolithography to introduce precise nanoscale patterns into the films. Using representative films formed from small thioalkanes, allowed us to establish the energy requirements to selectively oxidize the gold-thiol bond and replace the oxidized portion of the film with a secondary monolayer. The ability to selectively oxidize parts of a monolayer not only opens the pathway to future device implementation, but a more quantitative assessment of novel piezo and ferroelectric materials by garnering the ability to place control molecules within a molecular-based film. Building upon the successful introduction of patterns to the representative SAMs, we looked to selectively form multilayers within the patterned films. The oxo-amine coupling mechanism was selected for its selectivity for acid terminated molecules allowing for precise control over reaction location and the ease of monitoring reaction progression by sKPFM. This mechanism was demonstrated to garner the ability to control reaction location and form a bilayer by sKPFM and XPS for the first time.

In conclusion, the work represented within this document has proved to further the collective knowledge of the electromechanical coupling characteristics of organic-based molecular films at the nanoscale. Demonstrating the need for a flexible yet well-ordered molecular film for an optimal piezoelectric response from the organic biocompatible materials. Thus, severing as the foundation for the design of more responsive materials and providing methodologies to for the quantitative determination of their nanoscale electromechanical properties.

## 6.2 Future Directions

This section serves as a reference and a starting location for the future investigation of electromechanical coupling in organic-based molecular films at the nanoscale.

The development of a new highly quantitative methodology for the determination of the converse piezoelectric response in soft organic materials in chapter 3 of this document requires the reassessment of the influence of sequence and folding of peptides and.<sup>1,2</sup> By circular dichromatism (CD) there is a trend in both the peptides and peptoids, in chapter 2, for increasing percent helical population in solution. This trend indicates that there should be a gradient from “softer” molecular springs to “stiffer” molecular springs present in the resulting monolayer films of these tailored molecules. The initial investigation of organic molecular spring-based films, implementing known methodologies of the time, was inconclusive towards the effect of this gradient. With the enhanced resolution of the new DC Sweep methodology it may become possible to elucidate the effect of this gradient. The results of which, accurate experimental determination of  $d_{\text{eff}}$ , will enhance the feedback loop between experimentation and computational property prediction by confirming

what molecular properties garner the greatest influence over the resulting properties of the molecular films.

Additionally, in chapter 2 Haley Grim established synthetic pathways to tailorable peptide and peptoid motifs.<sup>2</sup> The piezoelectric response of these molecular springs indicates that softer more flexible backbones lead to higher effective piezocoefficients, peptides ~ 41 % higher than the control DDT and ~ 59 % higher than the peptoids. Artificial peptoids are naturally more flexible than peptoids, but in chapter 2 a R-2-methylbenzyl motif was used in high ratios to increase the backbone rigidity of the synthesized peptoids above that of the peptides.<sup>2-7</sup> With a sequence containing the methylbenzyl motif at lower ratios or the substitution of it for less helical forming side chains such as R-2-cyclohexylmethyl could lead to higher piezoelectric constants.<sup>5-8</sup> The pursuit of more flexible and polar peptoid sequences is advisable considering Gayatri's *et. al* investigation into the computational determination of the origin of negative piezoresponse in peptides witnessed in chapter 3.<sup>9, 10</sup> Gayatri found, based on Werling *et al* work illustrating the negative piezoelectric response of hydrogen bonding to an applied field, that the hydrogen bonds in the backbone of an  $\alpha$ -helical peptide contract under applied fields.<sup>9, 10</sup> This contraction of the hydrogen bonds can be overcome by a large macro dipole assuming there is little steric hindrance in the breathing mode of the molecule.<sup>9</sup> Unlike,  $\alpha$ -peptides the helical forming nature of the peptoids is driven by steric clash and electrostatic repulsions in the side chains rather than hydrogen bonding effectively eliminating the counter active motion of the hydrogen bonding under an applied field.<sup>2, 6, 7</sup> This coupled with higher macro dipoles, achievable through the implementation of more residues in the peptoid, could lead to molecular springs with higher piezocoefficients.

Chapter 5 of this document lays the foundation for the investigation of ferroelectricity on the nanoscale. This work has established a new class of piezoelectric materials with tailorable properties via the foundation of the conformable molecular bowl shape or the constituents placed upon the bowl.<sup>8, 11-14</sup> These synthetic knobs augment the molecular bowl depth, the anchoring motif of the molecule to the desired surface, or both simultaneously. Previous work has shown this class of molecules to invert their macrodipoles under an applied electrical field, but no complete experimental hysteresis loop has been established to ascertain the true ferroelectric character of these molecules.<sup>12, 15</sup> Here, we have established methodologies to extract the ferroelectric hysteresis of molecular films of these materials. **H4DFT** was proven to display para/ferroelectric character around ambient conditions. Quan *et al* computationally predicted the ferroelectric character of corannulene and several other molecular bowls, **Figure 38**. Here, they demonstrated that a fourfold decrease in inversion energy with decreasing molecular bowl depth in corannulene. This is essential since the unsubstituted corannulene and sumanene with bowl depths of  $\sim 0.86\text{\AA}$  will not invert in fields less than  $\pm 10\text{V/nm}$ . In contrast shallower bowl depths found in the unsubstituted pyrene and perylene structures, with bowl depths of  $0.632\text{\AA}$  and  $0.512\text{\AA}$ , display a bowl to bowl inversion at fields of  $\pm 2.83\text{ V/nm}$  and  $\pm 2.8\text{ V/nm}$ , respectively. This indicates with the addition of electron withdrawing groups to the bowl lip of the pyrene and perylene in **Figure**

37, a molecular film with pure ferroelectric character near or at room temperature maybe achievable.<sup>12, 14, 15</sup>

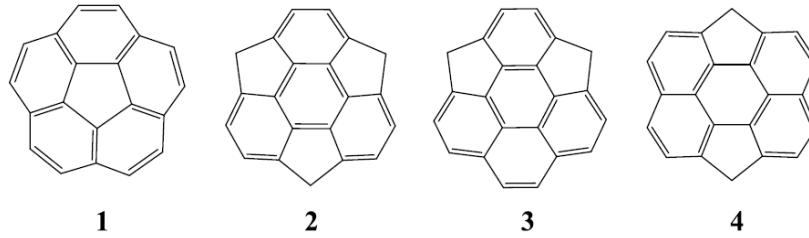


**Figure 37** Scheme of corannulene **1**, sumanene **2**, 1,4-dihydro-as-inaceno[2,1,8,7-cdefg]pyrene **3**, and 1,6-dihydrodicyclopenta[ghi,pqr]perylene **4**. Reproduced with permission from author.<sup>12</sup>

Chapter 6 investigates the implementation of UV-photolithography was optimized for molecular films and the stability of the resulting patterned films was confirmed. This system for pattern introduction must now be expanded to more complex molecular confirmations, such as the direct patterning of molecular springs and bowls, to allow for future device implementation of piezoelectric molecular films. The achievement of controlled pattern introduction in complex molecular films should then be leveraged for the development of films with built-in controls to further enhance the accuracy of the DC-Sweep DART-PFM method developed in chapter 3. Thereby, increasing the accuracy and precision in the screening of new molecular piezoelectric materials.

The controlled photooxidation of gold-thiol bonds can be leveraged to measure the in situ dielectric constants of novel materials at the nanoscale. The selectively oxidized gold-thiol bonds can be cleaved through extensive sonication generating patterns of monolayer vs bare gold. The bare gold can then be used as the reference material for the measurement of the dielectric constant of the monolayers.<sup>16, 17</sup>

$$\epsilon_r(D) = 2h[-2z - R_1 + ((2z + R_1)^2 - 4z(z + R_1) + 4 \left( \frac{(V-V_{sp})^2 \pi \epsilon_0 R R_1}{K(D-D_0)} \right)^{\frac{1}{2}}]^{-1} \quad \text{Eq. 6.1}^{16}$$

By applying **Eq. 6.1** to an sKPFM scan on a patterned sample of bare Au and monolayer the dielectric constant of the monolayer ( $\epsilon_r$ ) with respect to cantilever deflection can be determined. Here  $h$  is the thickness of the monolayer,  $z$  is the initial delta height of the scan over the bare gold minus the cantilever deflection and film thickness ( $h$ ).  $R_1$  represents the tip radius ( $R$ ) minus the product of 1 minus the sine of the tips cone angle. The spring constant of the lever is represented by  $K$  and  $D_0$  is the initial cantilever deflection over the bare Au surface. By obtaining the dielectric constants for piezoactive molecular-based films the classical  $d_{33}$  can be effectively converted to the  $g_{33}$  of the material.<sup>16</sup> The  $g_{33}$  is the piezoelectric voltage constant, equal to the  $d_{33}$  over the dielectric constant  $\epsilon_r$ , which quantifies a material's ability to generate an electric field under applied stress.<sup>3, 18</sup> This value gives insight into the suitability of a material for sensing applications in contrast to the energy harvesting applications of the piezoelectric charge constant  $d_{33}$ .

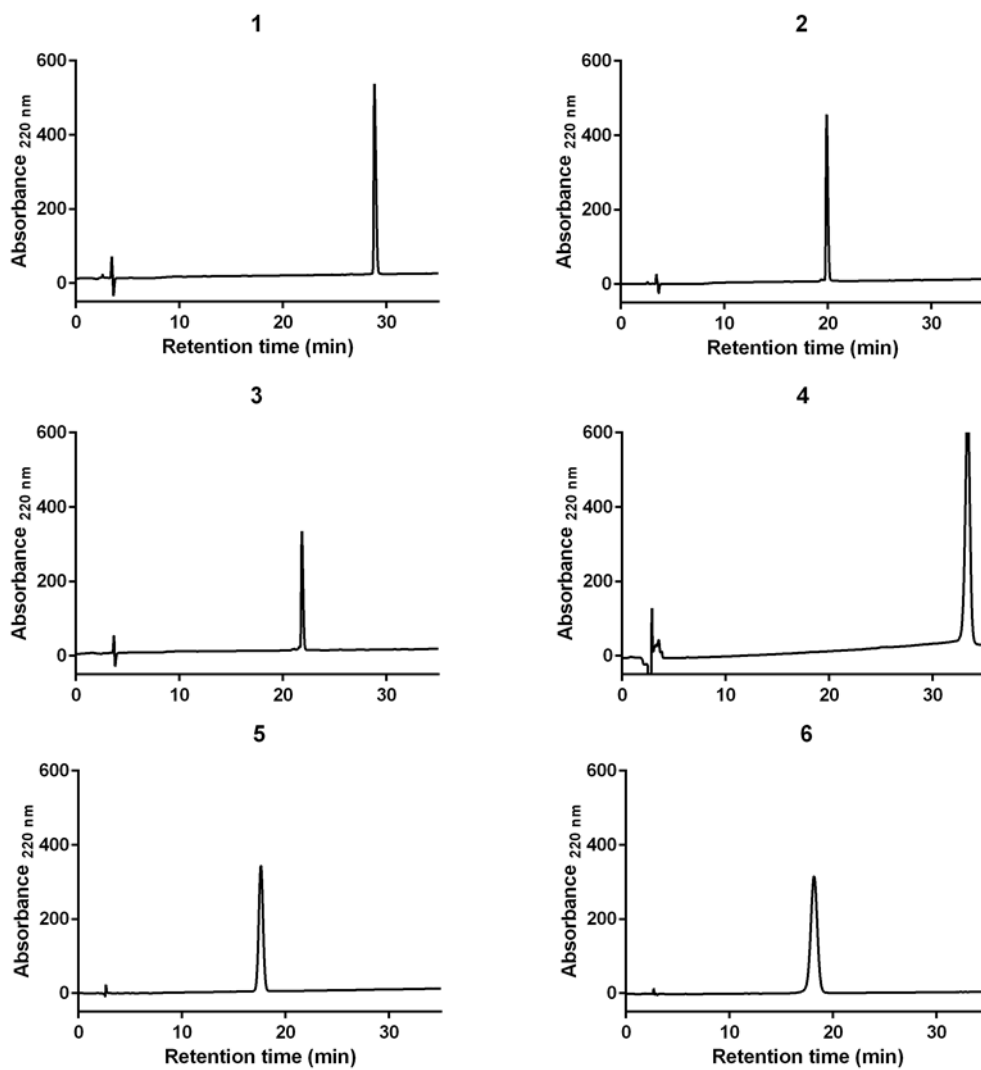
Lastly, the ability to selectively produce multilayer films can be garnered to enhance the magnitude of film response from low piezo coefficient materials. The formation of a multilayer simultaneously increases the signal to noise ratio of the experiments (accuracy) while establishing the relationship between film thickness and the resulting piezo coefficient. This additional tunable parameter garners insight into an additional experimental variable to put back into property prediction of future optimal organic molecular-based materials.

**Appendix A Supplementary Information for the Influence of Molecular Structure on a  
Self-Assembled Monolayer's Piezoresponse**

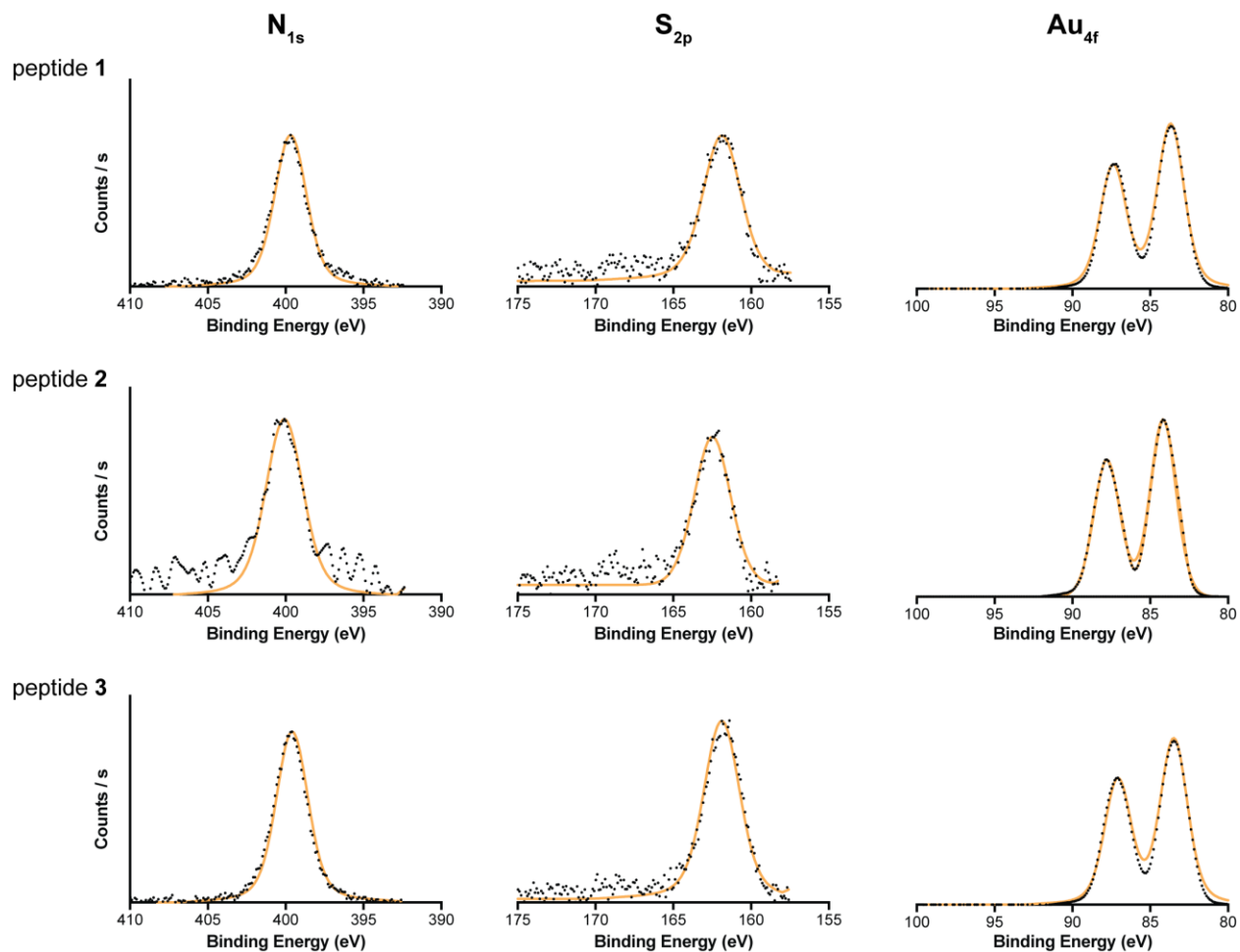
**Appendix Table 1** MALDI-TOF MS data for peptides **1-3** and peptoids **4-6**.

<i>m/z</i> (monoisotopic)		
#	Calculated	Observed
<b>1</b>	1262.7 <sup>a</sup>	1263.7
<b>2</b>	1220.7 <sup>a</sup>	1221.4
<b>3</b>	1178.6 <sup>a</sup>	1179.5
<b>4</b>	1269.6 <sup>b</sup>	1269.5
<b>5</b>	1131.6 <sup>b</sup>	1131.8
<b>6</b>	1039.5 <sup>b</sup>	1039.6

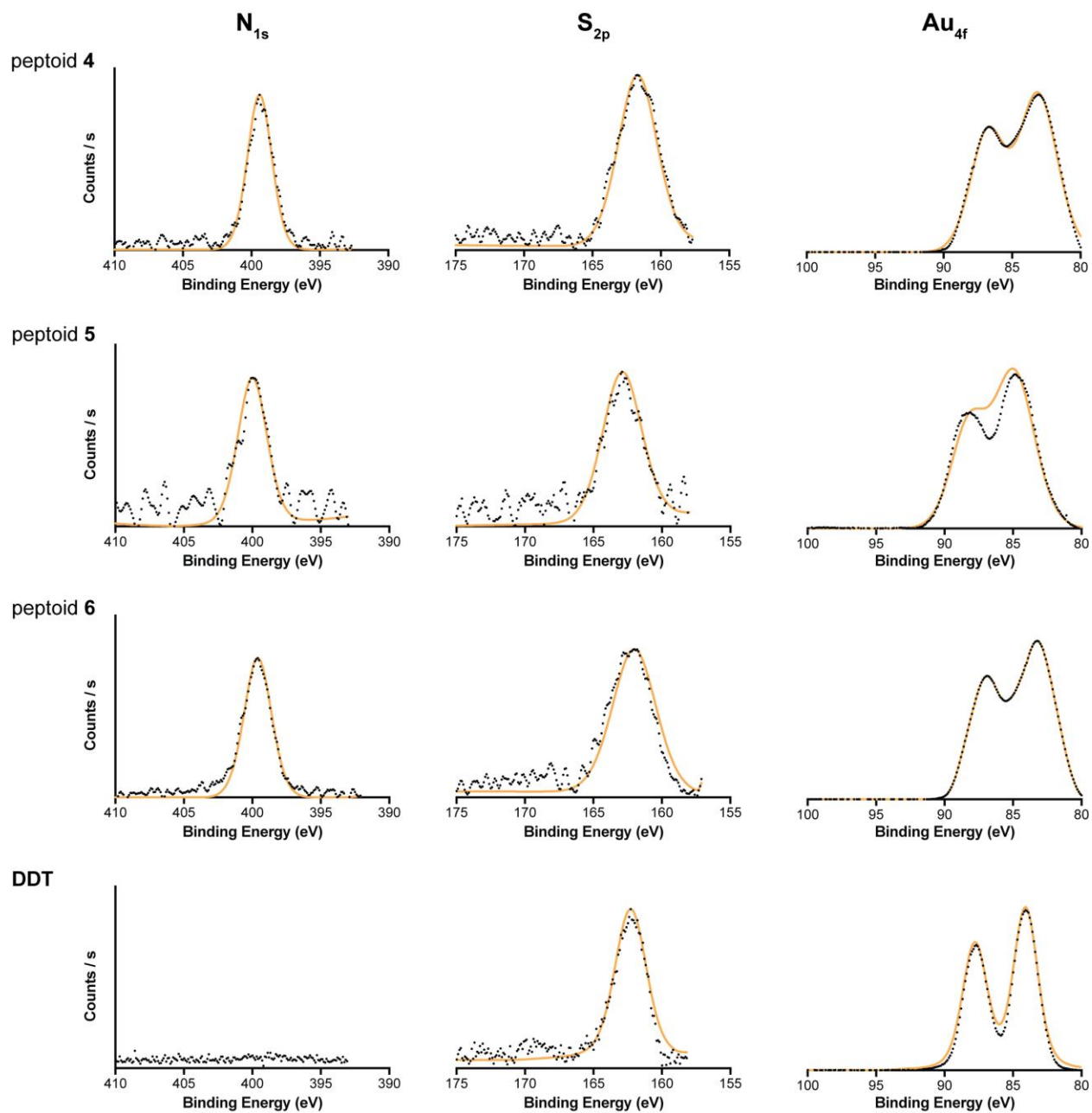
<sup>a</sup> [M+H]<sup>+</sup> ion; <sup>b</sup> [M+Na]<sup>+</sup> ion



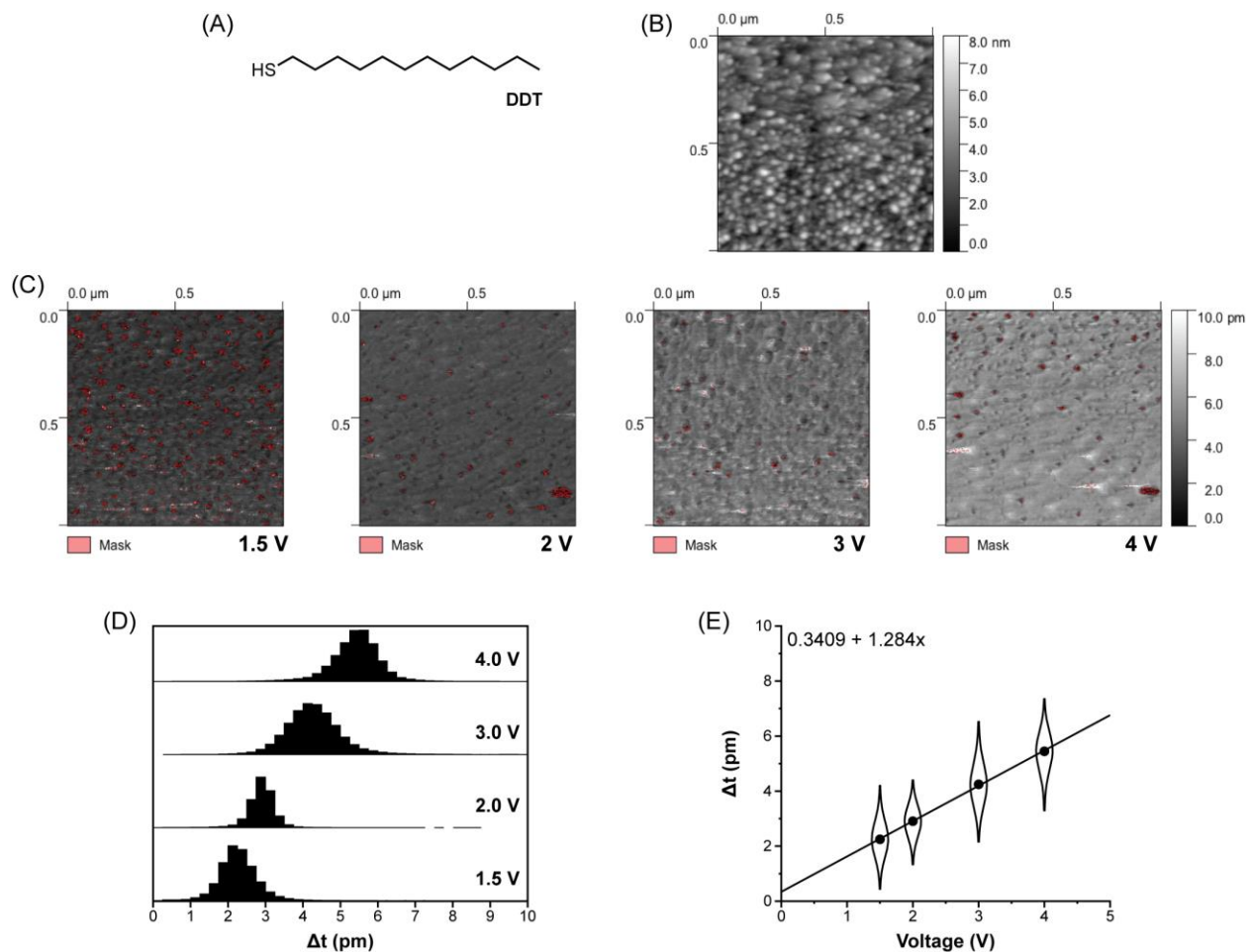
**Appendix Figure 1** Analytical HPLC chromatograms of purified peptides **1-3** and peptoids **4-6**.



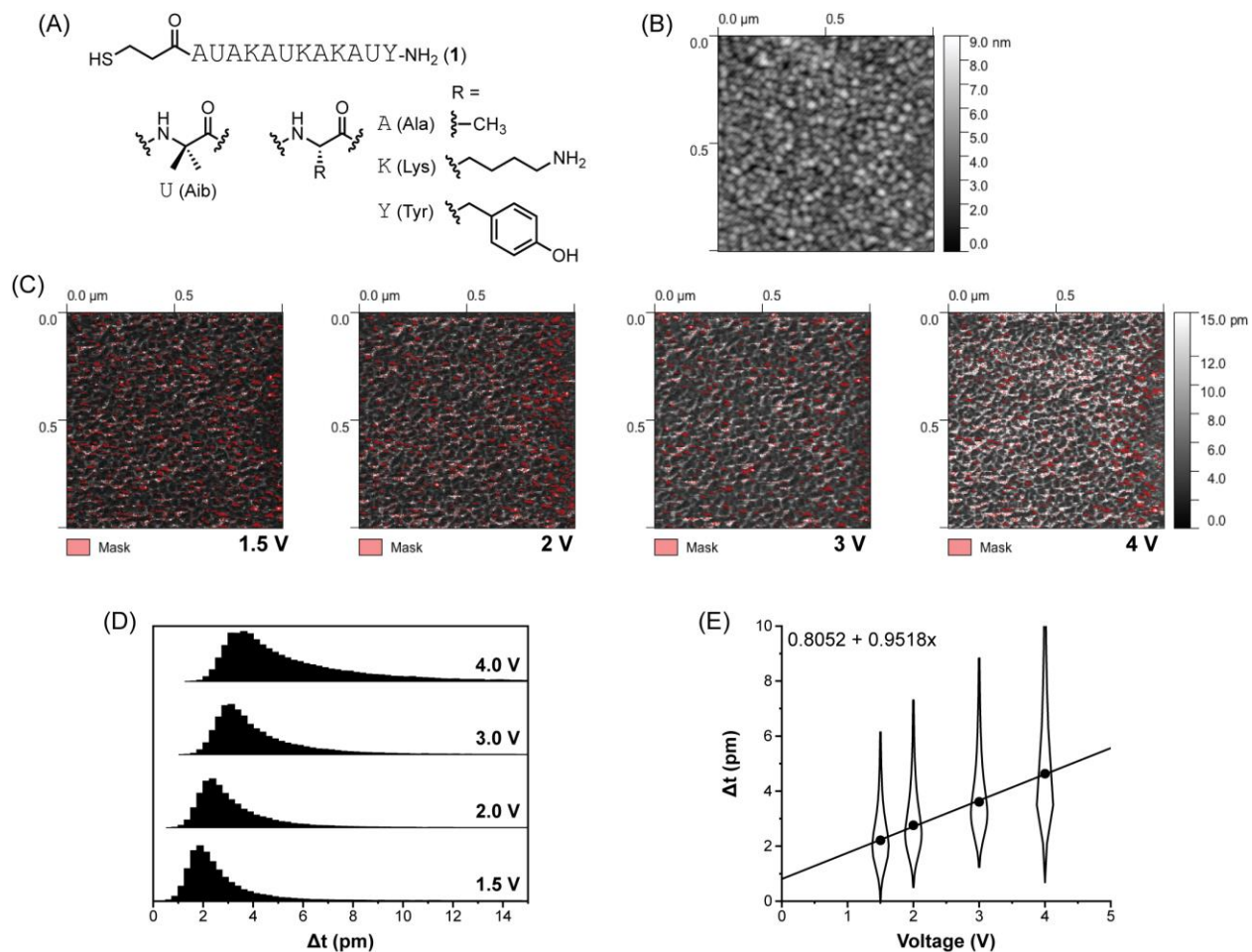
**Appendix Figure 2** Representative  $N_{1s}$ ,  $S_{2p}$ , and  $Au_{4f}$  XPS spectra for peptides **1-3**.



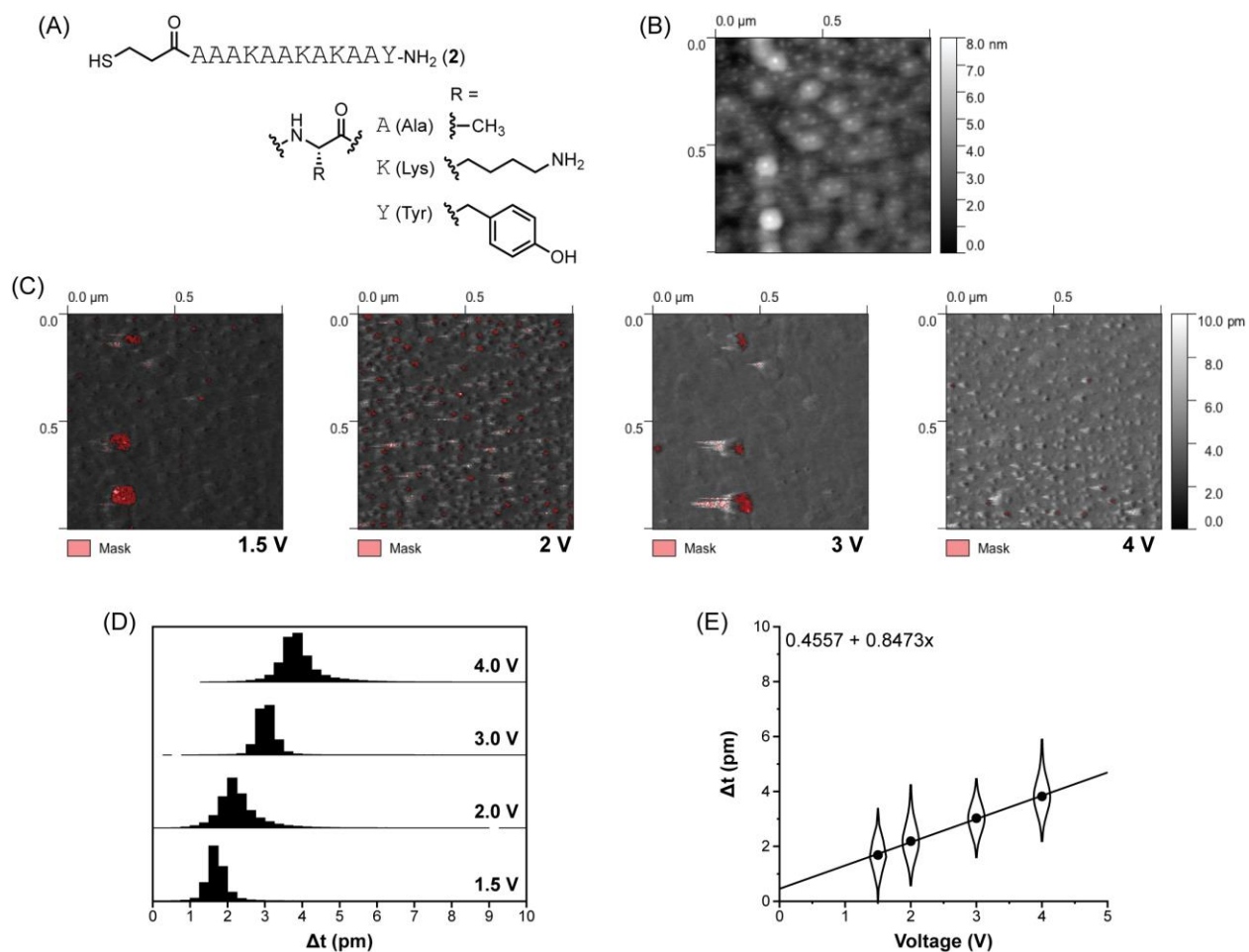
**Appendix Figure 3** Representative  $N_{1s}$ ,  $S_{2p}$ , and  $Au_{4f}$  XPS spectra for peptoids **4-6** and control dodecanethiol (**DDT**).



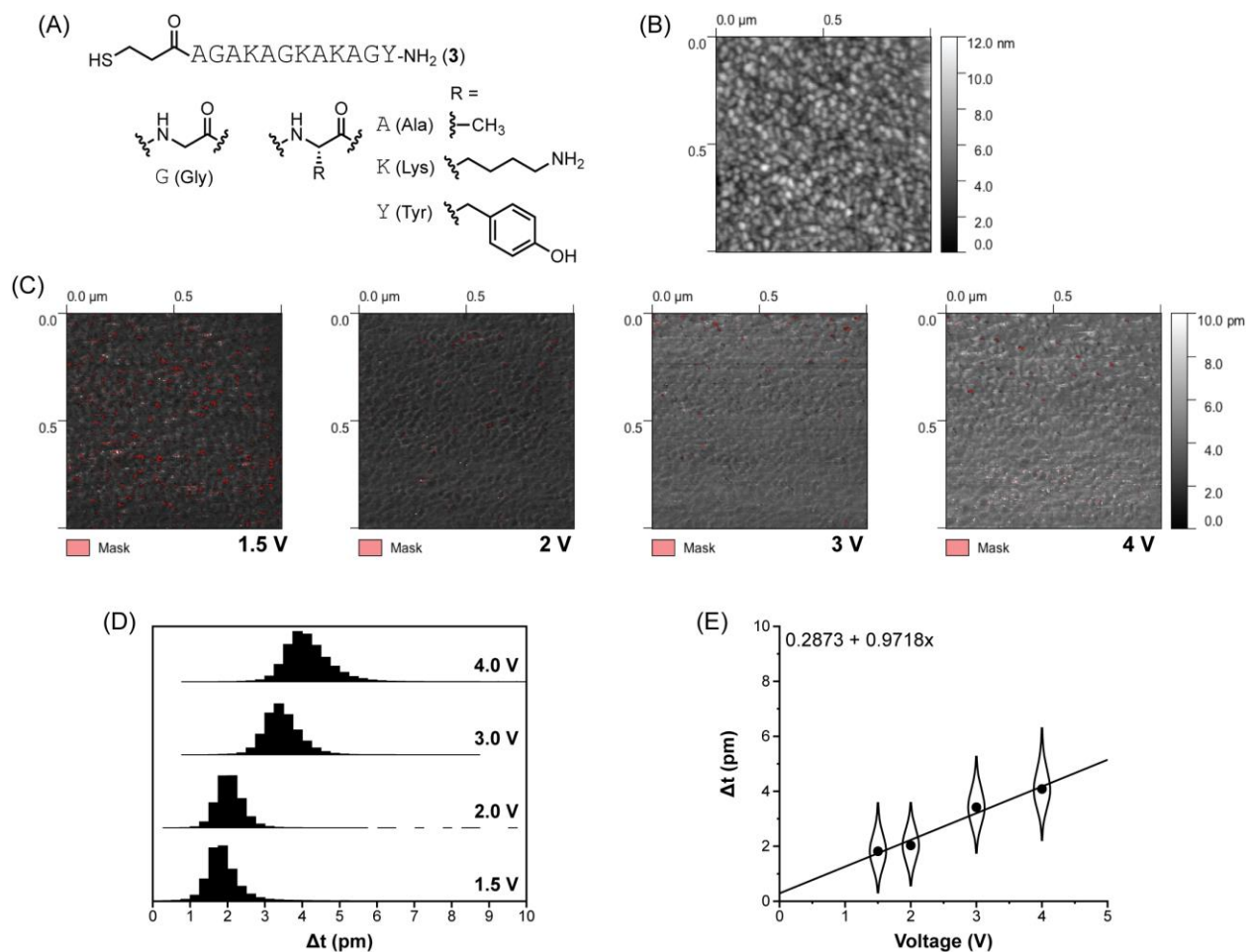
**Appendix Figure 4** Representative raw DART PFM data for analysis of a self-assembled monolayer of **DDT** on gold. (A) Chemical structure of **DDT**. (B) Height image from DART-PFM measurement at an applied voltage of 1.5 V. (C) Images depicting q-corrected DART amplitude ( $\Delta t$ ) at the indicated applied voltage. (D) Histogram analysis of the images shown in panel (C). (E) Linear regression of the histograms in panel (D) vs applied voltage; equation for the best-fit line is shown, in which  $d_{33}$  is the slope.



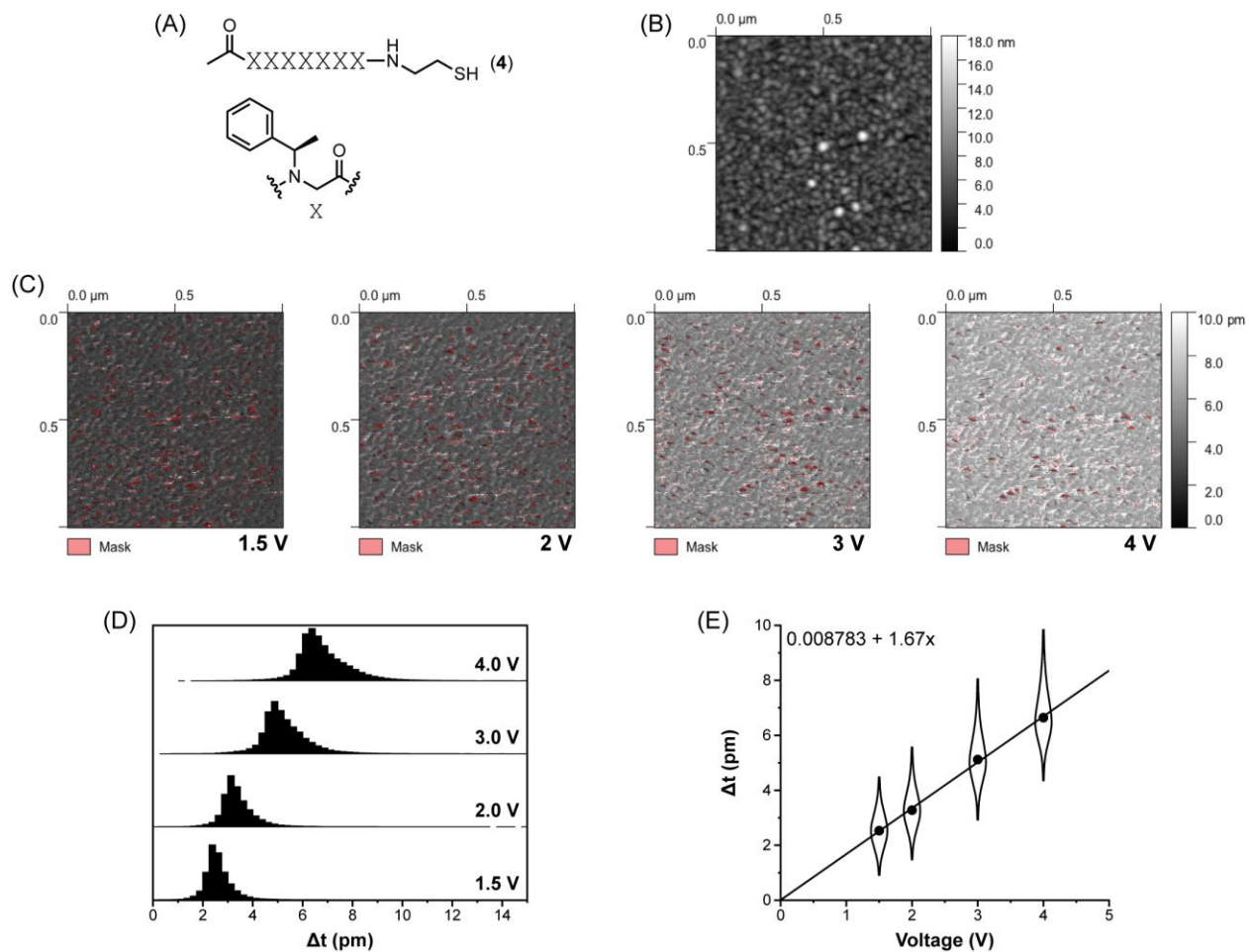
**Appendix Figure 5** Representative raw DART PFM data for analysis of a self-assembled monolayer of peptide **1** on gold. (A) Chemical structure of peptide **1**. (B) Height image from DART-PFM measurement at an applied voltage of 1.5 V. (C) Images depicting q-corrected DART amplitude ( $\Delta t$ ) at the indicated applied voltage. (D) Histogram analysis of the images shown in panel (C). (E) Linear regression of the histograms in panel (D) vs applied voltage; equation for the best-fit line is shown, in which  $d_{33}$  is the slope.



**Appendix Figure 6** Representative raw DART PFM data for analysis of a self-assembled monolayer of peptide **2** on gold. (A) Chemical structure of peptide **2**. (B) Height image from DART-PFM measurement at an applied voltage of 1.5 V. (C) Images depicting q-corrected DART amplitude ( $\Delta t$ ) at the indicated applied voltage. (D) Histogram analysis of the images shown in panel (C). (E) Linear regression of the histograms in panel (D) vs applied voltage; equation for the best-fit line is shown, in which  $d_{33}$  is the slope.

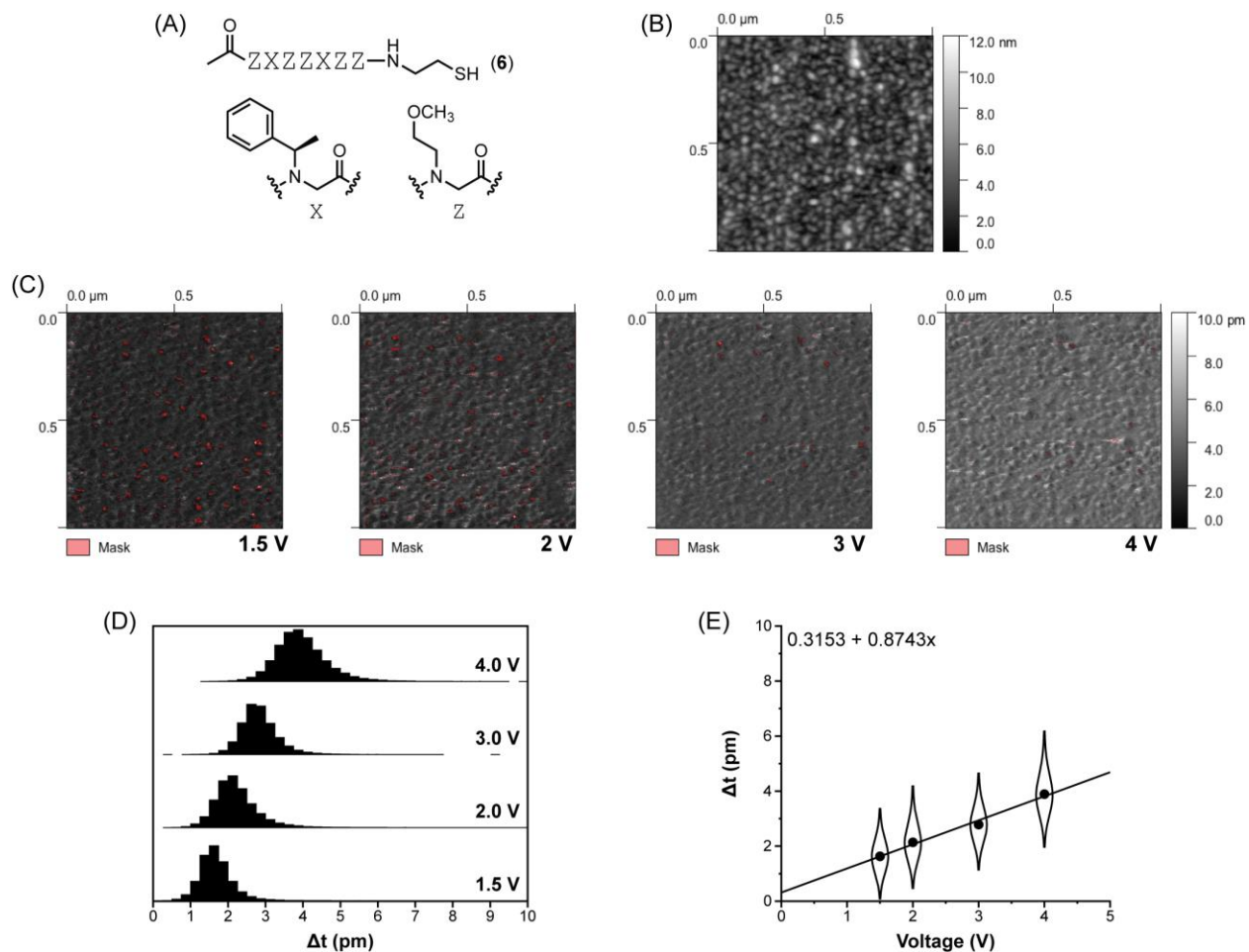


**Appendix Figure 7** Representative raw DART PFM data for analysis of a self-assembled monolayer of peptide **3** on gold. (A) Chemical structure of peptide **3**. (B) Height image from DART-PFM measurement at an applied voltage of 1.5 V. (C) Images depicting q-corrected DART amplitude ( $\Delta t$ ) at the indicated applied voltage. (D) Histogram analysis of the images shown in panel (C). (E) Linear regression of the histograms in panel (D) vs applied voltage; equation for the best-fit line is shown, in which  $d_{33}$  is the slope.



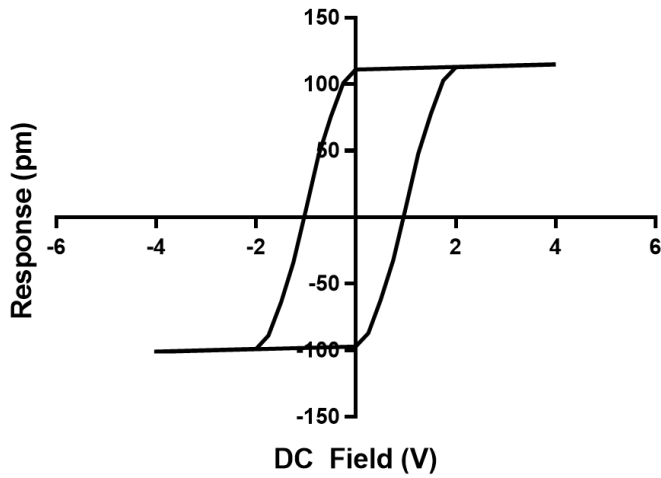
**Appendix Figure 8** Representative raw DART PFM data for analysis of a self-assembled monolayer of peptoid **4** on gold. (A) Chemical structure of peptoid **4**. (B) Height image from DART-PFM measurement at an applied voltage of 1.5 V. (C) Images depicting q-corrected DART amplitude ( $\Delta t$ ) at the indicated applied voltage. (D) Histogram analysis of the images shown in panel (C). (E) Linear regression of the histograms in panel (D) vs applied voltage; equation for the best-fit line is shown, in which  $d_{33}$  is the slope.



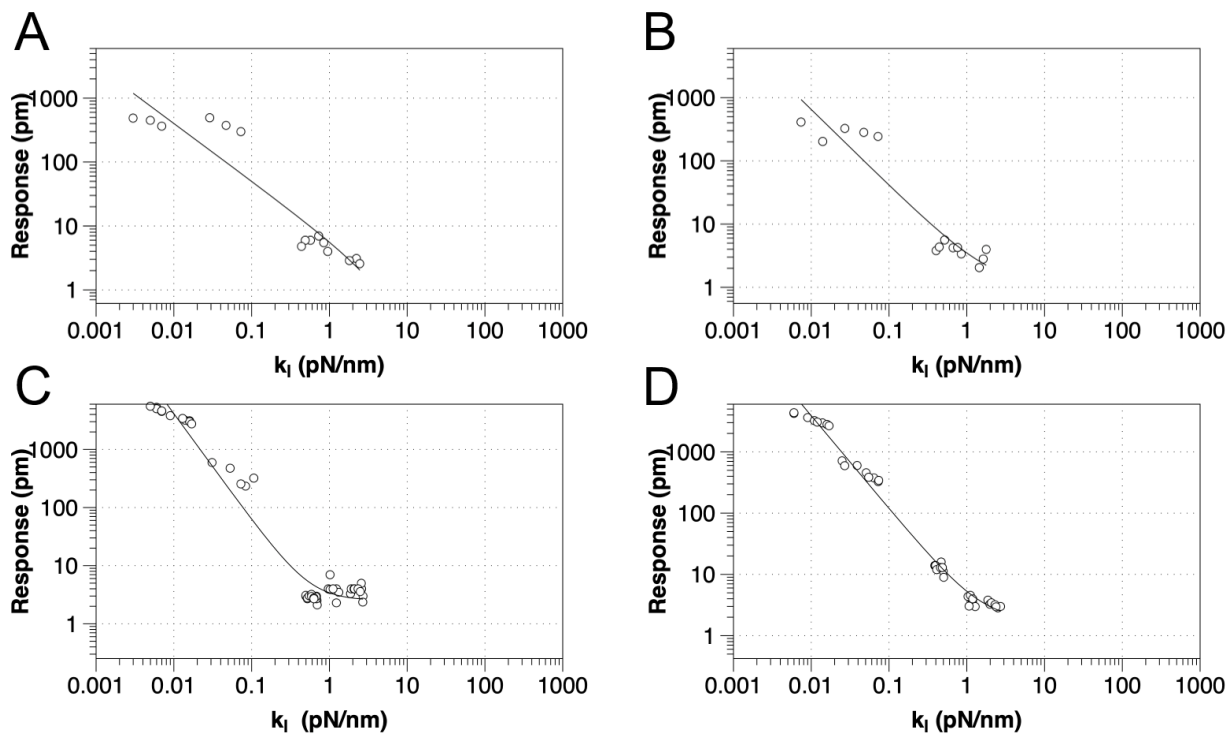


**Appendix Figure 10** Representative raw DART PFM data for analysis of a self-assembled monolayer of peptoid **6** on gold. (A) Chemical structure of peptoid **6**. (B) Height image from DART-PFM measurement at an applied voltage of 1.5 V. (C) Images depicting q-corrected DART amplitude ( $\Delta t$ ) at the indicated applied voltage. (D) Histogram analysis of the images shown in panel (C). (E) Linear regression of the histograms in panel (D) vs applied voltage; equation for the best-fit line is shown, in which  $d_{33}$  is the slope.

**Appendix B Supplementary Information for the Optimization of Nanoscale  
Electromechanical Coupling Evaluation Methods**



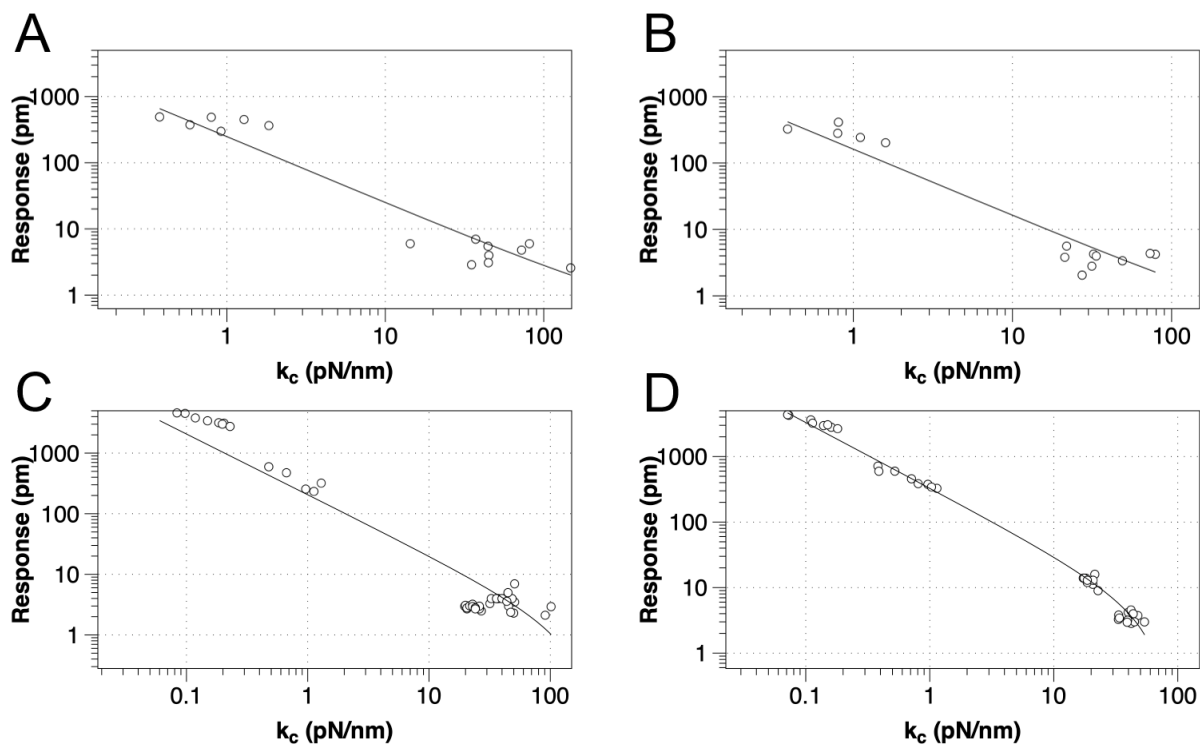
**Appendix Figure 11** Suggested  $V_{DC}$  sweep technique on non-fixed polar piezoelectric materials in which the remnant polarization switches under the coercive field.



**Appendix Figure 12** Relationship between tip response and  $k_1$  for various SAMs using AFM levers with spring constants from 0.02-2.8 N/m, for (a) **DDT**, (b) **MUA**, (c) peptide **A** and (d) peptoid **B** respectively. The best-fit line is to  $y = a + bx^c$ .

**Appendix Table 2** Summary of tip-dependent ( $k_1$ ) response across four organic self-assembled monolayers, indicating best-fit parameters of tip response to  $a + bx^c$ .

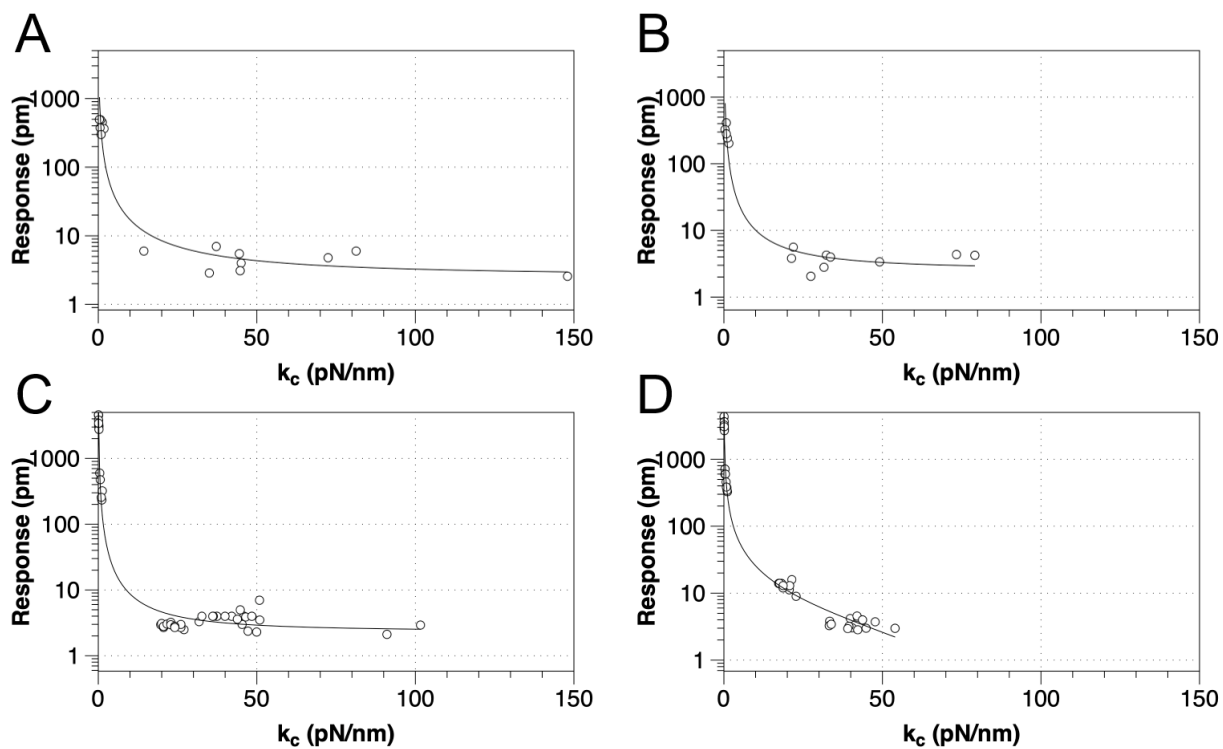
Material	Constant (a)	Coefficient (b)	Power (c)	R <sup>2</sup>
<b>DDT</b>	-0.786	6.35	-0.901	0.886
<b>MUA</b>	0.973	2.52	-1.21	0.903
<b>Peptide A</b>	2.51	0.899	-1.83	0.965
<b>Peptoid B</b>	1.73	3.57	-1.52	0.988



**Appendix Figure 13** Relationship between tip response and  $k_c$  for various SAMs using AFM levers with spring constants from 0.02-2.8 N/m, for (a) **DDT**, (b) **MUA**, (c) peptide **A** and (d) peptoid **B** respectively. The best-fit line is to  $y = a + bx^{-1}$ .

**Appendix Table 3** Summary of tip-dependent ( $k_c$ ) response across four organic self-assembled monolayers, indicating best-fit parameters of tip response to  $a + bx^{-1}$ .

Material	Constant (a)	Coefficient (b)	$R^2$
<b>DDT</b>	0.342	247	0.932
<b>MUA</b>	0.239	162	0.927
<b>Peptide A</b>	-1.02	207	0.944
<b>Peptoid B</b>	-4.24	331	0.992



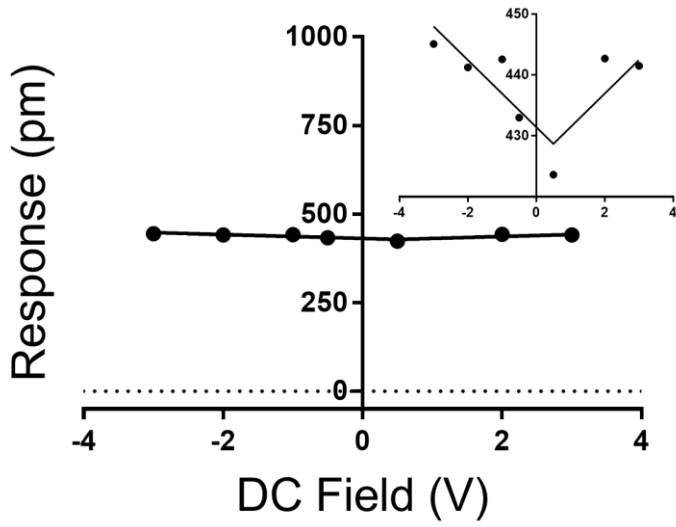
**Appendix Figure 14** Relationship between tip response and  $k_c$  for various SAMs using AFM levers with spring constants from 0.02-2.8 N/m, for (a) **DDT**, (b) **MUA**, (c) peptide **A** and (d) peptoid **B** respectively. The best-fit line is to  $y = a + bx^c$ . A replotting of Figure 2 from the main text but in log linear scaling to emphasize the asymptotic nature of the fits.

**Appendix Table 4** AMFM results for the measurement of  $k_c$  with corresponding  $k_l$  based on implemented lever.

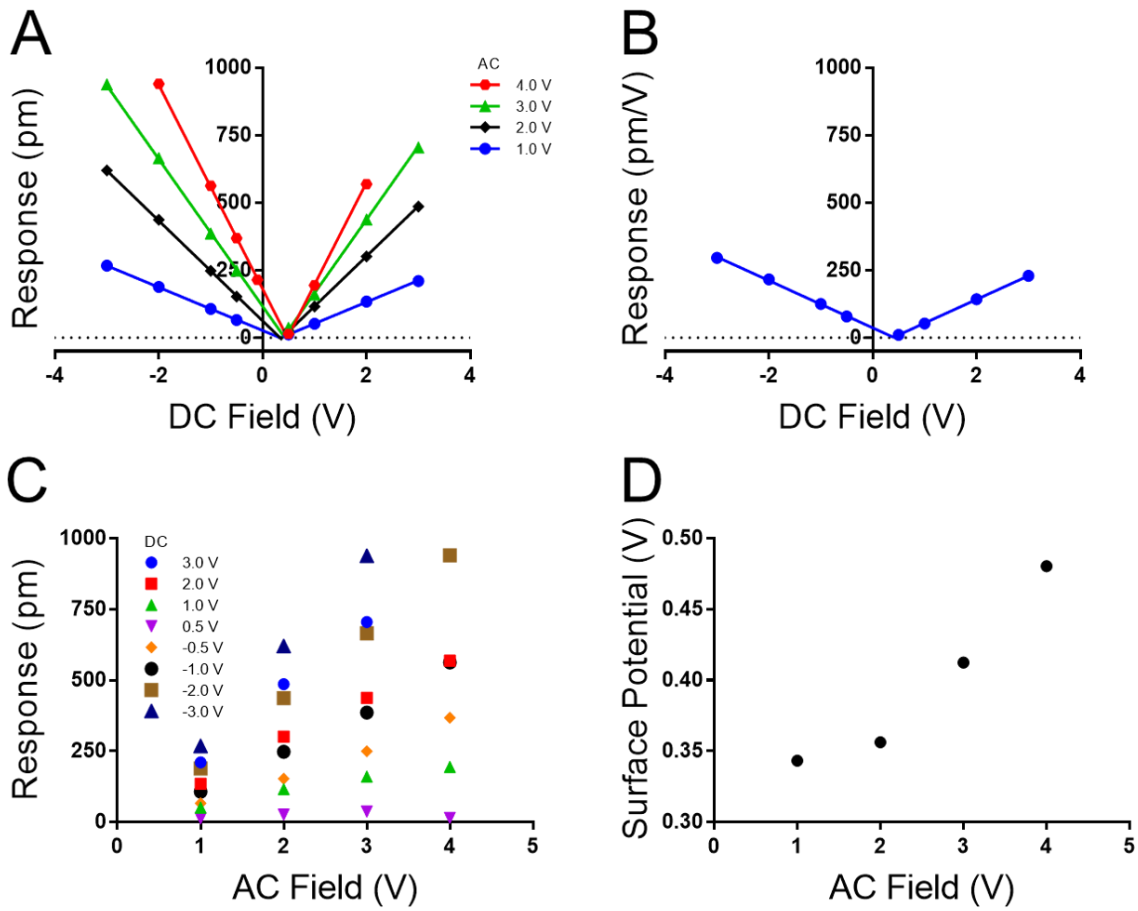
<b>Material</b>	<b>Lever <math>k_l</math> (N/m)</b>	<b><math>k_l</math> (<math>\mu\text{N/m}</math>)</b>	<b><math>k^*</math> (<math>\mu\text{N/m}</math>)</b>	<b><math>k^*</math> Error (<math>\mu\text{N/m}</math>)</b>
<b>QCM</b>	2.8	$1.66 \times 10^6$	1684	165
	0.09	$4.41 \times 10^4$	132.9	54.1
<b>DDT</b>	2.8	$1.69 \times 10^6$	1937	162
	0.09	$3.69 \times 10^4$	131.3	35.0
<b>MUA</b>	2.8	$1.66 \times 10^6$	1272	197
	0.09	$3.51 \times 10^4$	103.5	35.8
<b>Peptide A</b>	2.8	$1.68 \times 10^6$	1174	158
	0.09	$3.59 \times 10^4$	26.77	8.13
<b>Peptoid B</b>	2.8	$1.73 \times 10^6$	1244	140
	0.09	$3.41 \times 10^4$	65.10	26.4

**Appendix Table 5** Coefficient values and calculated  $d_{33}$  from tip response as a function of  $V_{AC}$  on peptoid **B** using 0.09 N/m  $k_l$  levers at varying  $V_{DC}$ .

<b><math>V_{DC}</math> (V)</b>	<b><math>R^2</math></b>	<b>Intercept (pm)</b>	<b><math>d_{eff}</math> (pm/V)</b>
3.0	0.998	7.19	241
2.0	0.995	13.9	148
1.0	0.956	22.8	50.6
-1.0	0.991	-32.6	137
-2.0	0.996	-35.7	229
-3.0	0.999	-38.0	325



**Appendix Figure 15** PFM tip response from  $V_{DC}$  sweep technique on **PZT** at 3.0  $V_{AC}$  with R2 levers (2.8 N/m). The resulting slope of the fit was 5.51 pm/ $V_{DC}$  with an  $R^2$  value of 0.704. With a calculated  $d_{eff}$  of 143 pm/ $V_{AC}$ .



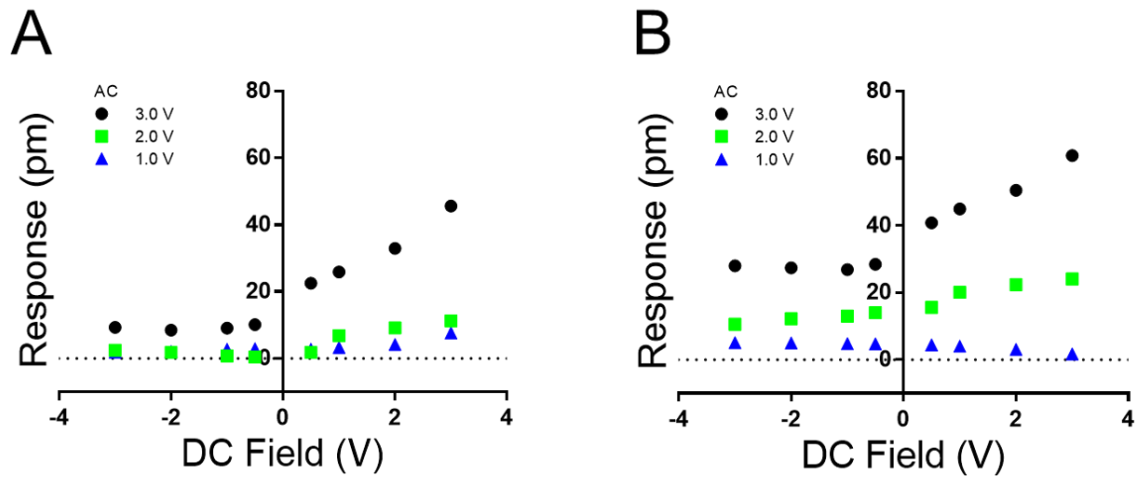
**Appendix Figure 16** (a) PFM tip response from  $V_{DC}$  sweep technique on **ZNO** with TRS levers (0.09 N/m) at varying  $V_{AC}$ . (b) DC- dependent response. (c) PFM response from  $V_{AC}$  at indicated  $V_{DC}$ . (d) Measure  $V_{CPD}$  as a function of  $V_{AC}$ .

**Appendix Table 6** Coefficient values and calculated  $d_{33}$  from tip response as a function of  $V_{DC}$  on ZNO using 0.09 N/m  $k_l$  levers at varying  $V_{AC}$ .

$V_{AC}$ (V)	$V_{CPD}$ (V)	Slope (A)	$R^2$	$d_{eff}$ (pm/V)
4.0	0.480	278	0.999	0.040
3.0	0.412	185	0.999	1.61
2.0	0.356	86.0	0.996	-1.54
1.0	0.343	43.9	0.999	-0.291
NA	0.401	87.5	0.999	1.90

**Appendix Table 7** Coefficient values and calculated  $d_{33}$  from tip response as a function of  $V_{AC}$  on ZNO using 0.09 N/m  $k_l$  levers at varying  $V_{DC}$ .

$V_{DC}$ (V)	$R^2$	Intercept (pm)	$d_{eff}$ (pm/V)
3.0	0.996	-27.5	247
2.0	0.997	0.675	144
1.0	0.980	12.2	47.3
0.5	0.996	0.740	12.3
-0.5	0.995	-41.9	100
-1.0	0.997	-50.3	151
-2.0	0.999	-62.7	248
-3.0	0.999	-62.8	336

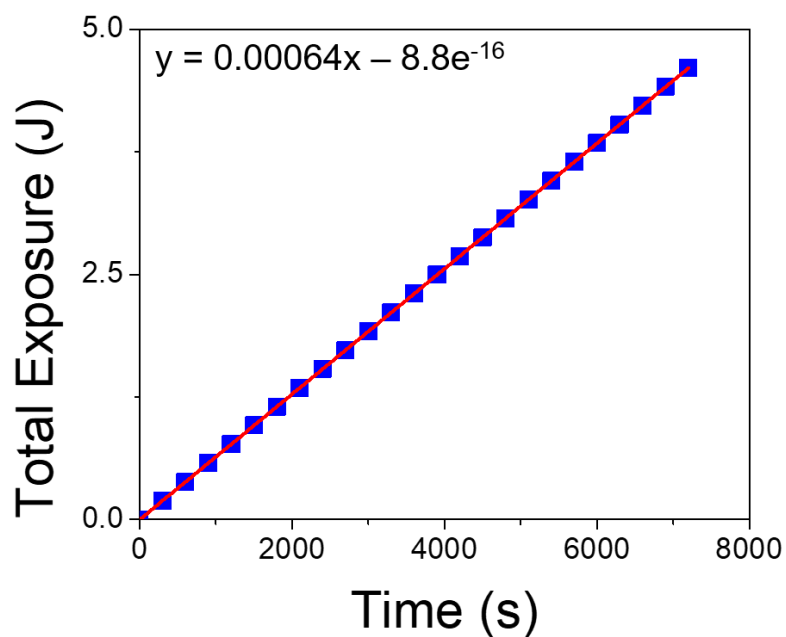


**Appendix Figure 17** PFM tip response from  $V_{DC}$  sweep technique on PPLN at various  $V_{AC}$  using R2 levers (2.8 N/m). (a) and (b) represent measured response of PPLN with phase up (+180°) and phase down (-180°) respectively.

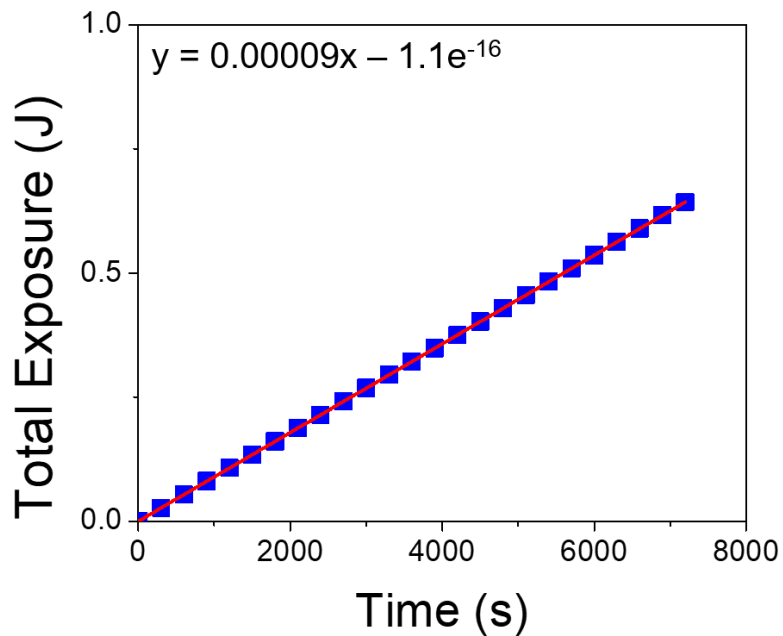
**Appendix Table 8** SKPFM results for the measurement of  $V_{CPD}$  for various materials using 2.8 N/m levers.

Material	$V_{CPD}$ (mV)	Error (mV)
DDT	172	5.95
MUA	-198	19.6
Peptide A	-139	16.2
Peptoid B	-362	23.6
QCM	1100	161
ZnO	-745	160

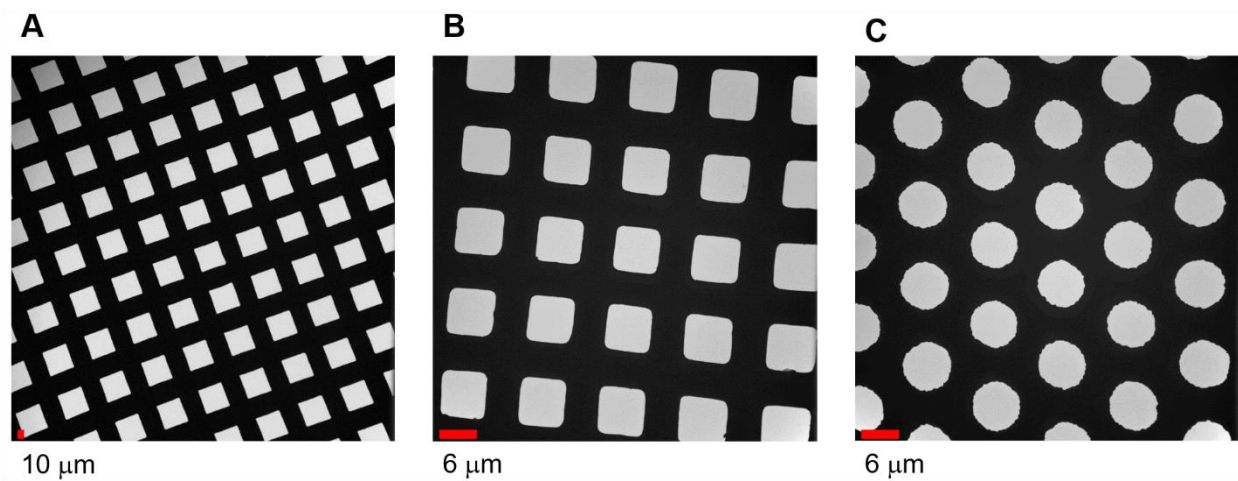
**Appendix C Supplementary Information for the Lab Scale Manipulation of Single and Multilayer Organic Self Assembled Structures**



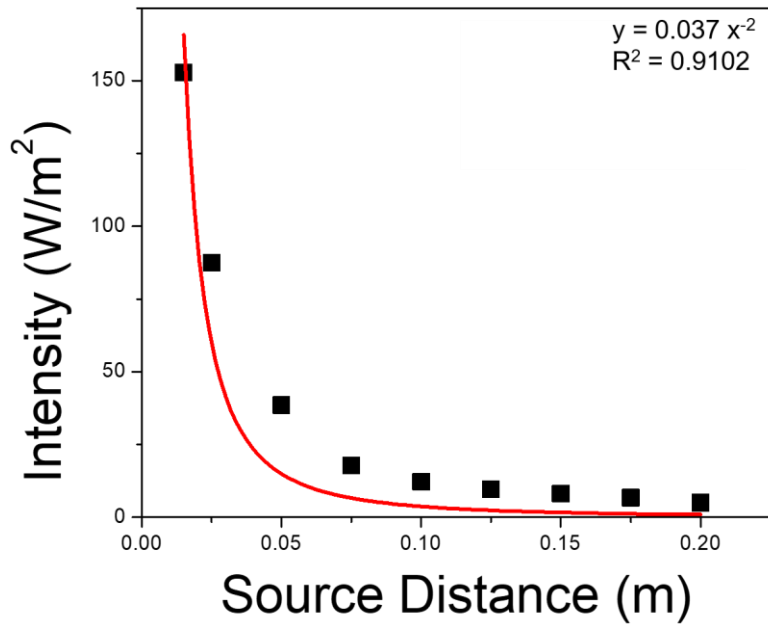
**Appendix Figure 18** Calibration curve for the total energy exposure to a sample surface with a source-sample distance of 2.5 cm from a 175 W source for a given period.



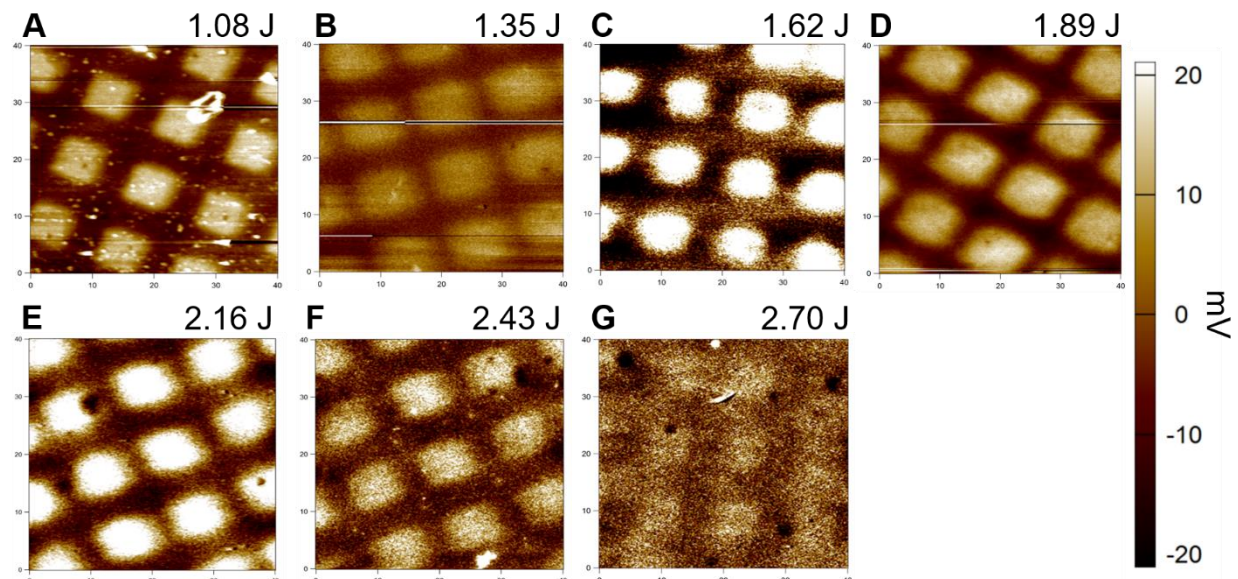
**Appendix Figure 19** Calibration curve for the total energy exposure to a sample surface with a source-sample distance of 10.0 cm from a 175 W source for a given period.



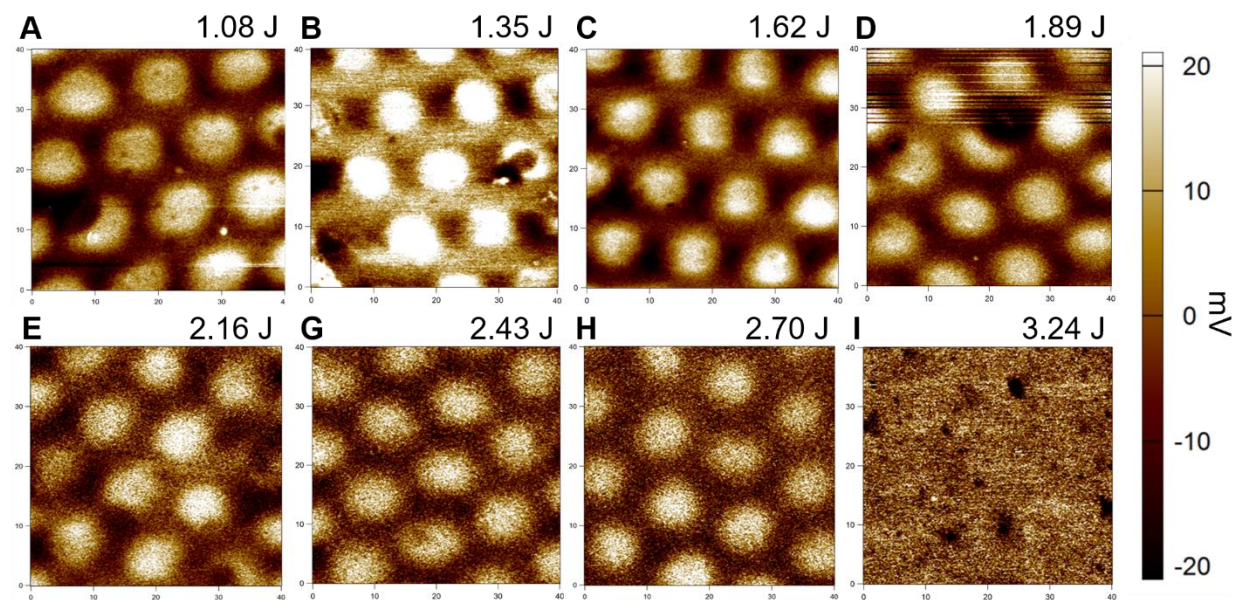
**Appendix Figure 20** TEM images of three mesh type TEM grids used as photomasks (a) 400 square mesh, (b) 2000 square mesh, and (c) 2000 circular mesh.



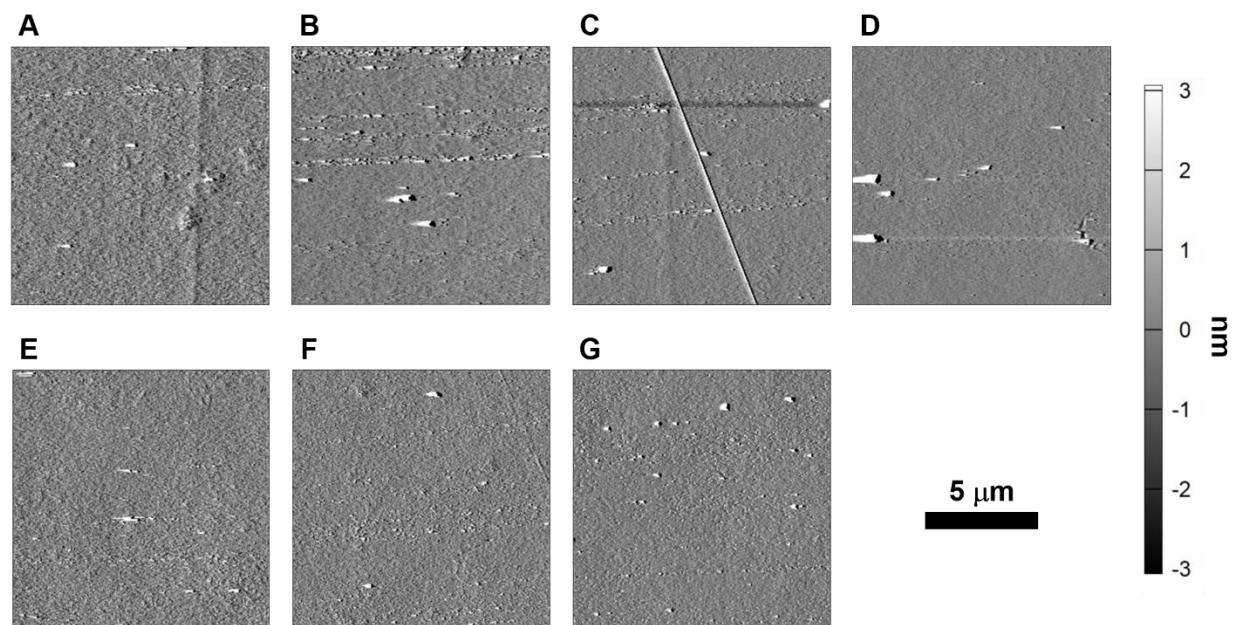
**Appendix Figure 21** Rate of change in the incident intensity over a change in source-sample distance for a 175 W metal halide light source measured at  $\lambda = 380$  nm fitted to a fixed exponent of -2.



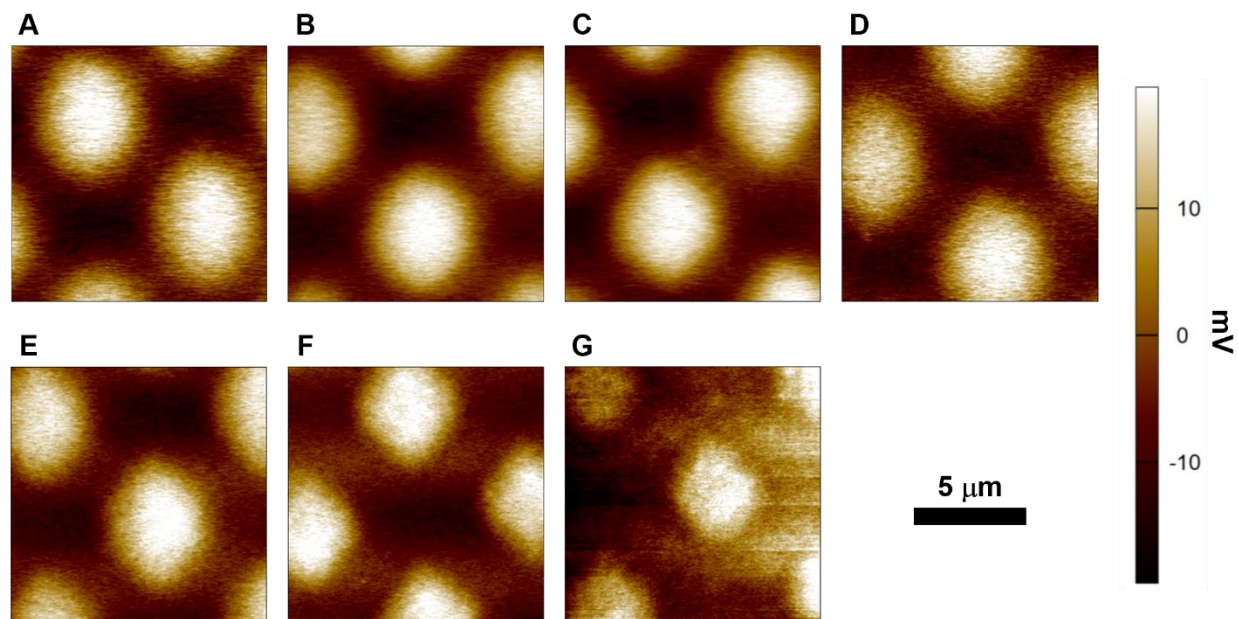
**Appendix Figure 22** SKPFM surface potential ( $V_{CPD}$ ) images of a MUA SAM patterned and backfilled with DDT using a 2000 square mesh TEM grid as the photomask.



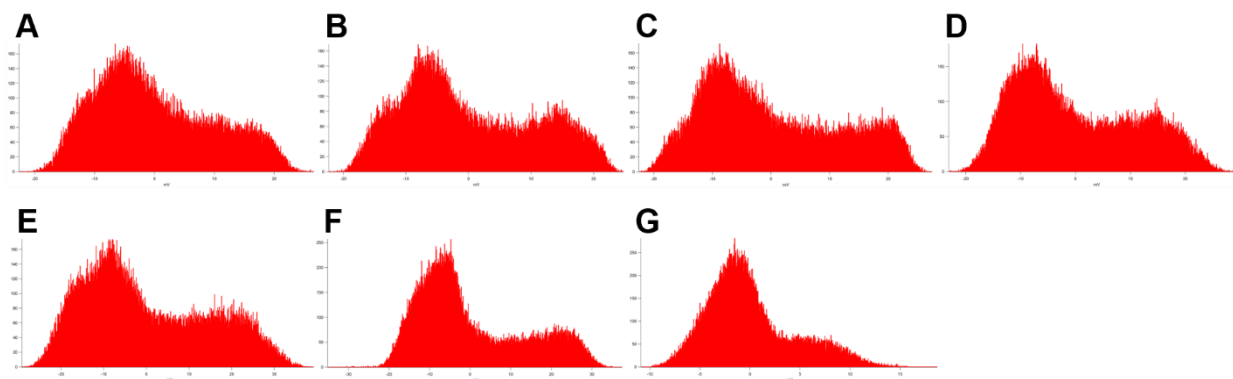
**Appendix Figure 23** SKPFM surface potential ( $V_{CPD}$ ) images of a MUA SAM patterned and backfilled with DDT using a 2000 circular mesh TEM grid as the photomask.



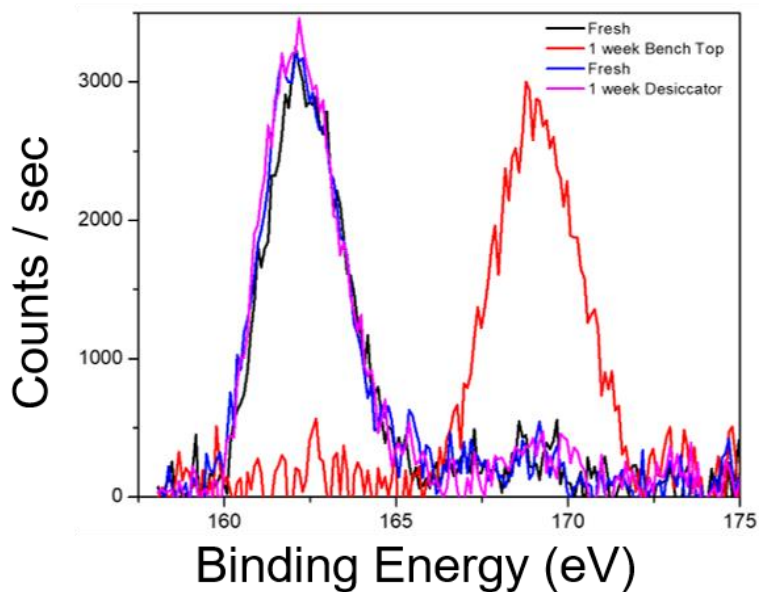
**Appendix Figure 24** SKPFM amplitude scans of a **MHDA** SAM patterned and backfilled with **DDT** using a 2000 square mesh TEM grid as the photomask as a factor of sample age with (a) 1 day, (b) 7 days, (c) 30 days, (d) 57 days, (e) 91 days, (f) 127 days, and (g) 171 days.



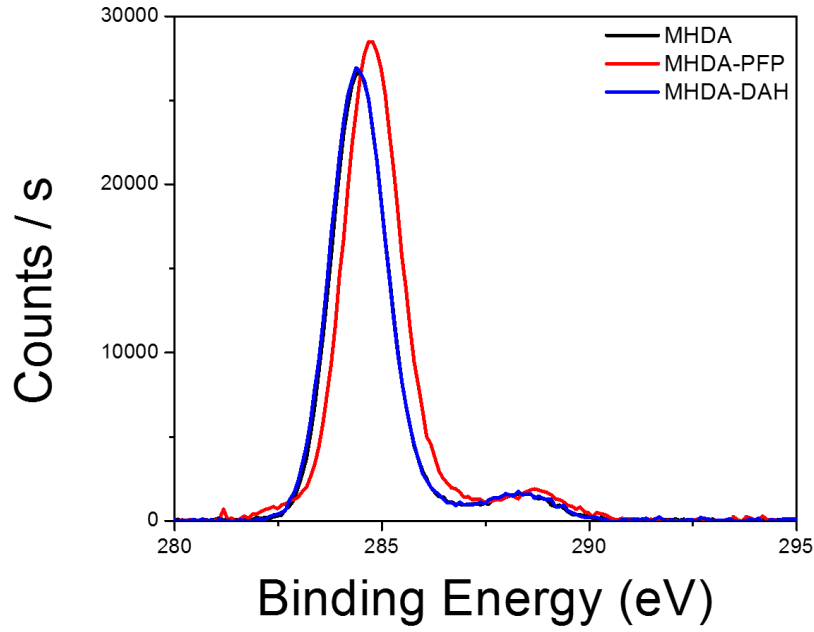
**Appendix Figure 25** SKPFM surface potential ( $V_{\text{CPD}}$ ) scans of a **MHDA** SAM patterned and backfilled with **DDT** using a 2000 square mesh TEM grid as the photomask as a factor of sample age with (a) 1 day, (b) 7 days, (c) 30 days, (d) 57 days, (e) 91 days, (f) 127 days, and (g) 171 days.



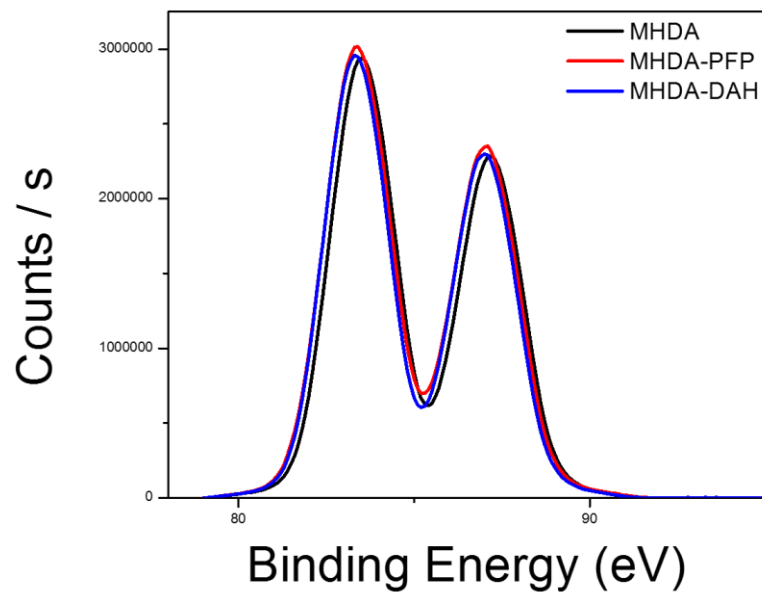
**Appendix Figure 26** SKPFM surface potential ( $V_{\text{CPD}}$ ) histograms of a **MHDA** SAM patterned and backfilled with **DDT** using a 2000 square mesh TEM grid as the photomask as a factor of sample age with (a) 1 day, (b) 7 days, (c) 30 days, (d) 57 days, (e) 91 days, (f) 127 days, and (g) 171 days.



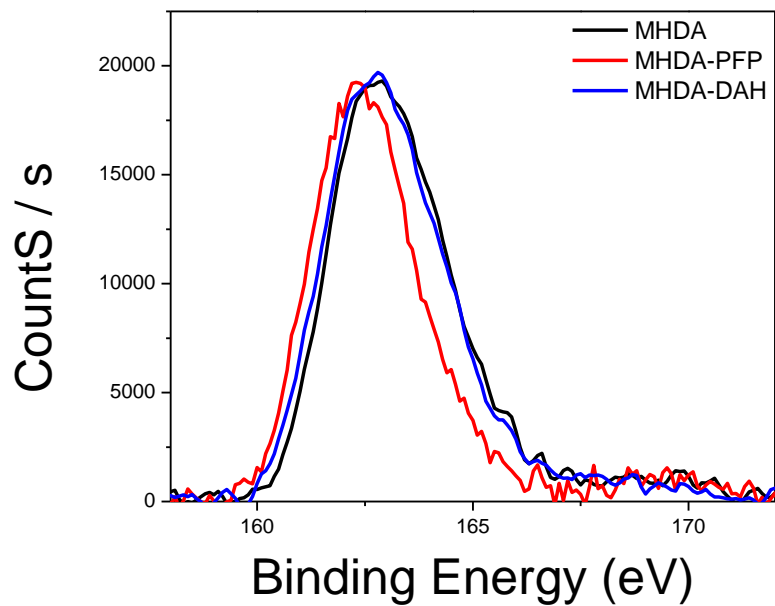
**Appendix Figure 27** XPS S<sub>2p</sub> spectrum for monitoring the oxidation of S in an Au-thiol SAM of DDT. The black trace relates to a freshly prepared DDT SAM, and the red track is the same SAM after one week of exposure to ambient conditions. The blue trace represents a freshly prepared DDT SAM with the pink trace correlating to the same SAM after one week in an evacuated desiccator shielded in an Al foil wrapped Petri dish.



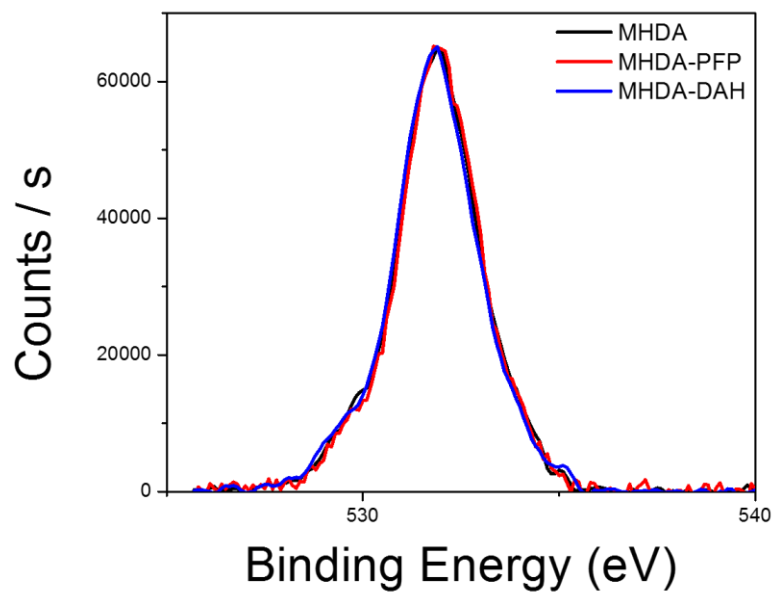
**Appendix Figure 28** C<sub>1s</sub> lines for multilayer confirmation by XPS.



**Appendix Figure 29** Au<sub>4f</sub> lines for multilayer confirmation by XPS.



**Appendix Figure 30** S<sub>2p</sub> lines for multilayer confirmation by XPS.



**Appendix Figure 31** O<sub>1s</sub> lines for multilayer confirmation by XPS.

## Bibliography

### B.1 Chapter 1 (Introduction)

1. Cheong, L. Z.; Zhao, W.; Song, S.; Shen, C., Lab on a tip: Applications of functional atomic force microscopy for the study of electrical properties in biology. *Acta Biomater* **2019**, *99*, 33-52.
2. Fridkin, V.; Ducharme, S., *Ferroelectricity at the Nanoscale*. 2014.
3. Guerin, S.; O'Donnell, J.; Haq, E. U.; McKeown, C.; Silien, C.; Rhen, F. M. F.; Soulimane, T.; Tofail, S. A. M.; Thompson, D., Racemic Amino Acid Piezoelectric Transducer. *Phys Rev Lett* **2019**, *122* (4), 047701.
4. Guerin, S.; Tofail, S. A. M.; Thompson, D., Organic piezoelectric materials: milestones and potential. *Npg Asia Materials* **2019**, *11* (1).
5. Kim, D.; Han, S. A.; Kim, J. H.; Lee, J. H.; Kim, S. W.; Lee, S. W., Biomolecular Piezoelectric Materials: From Amino Acids to Living Tissues. *Adv Mater* **2020**, e1906989.
6. Vasudevan, R. K.; Balke, N.; Maksymovych, P.; Jesse, S.; Kalinin, S. V., Ferroelectric or non-ferroelectric: Why so many materials exhibit “ferroelectricity” on the nanoscale. *Applied Physics Reviews* **2017**, *4* (2).
7. Chae, I.; Jeong, C. K.; Ounaies, Z.; Kim, S. H., Review on Electromechanical Coupling Properties of Biomaterials. *ACS Applied Bio Materials* **2018**, *1* (4), 936-953.
8. DAMJANOVIC, D.; NEWNHAM, R. E., Electrostrictive and Piezoelectric Materials for Actuator Applications. *J. of INTELL. MATER. SYST. AND STRUCT.* **1992**, *3*, 28.
9. Eckermann, A. L.; Feld, D. J.; Shaw, J. A.; Meade, T. J., Electrochemistry of redox-active self-assembled monolayers. *Coord Chem Rev* **2010**, *254* (15-16), 1769-1802.
10. Ursic, H.; Prah, U., Investigations of ferroelectric polycrystalline bulks and thick films using piezoresponse force microscopy. *Proc Math Phys Eng Sci* **2019**, *475* (2223), 20180782.
11. Miller, N. C.; Grimm, H. M.; Horne, W. S.; Hutchison, G. R., Accurate electromechanical characterization of soft molecular monolayers using piezo force microscopy. *Nanoscale Advances* **2019**, *1* (12), 4834-4843.
12. Voigtländer, B., *Atomic Force Microscopy*. 2019.
13. Quan, X.; Madura, J. D.; Hutchison, G. R. Self-Assembled Monolayer Piezoelectrics: Electric-Field Driven Conformational Changes **2017**.

14. Quan, X. F.; Marvin, C. W.; Seebald, L.; Hutchison, G. R., Single-Molecule Piezoelectric Deformation: Rational Design from First-Principles Calculations. *Journal of Physical Chemistry C* **2013**, *117* (33), 16783-16790.
15. Love, J. C.; Estroff, L. A.; Kriebel, J. K.; Nuzzo, R. G.; Whitesides, G. M., Self-assembled monolayers of thiolates on metals as a form of nanotechnology. *Chem Rev* **2005**, *105* (4), 1103-1169.
16. Ulman, A., Formation and Structure of Self-Assembled Monolayers. *Chem Rev* **1996**, *96* (4), 1533-1554.
17. White, S. J.; Johnson, S. D.; Sellick, M. A.; Bronowska, A.; Stockley, P. G.; Walti, C., The influence of two-dimensional organization on peptide conformation. *Angew Chem Int Ed Engl* **2015**, *54* (3), 974-8.
18. Rodriguez, B. J.; Callahan, C.; Kalinin, S. V.; Proksch, R., Dual-frequency resonance-tracking atomic force microscopy. *Nanotechnology* **2007**, *18* (47).
19. Jesse, S.; Lee, H. N.; Kalinin, S. V., Quantitative mapping of switching behavior in piezoresponse force microscopy. *Review of Scientific Instruments* **2006**, *77* (7).
20. Hofmann, S., *Auger- and X-Ray Photoelectron Spectroscopy in Materials Science*. 2013.
21. Lu, H.; Hood, M. A.; Mauri, S.; Baio, J. E.; Bonn, M.; Munoz-Espi, R.; Weidner, T., Biomimetic vaterite formation at surfaces structurally templated by oligo(glutamic acid) peptides. *Chem Commun (Camb)* **2015**, *51* (88), 15902-5.

## **B.2 Chapter 2 (Influence of Molecular Structure on a Self-Assembled Monolayer's Piezoresponse)**

1. Bowen, C. R.; Kim, H. A.; Weaver, P. M.; Dunn, S., Piezoelectric and Ferroelectric Materials and Structures for Energy Harvesting Applications. *Energy Environ. Sci.* **2014**, *7*, 25-44.
2. Dahiya, R. S.; Metta, G.; Valle, M.; Adami, A.; Lorenzelli, L., Piezoelectric Oxide Semiconductor Field Effect Transistor Touch Sensing Devices. *Appl. Phys. Lett.* **2009**, *95*, 034105.
3. Ciubotariu, D. A.; Ivan, I. A.; Clévy, C.; Lutz, P., Piezoelectric 3D Actuator for Micro-Manipulation Based on [011]-Poled PMN-PT Single Crystal. *Sensors and Actuators A: Physical* **2016**, *252*, 242-252.
4. Ilyas, M. A.; Swingler, J., Towards a Prototype Module for Piezoelectric Energy Harvesting from Raindrop Impacts. *Energy* **2017**, *125*, 716-725.

5. Ishikawa, M.; Uchida, Y.; Tabaru, M.; Kurosawa, M.; Kosuge, N.; Sugiyama, H., High Frequency and High Intensity Ultrasonic Transducers for Medical Applications Using Oriented Piezoelectric Thick Films by Hydrothermal Method. *J. Acoust. Soc. Am.* **2016**, *140*, 3374-3374.
6. Lefki, K.; Dormans, G. J. M., Measurement of Piezoelectric Coefficients of Ferroelectric Thin Films. *J. Appl. Phys.* **1994**, *76*, 1764-1767.
7. Hutson, A. R., Piezoelectricity and Conductivity in ZnO and CdS. *Phys. Rev. Lett.* **1960**, *4*, 505-507.
8. Bottom, V. E., Measurement of the Piezoelectric Coefficient of Quartz Using the Fabry-Perot Dilatometer. *J. Appl. Phys.* **1970**, *41*, 3941-3944.
9. Heiji, K., The Piezoelectricity of Poly (Vinylidene Fluoride). *Jpn. J. Appl. Phys.* **1969**, *8*, 975.
10. Quan, X.; Marvin, C. W.; Seebald, L.; Hutchison, G. R., Single-Molecule Piezoelectric Deformation: Rational Design from First-Principles Calculations. *J. Phys. Chem. C* **2013**, *117*, 16783-16790.
11. Eiichi, F.; Iwao, Y., Piezoelectric Effects in Collagen. *Jpn. J. Appl. Phys.* **1964**, *3*, 117.
12. Anderson, J. C.; Eriksson, C., Electrical Properties of Wet Collagen. *Nature* **1968**, *218*, 166-168.
13. Lee, B. Y.; Zhang, J.; Zueger, C.; Chung, W.-J.; Yoo, S. Y.; Wang, E.; Meyer, J.; Ramesh, R.; Lee, S.-W., Virus-Based Piezoelectric Energy Generation. *Nat. Nanotechnol.* **2012**, *7*, 351-356.
14. Nguyen, V.; Jenkins, K.; Yang, R., Epitaxial Growth of Vertically Aligned Piezoelectric Diphenylalanine Peptide Microrods with Uniform Polarization. *Nano Energy* **2015**, *17*, 323-329.
15. Nguyen, V.; Zhu, R.; Jenkins, K.; Yang, R., Self-assembly of diphenylalanine peptide with controlled polarization for power generation. *Nat. Commun.* **2016**, *7*, 13566.
16. Kholkin, A.; Amdursky, N.; Bdikin, I.; Gazit, E.; Rosenman, G., Strong Piezoelectricity in Bioinspired Peptide Nanotubes. *ACS Nano* **2010**, *4*, 610-614.
17. Farrar, D.; Ren, K.; Cheng, D.; Kim, S.; Moon, W.; Wilson, W. L.; West, J. E.; Yu, S. M., Permanent Polarity and Piezoelectricity of Electrospun  $\alpha$ -Helical Poly( $\alpha$ -Amino Acid) Fibers. *Adv. Mater.* **2011**, *23*, 3954-3958.
18. Werling, K. A.; Hutchison, G. R.; Lambrecht, D. S., Piezoelectric Effects of Applied Electric Fields on Hydrogen-Bond Interactions: First-Principles Electronic Structure Investigation of Weak Electrostatic Interactions. *J. Phys. Chem. Lett.* **2013**, *4*, 1365-1370.
19. Werling, K. A.; Griffin, M.; Hutchison, G. R.; Lambrecht, D. S., Piezoelectric Hydrogen Bonding: Computational Screening for a Design Rationale. *J. Phys. Chem. A* **2014**, *118*, 7404-7410.

20. Quan, X.; Madura, J. D.; Hutchison, G. R., Self-Assembled Monolayer Piezoelectrics: Electric-Field Driven Conformational Changes. *submitted*.
21. Banerjee, R.; Chattopadhyay, S.; Basu, G., Conformational Preferences of a Short Aib/Ala-Based Water-Soluble Peptide as a Function of Temperature. *Proteins: Struct., Funct., Bioinf.* **2009**, *76*, 184-200.
22. Gellman, S. H., Foldamers: A Manifesto. *Acc. Chem. Res.* **1998**, *31*, 173-180.
23. Bautista, A. D.; Craig, C. J.; Harker, E. A.; Schepartz, A., Sophistication of Foldamer Form and Function in Vitro and in Vivo. *Curr. Opin. Chem. Biol.* **2007**, *11*, 685-692.
24. Goodman, C. M.; Choi, S.; Shandler, S.; DeGrado, W. F., Foldamers as Versatile Frameworks for the Design and Evolution of Function. *Nat. Chem. Biol.* **2007**, *3*, 252-262.
25. Guichard, G.; Huc, I., Synthetic Foldamers. *Chem. Commun.* **2011**, *47*, 5933-5941.
26. Kirshenbaum, K.; Barron, A. E.; Goldsmith, R. A.; Armand, P.; Bradley, E. K.; Truong, K. T. V.; Dill, K. A.; Cohen, F. E.; Zuckermann, R. N., Sequence-Specific Polypeptoids: A Diverse Family of Heteropolymers with Stable Secondary Structure. *Proc. Natl. Acad. Sci. USA* **1998**, *95*, 4303-4308.
27. Sun, J.; Zuckermann, R. N., Peptoid Polymers: A Highly Designable Bioinspired Material. *ACS Nano* **2013**, *7*, 4715-4732.
28. Wu, C. W.; Sanborn, T. J.; Huang, K.; Zuckermann, R. N.; Barron, A. E., Peptoid Oligomers with  $\alpha$ -Chiral, Aromatic Side Chains: Sequence Requirements for the Formation of Stable Peptoid Helices. *J. Am. Chem. Soc.* **2001**, *123*, 6778-6784.
29. Shin, H.-M.; Kang, C.-M.; Yoon, M.-H.; Seo, J., Peptoid Helicity Modulation: Precise Control of Peptoid Secondary Structures via Position-Specific Placement of Chiral Monomers. *Chem. Commun.* **2014**, *50*, 4465-4468.
30. Lu, H.; Hood, M. A.; Mauri, S.; Baio, J. E.; Bonn, M.; Munoz-Espi, R.; Weidner, T., Biomimetic Vaterite Formation at Surfaces Structurally Templated by Oligo(Glutamic Acid) Peptides. *Chem. Commun.* **2015**, *51*, 15902-15905.
31. Marino, A. A.; Becker, R. O.; Soderholm, S. C., Origin of the Piezoelectric Effect in Bone. *Calc. Tis. Res.* **1971**, *8*, 177-180.
32. Fukada, E., Piezoelectricity of Wood. *J. Phys. Soc. Jpn.* **1955**, *10*, 149-154.
33. Moody, M. J.; Marvin, C. W.; Hutchison, G. R., Molecularly-Doped Polyurethane Foams with Massive Piezoelectric Response. *J. Mater. Chem. C* **2016**, *4*, 4387-4392.

## B.3 Chapter 3 (Optimization of Nanoscale Electromechanical Coupling Evaluation

### Methods)

1. Abdollahi, A.; Domingo, N.; Arias, I.; Catalan, G., Converse flexoelectricity yields large piezoresponse force microscopy signals in non-piezoelectric materials. *Nat Commun* **2019**, *10* (1), 1266.
2. Balke, N.; Maksymovych, P.; Jesse, S.; Herklotz, A.; Tselev, A.; Eom, C. B.; Kravchenko, II; Yu, P.; Kalinin, S. V., Differentiating Ferroelectric and Nonferroelectric Electromechanical Effects with Scanning Probe Microscopy. *ACS Nano* **2015**, *9* (6), 6484-92.
3. Chae, I.; Jeong, C. K.; Ounaies, Z.; Kim, S. H., Review on Electromechanical Coupling Properties of Biomaterials. *ACS Applied Bio Materials* **2018**, *1* (4), 936-953.
4. Gruverman, A.; Kalinin, S. V., Piezoresponse force microscopy and recent advances in nanoscale studies of ferroelectrics. *Journal of Materials Science* **2006**, *41* (1), 107-116.
5. Guerin, S.; Syed, T. A. M.; Thompson, D., Deconstructing collagen piezoelectricity using alanine-hydroxyproline-glycine building blocks. *Nanoscale* **2018**, *10* (20), 9653-9663.
6. Kalinin, S. V.; Rodriguez, B. J.; Jesse, S.; Karapetian, E.; Mirman, B.; Eliseev, E. A.; Morozovska, A. N., Nanoscale electromechanics of ferroelectric and biological systems: A new dimension in scanning probe microscopy. *Annual Review of Materials Research* **2007**, *37* (1), 189-238.
7. Kang, S. K.; Koo, J.; Lee, Y. K.; Rogers, J. A., Advanced Materials and Devices for Bioresorbable Electronics. *Acc Chem Res* **2018**, *51* (5), 988-998.
8. Lee, J. H.; Heo, K.; Schulz-Schonhagen, K.; Lee, J. H.; Desai, M. S.; Jin, H. E.; Lee, S. W., Diphenylalanine Peptide Nanotube Energy Harvesters. *ACS Nano* **2018**, *12* (8), 8138-8144.
9. Li, N.; Yi, Z.; Ma, Y.; Xie, F.; Huang, Y.; Tian, Y.; Dong, X.; Liu, Y.; Shao, X.; Li, Y.; Jin, L.; Liu, J.; Xu, Z.; Yang, B.; Zhang, H., Direct Powering a Real Cardiac Pacemaker by Natural Energy of a Heartbeat. *ACS Nano* **2019**, *13* (3), 2822-2830.
10. Lucklum, R.; Behling, C.; Cernosek, R. W.; Martin, S. J., Determination of complex shear modulus with thickness shear mode resonators. *Journal of Physics D-Applied Physics* **1997**, *30* (3), 346-356.
11. Lv, Z. S.; Li, W. L.; Yang, L.; Loh, X. J.; Chen, X. D., Custom-Made Electrochemical Energy Storage Devices. *Acs Energy Letters* **2019**, *4* (2), 606-614.
12. Panda, S. S.; Katz, H. E.; Tovar, J. D., Solid-state electrical applications of protein and peptide based nanomaterials. *Chem Soc Rev* **2018**, *47* (10), 3640-3658.

13. Tabata, Y.; Takagaki, K.; Uji, H.; Kimura, S., Piezoelectric property of bundled peptide nanotubes stapled by bis-cyclic-beta-peptide. *J Pept Sci* **2019**, *25* (1), e3134.
14. Fang, X. Q.; Liu, J. X.; Gupta, V., Fundamental formulations and recent achievements in piezoelectric nano-structures: a review. *Nanoscale* **2013**, *5* (5), 1716-26.
15. Zhang, J.; Wang, C.; Bowen, C., Piezoelectric effects and electromechanical theories at the nanoscale. *Nanoscale* **2014**, *6* (22), 13314-27.
16. Marvin, C. W.; Grimm, H. M.; Miller, N. C.; Horne, W. S.; Hutchison, G. R., Interplay among Sequence, Folding Propensity, and Bio-Piezoelectric Response in Short Peptides and Peptoids. *J Phys Chem B* **2017**, *121* (44), 10269-10275.
17. Rabe, U., *Atomic Force Acoustic Microscopy*. Springer: 2006; p 54.
18. Balke, N.; Maksymovych, P.; Jesse, S.; Kravchenko, II; Li, Q.; Kalinin, S. V., Exploring local electrostatic effects with scanning probe microscopy: implications for piezoresponse force microscopy and triboelectricity. *ACS Nano* **2014**, *8* (10), 10229-36.
19. Christman, J. A.; Woolcott, R. R.; Kingon, A. I.; Nemanich, R. J., Piezoelectric measurements with atomic force microscopy. *Applied Physics Letters* **1998**, *73* (26), 3851-3853.
20. Kalinin, S. V.; Bonnell, D. A., Imaging mechanism of piezoresponse force microscopy of ferroelectric surfaces. *Physical Review B* **2002**, *65* (12).
21. Kalinin, S. V.; Karapetian, E.; Kachanov, M., Nanoelectromechanics of piezoresponse force microscopy. *Physical Review B* **2004**, *70* (18).
22. Jesse, S.; Baddorf, A. P.; Kalinin, S. V., Dynamic behaviour in piezoresponse force microscopy. *Nanotechnology* **2006**, *17* (6), 1615-28.
23. Jesse, S.; Mirman, B.; Kalinin, S. V., Resonance enhancement in piezoresponse force microscopy: Mapping electromechanical activity, contact stiffness, and Q factor. *Applied Physics Letters* **2006**, *89* (2).
24. Rodriguez, B. J.; Callahan, C.; Kalinin, S. V.; Proksch, R., Dual-frequency resonance-tracking atomic force microscopy. *Nanotechnology* **2007**, *18* (47).
25. Jesse, S.; Kalinin, S. V., Band excitation in scanning probe microscopy: sines of change. *Journal of Physics D-Applied Physics* **2011**, *44* (46).
26. Gomez, A.; Puig, T.; Obradors, X., Diminish electrostatic in piezoresponse force microscopy through longer or ultra-stiff tips. *Applied Surface Science* **2018**, *439*, 577-582.
27. Kim, S.; Seol, D.; Lu, X.; Alexe, M.; Kim, Y., Electrostatic-free piezoresponse force microscopy. *Sci Rep* **2017**, *7*, 41657.
28. Calahorra, Y.; Smith, M.; Datta, A.; Benisty, H.; Kar-Narayan, S., Mapping piezoelectric response in nanomaterials using a dedicated non-destructive scanning probe technique. *Nanoscale* **2017**, *9* (48), 19290-19297.

29. Vasudevan, R. K.; Balke, N.; Maksymovych, P.; Jesse, S.; Kalinin, S. V., Ferroelectric or non-ferroelectric: Why so many materials exhibit “ferroelectricity” on the nanoscale. *Applied Physics Reviews* **2017**, *4* (2).
30. Gannepalli, A.; Yablon, D. G.; Tsou, A. H.; Proksch, R., Corrigendum: Mapping nanoscale elasticity and dissipation using dual frequency contact resonance AFM. *Nanotechnology* **2013**, *24* (15).
31. Idiris, A.; Alam, M. T.; Ikai, A., Spring mechanics of alpha-helical polypeptide. *Protein Eng* **2000**, *13* (11), 763-70.
32. Stan, G.; King, S. W.; Cook, R. F., Nanoscale mapping of contact stiffness and damping by contact resonance atomic force microscopy. *Nanotechnology* **2012**, *23* (21), 215703.
33. Katsouras, I.; Asadi, K.; Li, M.; van Driel, T. B.; Kjaer, K. S.; Zhao, D.; Lenz, T.; Gu, Y.; Blom, P. W.; Damjanovic, D.; Nielsen, M. M.; de Leeuw, D. M., The negative piezoelectric effect of the ferroelectric polymer poly(vinylidene fluoride). *Nat Mater* **2016**, *15* (1), 78-84.
34. Liu, S.; Cohen, R. E., Origin of Negative Longitudinal Piezoelectric Effect. *Phys Rev Lett* **2017**, *119* (20), 207601.
35. Zhu, G.; Zeng, Z.; Zhang, L.; Yan, X., Piezoelectricity in  $\beta$ -phase PVDF crystals: A molecular simulation study. *Computational Materials Science* **2008**, *44* (2), 224-229.
36. Bottom, V. E., Dielectric-Constants of Quartz. *Journal of Applied Physics* **1972**, *43* (4), 1493.
37. Damos, F. S.; Luz, R. C.; Kubota, L. T., Determination of thickness, dielectric constant of thiol films, and kinetics of adsorption using surface plasmon resonance. *Langmuir* **2005**, *21* (2), 602-9.

#### **B.4 Chapter 4 (Exploration of Organic-Molecular Based Ferroelectric Materials)**

1. Fridkin, V.; Ducharme, S., *Ferroelectricity at the Nanoscale*. 2014.
2. Fujii, S.; Ziatdinov, M.; Higashibayashi, S.; Sakurai, H.; Kiguchi, M., Bowl Inversion and Electronic Switching of Buckybowls on Gold. *J Am Chem Soc* **2016**, *138* (37), 12142-9.
3. Guerin, S.; O'Donnell, J.; Haq, E. U.; McKeown, C.; Silien, C.; Rhen, F. M. F.; Soulimane, T.; Tofail, S. A. M.; Thompson, D., Racemic Amino Acid Piezoelectric Transducer. *Phys Rev Lett* **2019**, *122* (4), 047701.
4. Chae, I.; Jeong, C. K.; Ounaies, Z.; Kim, S. H., Review on Electromechanical Coupling Properties of Biomaterials. *ACS Applied Bio Materials* **2018**, *1* (4), 936-953.

5. Cheong, L. Z.; Zhao, W.; Song, S.; Shen, C., Lab on a tip: Applications of functional atomic force microscopy for the study of electrical properties in biology. *Acta Biomater* **2019**, *99*, 33-52.
6. Guerin, S.; Tofail, S. A. M.; Thompson, D., Organic piezoelectric materials: milestones and potential. *Npg Asia Materials* **2019**, *11* (1).
7. Fellows, W. B.; Rice, A. M.; Williams, D. E.; Dolgoplova, E. A.; Vannucci, A. K.; Pellechia, P. J.; Smith, M. D.; Krause, J. A.; Shustova, N. B., Redox-Active Corannulene Buckybowls in a Crystalline Hybrid Scaffold. *Angew Chem Int Ed Engl* **2016**, *55* (6), 2195-9.
8. Kim, D.; Han, S. A.; Kim, J. H.; Lee, J. H.; Kim, S. W.; Lee, S. W., Biomolecular Piezoelectric Materials: From Amino Acids to Living Tissues. *Adv Mater* **2020**, e1906989.
9. Frey, B. L.; Corn, R. M., Covalent attachment and derivatization of poly(L-lysine) monolayers on gold surfaces as characterized by polarization-modulation FT-IR spectroscopy. *Anal Chem* **1996**, *68* (18), 3187-3193.
10. Jesse, S.; Lee, H. N.; Kalinin, S. V., Quantitative mapping of switching behavior in piezoresponse force microscopy. *Review of Scientific Instruments* **2006**, *77* (7).
11. Quan, X.; Hutchison, G. R. Single Molecule Ferroelectrics via Conformational Inversion: An Electronic Structure Investigation 2017, p. 25.
12. Gorbunov, A. V.; Iglesias, M. G.; Guilleme, J.; Cornelissen, T. D.; Roelofs, W. S. C.; Torres, T.; Gonzalez-Rodriguez, D.; Meijer, E. W.; Kemerink, M., Ferroelectric self-assembled molecular materials showing both rectifying and switchable conductivity. *Science Advances* **2017**, *3* (9).
13. Miyajima, D.; Tashiro, K.; Araoka, F.; Takezoe, H.; Kim, J.; Kato, K.; Takata, M.; Aida, T., Liquid crystalline corannulene responsive to electric field. *J Am Chem Soc* **2009**, *131* (1), 44-5.
14. Saito, M.; Shinokubo, H.; Sakurai, H., Figuration of bowl-shaped  $\pi$ -conjugated molecules: properties and functions. *Materials Chemistry Frontiers* **2018**, *2* (4), 635-661.
15. Vasudevan, R. K.; Balke, N.; Maksymovych, P.; Jesse, S.; Kalinin, S. V., Ferroelectric or non-ferroelectric: Why so many materials exhibit “ferroelectricity” on the nanoscale. *Applied Physics Reviews* **2017**, *4* (2).
16. Rodriguez, B. J.; Callahan, C.; Kalinin, S. V.; Proksch, R., Dual-frequency resonance-tracking atomic force microscopy. *Nanotechnology* **2007**, *18* (47).
17. Miller, N. C.; Grimm, H. M.; Horne, W. S.; Hutchison, G. R., Accurate electromechanical characterization of soft molecular monolayers using piezo force microscopy. *Nanoscale Advances* **2019**, *1* (12), 4834-4843.

18. Shrestha, B. B.; Karanjit, S.; Higashibayashi, S.; Sakurai, H., Correlation between bowl-inversion energy and bowl depth in substituted sumanenes. *Pure and Applied Chemistry* **2014**, *86* (5), 747-753.
19. Huang, C. R.; Luo, X.; Liao, W. Q.; Tang, Y. Y.; Xiong, R. G., An Above-Room-Temperature Molecular Ferroelectric: [Cyclopentylammonium]<sub>2</sub>CdBr<sub>4</sub>. *Inorg Chem* **2020**, *59* (1), 829-836.
20. Lim, M. S.; Feng, K.; Chen, X.; Wu, N.; Raman, A.; Nightingale, J.; Gawalt, E. S.; Korakakis, D.; Hornak, L. A.; Timperman, A. T., Adsorption and desorption of stearic acid self-assembled monolayers on aluminum oxide. *Langmuir* **2007**, *23* (5), 2444-52.
21. Nguyen, K. C., Quantitative analysis of COOH-terminated alkanethiol SAMs on gold nanoparticle surfaces. *Advances in Natural Sciences: Nanoscience and Nanotechnology* **2012**, *3* (4).
22. Seiders, T. J.; Baldrige, K. K.; Grube, G. H.; Siegel, J. S., Structure/energy correlation of bowl depth and inversion barrier in corannulene derivatives: combined experimental and quantum mechanical analysis. *J Am Chem Soc* **2001**, *123* (4), 517-25.
23. Stockl, Q. S.; Wu, T. C.; Mairena, A.; Wu, Y. T.; Ernst, K. H., Erecting buckybowls onto their edge: 2D self-assembly of terphenylcorannulene on the Cu(111) surface. *Faraday Discuss* **2017**, *204*, 429-437.
24. Ursic, H.; Prah, U., Investigations of ferroelectric polycrystalline bulks and thick films using piezoresponse force microscopy. *Proc Math Phys Eng Sci* **2019**, *475* (2223), 20180782.
25. Allara, D. L.; Nuzzo, R. G., Spontaneously Organized Molecular Assemblies. 2. Quantitative Infrared Spectroscopic Determination of Equilibrium Structures of Solution-Adsorbed n -Alkanoic Acids on an Oxidized Aluminum Surface. *Langmuir* **1985**, *1*, 14.
26. Gao, J.; Hu, Y.; Li, S.; Zhang, Y.; Chen, X., Adsorption of benzoic acid, phthalic acid on gold substrates studied by surface-enhanced Raman scattering spectroscopy and density functional theory calculations. *Spectrochim Acta A Mol Biomol Spectrosc* **2013**, *104*, 41-7.
27. Jee, S. H.; Kim, S. H.; Ko, J. H.; Kima, D.-J.; Yoon, Y. S., Ceramic Processing Research Wet chemical surface modification of ITO by a self assembled monolayer for an organic thin film transistor. *Journal of Ceramic Processing Research* **2008**, *9* (1), 42-45.
28. Quan, X.; Madura, J. D.; Hutchison, G. R. Self-Assembled Monolayer Piezoelectrics: Electric-Field Driven Conformational Changes 2017.
29. Yildirim, O., *Self-Assembled Monolayers on Metal Oxides: Applications in Nanotechnology*. 2010.

30. Tayi, A. S.; Kaeser, A.; Matsumoto, M.; Aida, T.; Stupp, S. I., Supramolecular ferroelectrics. *Nat Chem* **2015**, *7* (4), 281-94.
31. Li, P. F.; Tang, Y. Y.; Liao, W. Q.; Ye, H. Y.; Zhang, Y.; Fu, D. W.; You, Y. M.; Xiong, R. G., A semiconducting molecular ferroelectric with a bandgap much lower than that of BiFeO<sub>3</sub>. *Npg Asia Materials* **2017**, *9* (1), e342-e342.
32. Quan, X. F.; Marvin, C. W.; Seebald, L.; Hutchison, G. R., Single-Molecule Piezoelectric Deformation: Rational Design from First-Principles Calculations. *Journal of Physical Chemistry C* **2013**, *117* (33), 16783-16790.

## **B.5 Chapter 5 (Lab Scale Manipulation of Single and Multilayer Organic Self Assembled Structures)**

1. Anderson, M. E.; Srinivasan, C.; Hohman, J. N.; Carter, E. M.; Horn, M. W.; Weiss, P. S., Combining conventional lithography with molecular self-assembly for chemical patterning. *Advanced Materials* **2006**, *18* (24), 3258-+.
2. Carlson, A.; Bowen, A. M.; Huang, Y.; Nuzzo, R. G.; Rogers, J. A., Transfer printing techniques for materials assembly and micro/nanodevice fabrication. *Adv Mater* **2012**, *24* (39), 5284-318.
3. DeFranco, J. A.; Schmidt, B. S.; Lipson, M.; Malliaras, G. G., Photolithographic patterning of organic electronic materials. *Organic Electronics* **2006**, *7* (1), 22-28.
4. Friebel, S.; Aizenberg, J.; Abad, S.; Wiltzius, P., Ultraviolet lithography of self-assembled monolayers for submicron patterned deposition. *Applied Physics Letters* **2000**, *77* (15), 2406-2408.
5. Gates, B. D.; Xu, Q.; Stewart, M.; Ryan, D.; Willson, C. G.; Whitesides, G. M., New approaches to nanofabrication: molding, printing, and other techniques. *Chem Rev* **2005**, *105* (4), 1171-96.
6. Lin, M. H.; Chen, C. F.; Shiu, H. W.; Chen, C. H.; Gwo, S., Multilength-scale chemical patterning of self-assembled monolayers by spatially controlled plasma exposure: nanometer to centimeter range. *J Am Chem Soc* **2009**, *131* (31), 10984-91.
7. Mu, X.; Gao, A.; Wang, D.; Yang, P., Self-assembled monolayer-assisted negative lithography. *Langmuir* **2015**, *31* (9), 2922-30.
8. Shuster, M. J.; Vaish, A.; Cao, H. H.; Guttentag, A. I.; McManigle, J. E.; Gibb, A. L.; Martinez-Rivera, M.; Nezarati, R. M.; Hinds, J. M.; Liao, W. S.; Weiss, P. S.; Andrews, A. M.,

Patterning small-molecule biocapture surfaces: microcontact insertion printing vs. photolithography. *Chem Commun (Camb)* **2011**, 47 (38), 10641-3.

9. Zhou, C.; Nagy, G.; Walker, A. V., Toward molecular electronic circuitry: selective deposition of metals on patterned self-assembled monolayer surfaces. *J Am Chem Soc* **2005**, 127 (35), 12160-1.

10. Casalini, S.; Bortolotti, C. A.; Leonardi, F.; Biscarini, F., Self-assembled monolayers in organic electronics. *Chem Soc Rev* **2017**, 46 (1), 40-71.

11. Oh, S.; Park, S. K.; Kim, J. H.; Cho, I.; Kim, H. J.; Park, S. Y., Patterned Taping: A High-Efficiency Soft Lithographic Method for Universal Thin Film Patterning. *ACS Nano* **2016**, 10 (3), 3478-85.

12. Ong, Q.; Nianias, N.; Stellacci, F., A review of molecular phase separation in binary self-assembled monolayers of thiols on gold surfaces. *Epl-Europhys Lett* **2017**, 119 (6).

13. Liao, W. S.; Cheunkar, S.; Cao, H. H.; Bednar, H. R.; Weiss, P. S.; Andrews, A. M., Subtractive patterning via chemical lift-off lithography. *Science* **2012**, 337 (6101), 1517-21.

14. Pease, R. F.; Chou, S. Y., Lithography and Other Patterning Techniques for Future Electronics. *Proceedings of the IEEE* **2008**, 96 (2), 248-270.

15. Zhang, Y.; D'Ambra, C. A.; Katsumata, R.; Burns, R. L.; Somervell, M. H.; Segalman, R. A.; Hawker, C. J.; Bates, C. M., Rapid and Selective Deposition of Patterned Thin Films on Heterogeneous Substrates via Spin Coating. *ACS Appl Mater Interfaces* **2019**, 11 (23), 21177-21183.

16. Zhao, C.; Xu, X.; Yang, Q.; Man, T.; Jonas, S. J.; Schwartz, J. J.; Andrews, A. M.; Weiss, P. S., Self-Collapse Lithography. *Nano Lett* **2017**, 17 (8), 5035-5042.

17. Pimpin, A.; Srituravanich, W., Review on Micro- and Nanolithography Techniques and their Applications. *Engineering Journal* **2012**, 16 (1), 37-56.

18. Huang, J.; Hemminger, J. C., Photooxidation of thiols in self-assembled monolayers on gold. *Journal of the American Chemical Society* **1993**, 115 (8), 3342-3343.

19. Huang, J. Y.; Dahlgren, D. A.; Hemminger, J. C., Photopatterning of Self-Assembled Alkanethiolate Monolayers on Gold - a Simple Monolayer Photoresist Utilizing Aqueous Chemistry. *Langmuir* **1994**, 10 (3), 626-628.

20. Whitesides, G. M.; Xia, Y., Soft Lithography. *Angewandte Chemistry international edition* **1998**, 37 (5), 550 - 575.

21. Li, Y.; Huang, J.; McIver, R. T.; Hemminger, J. C., Characterization of thiol self-assembled films by laser desorption Fourier transform mass spectrometry. *Journal of the American Chemical Society* **1992**, 114 (7), 2428-2432.

22. Brewer, N. J.; Janusz, S.; Critchley, K.; Evans, S. D.; Leggett, G. J., Photooxidation of self-assembled monolayers by exposure to light of wavelength 254 nm: a static SIMS study. *J Phys Chem B* **2005**, *109* (22), 11247-56.
23. Brewer, N. J.; Rawsterne, R. E.; Kothari, S.; Leggett, G. J., Oxidation of self-assembled monolayers by UV light with a wavelength of 254 nm. *Journal of the American Chemical Society* **2001**, *123* (17), 4089-4090.
24. Al Mamun, A. H.; Zahid, A. A. S. M.; Lee, I.; Kang, H. S.; Hahn, J. R., Phase Segregation in the Mixed Alkyl Thiol Self-assembled Monolayers on a Gold Surface at a High Incubation Temperature in a Sealed Container. *Bulletin of the Korean Chemical Society* **2015**, *36* (11), 2710-2715.
25. Schmaltz, T.; Sforazzini, G.; Reichert, T.; Frauenrath, H., Self-Assembled Monolayers as Patterning Tool for Organic Electronic Devices. *Adv Mater* **2017**, *29* (18).
26. Tarlov, M. J.; Burgess, D. R. F.; Gillen, G., UV photopatterning of alkanethiolate monolayers self-assembled on gold and silver. *Journal of the American Chemical Society* **1993**, *115* (12), 5305-5306.
27. Sotthewes, K.; Kap, O.; Wu, H.; Thompson, D.; Huskens, J.; Zandvliet, H. J. W., Ordering of Air-Oxidized Decanethiols on Au(111). *J Phys Chem C Nanomater Interfaces* **2018**, *122* (15), 8430-8436.
28. Zhou, C.; Walker, A. V., Dependence of patterned binary alkanethiolate self-assembled monolayers on "UV-photopatterning" conditions and evolution with time, terminal group, and methylene chain length. *Langmuir* **2006**, *22* (26), 11420-5.
29. Zhou, C.; Walker, A. V., Formation of multilayer ultrathin assemblies using chemical lithography. *Langmuir* **2010**, *26* (11), 8441-9.
30. Bourg, M. C.; Badia, A.; Lennox, R. B., Gold-sulfur bonding in 2D and 3D self-assembled monolayers: XPS characterization. *J Phys Chem B* **2000**, *104* (28), 6562-6567.
31. Todeschini, M.; Bastos da Silva Fanta, A.; Jensen, F.; Wagner, J. B.; Han, A., Influence of Ti and Cr Adhesion Layers on Ultrathin Au Films. *ACS Appl Mater Interfaces* **2017**, *9* (42), 37374-37385.
32. Liu, G. Y.; Xu, S.; Qian, Y., Nanofabrication of self-assembled monolayers using scanning probe lithography. *Acc Chem Res* **2000**, *33* (7), 457-66.
33. Melitz, W.; Shen, J.; Kummel, A. C.; Lee, S., Kelvin probe force microscopy and its application. *Surface Science Reports* **2011**, *66* (1), 1-27.
34. Saito, N.; Hayashi, K.; Sugimura, H.; Takai, O.; Nakagiri, N., Surface potentials of patterned organosilane self-assembled monolayers acquired by Kelvin probe force microscopy and ab initio molecular calculation. *Chemical Physics Letters* **2001**, *349* (3-4), 172-177.

35. Lee, S. H.; Lin, W. C.; Kuo, C. H.; Karakachian, M.; Lin, Y. C.; Yu, B. Y.; Shyue, J. J., Photooxidation of Amine-Terminated Self-Assembled Monolayers on Gold. *J Phys Chem C* **2010**, *114* (23), 10512-10519.
36. Lee, M.-T.; Hsueh, C.-C.; Freund, M. S.; Ferguson, G. S., Air Oxidation of Self-Assembled Monolayers on Polycrystalline Gold: The Role of the Gold Substrate. *Langmuir* **1998**, *14* (22), 6419-6423.
37. Choi, I.; Kim, Y.; Kang, S. K.; Lee, J.; Yi, J., Phase separation of a mixed self-assembled monolayer prepared via a stepwise method. *Langmuir* **2006**, *22* (11), 4885-9.

### B.6 Chapter 6 (Conclusions and Future Directions)

1. Miller, N. C.; Grimm, H. M.; Horne, W. S.; Hutchison, G. R., Accurate electromechanical characterization of soft molecular monolayers using piezo force microscopy. *Nanoscale Advances* **2019**, *1* (12), 4834-4843.
2. Marvin, C. W.; Grimm, H. M.; Miller, N. C.; Horne, W. S.; Hutchison, G. R., Interplay among Sequence, Folding Propensity, and Bio-Piezoelectric Response in Short Peptides and Peptoids. *J Phys Chem B* **2017**, *121* (44), 10269-10275.
3. Guerin, S.; Tofail, S. A. M.; Thompson, D., Organic piezoelectric materials: milestones and potential. *Npg Asia Materials* **2019**, *11* (1).
4. Kim, D.; Han, S. A.; Kim, J. H.; Lee, J. H.; Kim, S. W.; Lee, S. W., Biomolecular Piezoelectric Materials: From Amino Acids to Living Tissues. *Adv Mater* **2020**, e1906989.
5. Lu, L.; Lahasky, S. H.; McCandless, G. T.; Zhang, D. H.; Garno, J. C., Thermoresponsive Behavior of Polypeptoid Nanostructures Investigated with Heated Atomic Force Microscopy: Implications toward the Development of Smart Coatings for Surface-Based Sensors. *Acs Applied Nano Materials* **2019**, *2* (12), 7617-7625.
6. Wu, C. W.; Kirshenbaum, K.; Sanborn, T. J.; Patch, J. A.; Huang, K.; Dill, K. A.; Zuckermann, R. N.; Barron, A. E., Structural and spectroscopic studies of peptoid oligomers with alpha-chiral aliphatic side chains. *J Am Chem Soc* **2003**, *125* (44), 13525-30.
7. Wu, C. W.; Sanborn, T. J.; Huang, K.; Zuckermann, R. N.; Barron, A. E., Peptoid oligomers with alpha-chiral, aromatic side chains: sequence requirements for the formation of stable peptoid helices. *J Am Chem Soc* **2001**, *123* (28), 6778-84.
8. Allara, D. L.; Nuzzo, R. G., Spontaneously Organized Molecular Assemblies. 2. Quantitative Infrared Spectroscopic Determination of Equilibrium Structures of Solution-Adsorbed n -Alkanoic Acids on an Oxidized Aluminum Surface. *Langmuir* **1985**, *1*, 14.

9. Gayatri, N. N. D.; Hutchison, G. R. Origins of Negative and Positive Electromechanical Response of Oligopeptide Piezoelectrics 2019.
10. Werling, K. A.; Griffin, M.; Hutchison, G. R.; Lambrecht, D. S., Piezoelectric hydrogen bonding: computational screening for a design rationale. *J Phys Chem A* **2014**, *118* (35), 7404-10.
11. Miyajima, D.; Tashiro, K.; Araoka, F.; Takezoe, H.; Kim, J.; Kato, K.; Takata, M.; Aida, T., Liquid crystalline corannulene responsive to electric field. *J Am Chem Soc* **2009**, *131* (1), 44-5.
12. Quan, X.; Hutchison, G. R. Single Molecule Ferroelectrics via Conformational Inversion: An Electronic Structure Investigation 2017, p. 25.
13. Shoji, Y.; Kajitani, T.; Ishiwari, F.; Ding, Q.; Sato, H.; Anetai, H.; Akutagawa, T.; Sakurai, H.; Fukushima, T., Hexathioalkyl sumanenes: an electron-donating buckybowl as a building block for supramolecular materials. *Chem Sci* **2017**, *8* (12), 8405-8410.
14. Shrestha, B. B.; Karanjit, S.; Higashibayashi, S.; Sakurai, H., Correlation between bowl-inversion energy and bowl depth in substituted sumanenes. *Pure and Applied Chemistry* **2014**, *86* (5), 747-753.
15. Seiders, T. J.; Baldrige, K. K.; Grube, G. H.; Siegel, J. S., Structure/energy correlation of bowl depth and inversion barrier in corannulene derivatives: combined experimental and quantum mechanical analysis. *J Am Chem Soc* **2001**, *123* (4), 517-25.
16. Gramse, G.; Casuso, I.; Toset, J.; Fumagalli, L.; Gomila, G., Quantitative dielectric constant measurement of thin films by DC electrostatic force microscopy. *Nanotechnology* **2009**, *20* (39), 395702.
17. Fumagalli, L.; Ferrari, G.; Sampietro, M.; Gomila, G., Quantitative Nanoscale Dielectric Microscopy of Single-Layer Supported Biomembranes. *Nano Lett* **2009**, *9* (4), 1604-1608.
18. Chae, I.; Jeong, C. K.; Ounaies, Z.; Kim, S. H., Review on Electromechanical Coupling Properties of Biomaterials. *ACS Applied Bio Materials* **2018**, *1* (4), 936-953.